Czech Technical University in Prague

Faculty of Electrical Engineering

Doctoral Thesis

August, 2016 *Martin Blažek*

Czech Technical University in Prague
Faculty of Electrical Engineering
Department of Radioelectronics

ALGORITHMS FOR IMAGE PROCESSING OF CROWDED FIELDS IN ASTRONOMY

Doctoral Thesis

Mgr. Martin Blažek

Prague, August 2016

Ph.D. Programme: Electrical Engineering and Information Technology
Branch of study: Radioelectronics

Supervisor: Doc. Mgr Petr Páta, PhD.
Supervisor-Specialist: Ing. Stanislav Vítek, Ph.D.

Abstract

This thesis deals with the image processing of so called crowded fields. These objects (such as Globular or Open stellar clusters) in astronomical images represent extremely dense and concentrated stellar fields and they are extremely difficult to analyse. This thesis brings detail analysis of this phenomena together with the description of the problem and suggestion of several new approaches and algorithms. The presented WHIDE algorithm (Weighed and Histogram Thresholded Deconvolution) deals with crowded fields by using both known (mathematical deconvolution, aperture and profile photometry, Nelder-Mead optimization, ...) and new approaches. The research about the application of standard image processing methods in astronomy and other fields is presented together with simulations and the analysis which helps in designation of the new algorithms. For these simulations new simulator of astronomical images (including instrumental errors and defects) with crowded fields called GlencoeSim is used. The suggested WHIDE algorithm uses as well two new approaches in data reduction - ”Flux Histogram Noise Thresholding” and Statistical weighing of deconvolution results. These methods allow the deconvolution process to be automatic and reliable and deal with both the noise and the deconvolution artefacts.

Acknowledgements

At this point I would like to thank to Dr. Stanislav Vítek who introduced me to the team of the Department of Radioelectronics in Czech Technical University. This thesis is actually a result of his suggestion, from one historical conference coffee break, for me to study at FEE CTU. Many thanks belong to my family for their spiritual support during my studies, and at this point I would like to symbolically dedicate this work to my grandfather Vlastimil Šenk for his everlasting faith in my scientific effort. The greatest thanks however belong to my supervisor Dr. Petr Páta for his towering patience and scientific mentoring. After years of my passive resistance these two attributes allowed this thesis to be born, which eventually made me extremely grateful.

This work was partially supported by Grant no. GA14-25251S of the Grant Agency of the Czech Republic and by the project SGS16/165/OHK3/2T/13 of the Student Grant Agency of the Czech Technical University no..

Abstrakt (CZE)

Tato dizertace se zabývá zpracováním obrazu zahuštěných hvězdných polí. Tyto objekty (jako jsou kulové či otevřené hvězdokupy) v astronomických datech reprezentují velmi koncentrované objekty, které je extrémně obtížné analyzovat a vědecky zpracovat. Tato dizertace obsahuje detailní analýzu tohoto problému spolu s jeho popisem a především s návrhem několika nových přístupů a algoritmů. Jádrem je navržený algoritmus WHIDE (Weighed and Histogram Thresholded Deconvolution), který zpracovává zahuštěná hvězdná pole jak pomocí známých psotředků (matematická dekonvoluce, aperturní a profilová fotometrie, Nelder-Mead optimalizace, ...), tak pomocí nových navržených postupů a myšlenek. Pro potřeby simulací je zde také navržen nový simulátor GlencoeSim pro vytváření sofistikovaných dat s komplikovanými hvězdnými poli (včetně šumových a přístrojových defektů). V práci je přednesena rešerše standardních metod pro zpracování obrazu v astronomii spolu s jejich analýzou a simulacemi, které v závěru pomohly k návrhu nového algoritmu WHIDE. Součástí tohoto algoritmu jsou také dva nové postupy - metoda nazvaná ”Flux Histogram Noise Thresholding” a tzv. myšlenka statistického váhování výsledků dekonvoluce, která obrací zavedené pořadí kroků u standardního zpracování astronomických dat pro potlačení šumu a dekonvolučních artefaktů.

Poděkování

Chtěl bych poděkovat doktoru Stanislavu Vítkovi za to, že mě seznámil s týmem na Katedře radioelektroniky a pomohl mi se do něj začlenit. Tato práce je totiž výsledkem jeho návrhu u kávy při jedné nejmenované konferenci, abych zkusil doktorát na FEL ČVUT. Své rodině bych chtěl poděkovat, že mě psychicky podporovali i přes můj nestudentský věk v mém studentském snažení a velký dík patří mému dědovi Vlastimilu Šenkovi, kterému bych rád tuto práci symbolicky věnoval, za jeho celoživotní duchovní dohled nad mým akademickým působením. Největší dík patří ovšem mému školiteli docentu Petru Pátovi, neboť jeho nebetyčná trpělivost a odborné vedení umožnily tomuto výzkumu vzniknout a jej po letech i přes můj častý pasivní odpor dovést do zdárného konce.

Tato práce vznikla za podpory Grantové Agentury ČR projektu GA14-25251S a studentské grantové soutěže ČVUT projektu SGS16/165/OHK3/2T/13.

Contents

Used symbols and abbreviations

ADU	Analog-Digital unit
CCD	Charged-Coupled Device
CTU	Czech Technical University in Prague
FITS	Flexible Image Transportation System
FOV	Field of view
FWHM	Full Width at Half-Maximum
GB	GigaByte of hard drive space
GC	Globular (stellar) Clusters
GRB	Gamma-Ray Burst
GSC	Guide Star Catalog
HST	Hubble Space Telescope
ICRS	International Celestial Reference System
INTEGRAL	International Gamma Ray Astrophysics Laboratory
IR	Infra-Red
IRAF	Image Reduction and Analysis Facility
NOAO	National Optical Astronomy Observatory
PCA	Principal Component Analysis
PDF	Probability Density Function
PSF	Point-Spread Function
px	Pixel
R-L	Richardson-Lucy deconvolution
SNR	Signal-to-Noise ratio
USNO	United States Naval Observatory
UWFC	Ultra Wide-Field Camera
WCS	World Coordinate System
WFC	Wide-Field Camera
WHIDE	Weighed and Histogram Thresholded Automatic Deconvolution
WILLIAM	Wide-field all-sky image analyzing monitoring system

$\hat{f}$	Fourier transform of a function f
$f * g$	convolution of functions f and g
X^T	transposition of the matrix X
σ	standard deviation
$p(X)$	probability of X
$p(X\|Y)$	conditional probability of X, Y
$\|x\|$	absolute value metrics
$O^{(n)}$	n-iteration to get estimation of O
$\bar{x}$	Mean or estimated mean value of x
$x!$	factorial number of x
$\sum_k x_k$	sum of k-values of x
$\prod_x x$	product of x values

1 Introduction

Billions and billions of stars shine around us even though we can't see most of them. The human eye can distinguish ca. 6000 stars in the sky [52], yet these billions are hidden somewhere above us. Grounded telescopes or space satellites in all possible wavelengths from radio to γ-rays observe the Universe and give us the data in the form of images, spectra or just single measurements. In these images though the billions and billions of stars often blend together and produce complex source of information about the Universe up there. Thesis topic is focused on the case of the astronomical images where the stars cannot be easily distinguished from each other. The field of study then overlaps with the area of image processing in informatics combined with experimental astronomy. Better image processing solutions for very complex data and at the end the algorithm for automatic deconvolution of crowded fields in astronomy is presented here.

The motivation for this work is based on the experiences of our team in Czech Technical University in Prague with developing and supporting of imaging systems MAIA [67], WILLIAM [29] or BOOTES [16]. Automatic data reduction of complicated stellar fields practically does not exist and one of the team tasks is to develop complex set of tools for the analysis of these complicated fields.

Thesis is divided in following order.

Chapter 2 explains the term *crowded field* in astronomy and the necessity for a new approach of the image processing algorithm. It shows the difficulties and the common situation in the scientific analysis.

Chapter 3 describes the brief state-of-the-art of the astronomical image processing related to our main thesis topic. It touches on the issues with the noise and Point Spread Function (PSF).

Chapter 4 offers the detailed "Astronomical data reduction" summary - the standard methods, their mathematical background, commonly used software, definition of the astrometry and the photometry terms and detailed description of the aperture and profile photometry methods. Sections 4.5.3 and 4.5.4 offer procedure outlines with several illustrations of the issues received in practice.

Chapter 5 describes the mathematical background for the image deconvolution and several practical methods used in the common image processing. Sections 5.1 - 5.2 offer detailed explanation of these deconvolution techniques given by the literature while section 5.3 shows the basic analysis of these techniques for their use in astronomy and their comparison.

Chapter 6 shows the brief selection of practical experiments where the newly designed algorithm would be useful and desired.

From chapter 7 up to chapter 14 author's simulations, analysis and new algorithms can be found. **Chapter 7 describes the published simulator of the astronomical images of crowded field called GlencoeSim.** Such a simulator is necessary to test the algorithms and the deconvolution as there is naturally no realistic data where the initial conditions would be perfectly known due to the presence of noise, which is omnipotent in the astronomical data reduction.

Chapter 8 uses the simulator GlencoeSim to produce dozens of Gigabytes of simulations under many various conditions and with different parameters. Sections 8.2 deals with how to efficiently analyse (the metrics) these huge amounts of simulated data in view of getting as much relevant information as possible. Section 8.4 explains how the Richardson-Lucy deconvolution [54, 57] was applied and the section 8.5 uses the Principal Component Analysis [44] to check whether the used parameters and metrics are suitable for the description of the simulations.

Chapter 9 then displays chosen results from the simulations made in the previous chapter 8. In the graphical figures the analysis tries to get the information about how the deconvolution behaves and which parameters influence the results and how much. These hints are important later when designing the new algorithm.

Chapter 10 tries to apply the optimization technique called Nelder-Mead [36] to find out if it is suitable for the case of getting the new designed algorithms as automatic as possible without the human intervention.

Chapter 11 just summarizes all the information we got from the chapters 7-10. They are immediately used in the following chapters concerning the newly designed algorithms themselves.

The new idea of the automatic thresholding is suggested in chapter 12. Such an idea is based on the knowledge of the objects in the astronomical images and namely the behaviour of the noise. Proposed name **"Flux histogram noise thresholding algorithm"** is connected with the inner principal of noise and stellar histogram operations to get the criteria, which would allow the following image processing automatic.

The core of the thesis is then when all the previous information is collected together to design the combination of steps which would allow the automatic and reliable deconvolution of the crowded fields based on the statistical approach. The whole proposed algorithm is called **WHIDE - Weighed and HIstogram thresholded DEconvolution** and its detailed description can be found in chapter 13. It is based on the combination of the methods and techniques (such as commonly known Richardson-Lucy deconvolution, profile photometry PSF acquisition,...) and two newly designed approaches. The first one is the "Flux histogram noise thresholding" from the chapter 12 (dealing with the automation and with the noise in deconvolution process) and **the second one suggests new "heretic" statistical approach based in weighing of the deconvolution results before combining the astronomical images**. The explanation and the motivation for this weighing step can be found in the section 13.1. Section 13.2 then describes the complete algorithm of WHIDE step by step.

The practical tests of the WHIDE algorithm can be found in chapter 14 where it is applied to the real semi-crowded field image together with standard astronomical image processing method (aperture photometry).

The contribution of this thesis can be regarded namely in four related objectives :

1. the GlencoeSim simulator,
2. Flux Histogram Noise Thresholding method (which is used as a step in the designed WHIDE algorithm),
3. the idea of statistically weighing of the deconvolution results before/without denoising image operations
4. and the whole WHIDE algorithm itself.

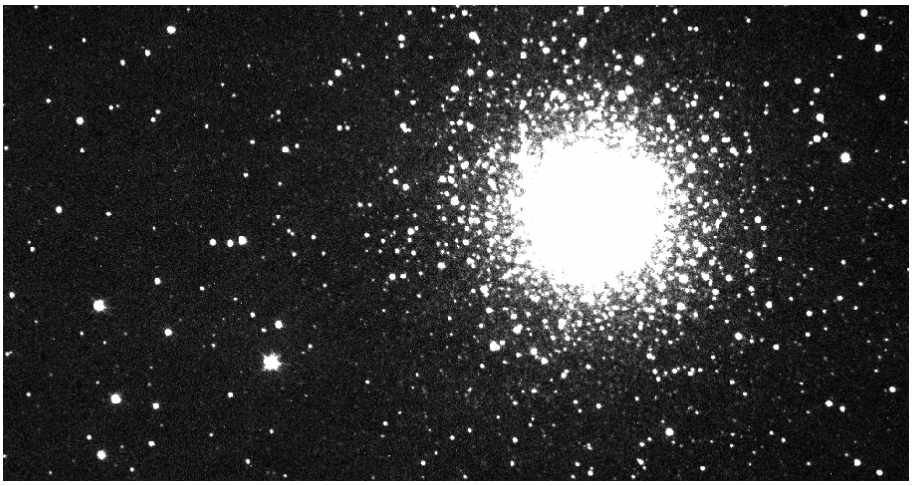

Figure 1: Globular Cluster M15 in Pegasus constellation - typical representative of *crowded field* in astronomical image processing.

2 Definition of the crowded field

In the near IR and optical part of spectrum digital linear sensors are widely used nowadays to obtain the signal from distant astronomical objects like stars, galaxies, nebulas, molecular clouds etc. Since the introduction of the digital sensors and fast computation capabilities the algorithms of the effective, robust or just fast flux and spectral measurements were presented to the scientific astronomical community. The problem is mostly separated to the *astrometry*, solving the positional questions and objects determination, and *photometry*, counting the fluxes of the astronomical objects [57]. CCD (Charged-Coupled Device) are commonly used nowadays for the astronomical observations in near IR or optical spectrum, in which most of the baryonic matter (e.g. stars) with its own source of energy shines [34].

The stars in the space tend to be gravitationally attracted to the larger systems. Most of them exists in the form of double (triple, quadruple, ...) stars consisting of the members orbiting around each other. Larger stellar systems are commonly called clusters, while two different groups can be defined [34] as :

- Open stellar (galactic) Clusters - those systems are mostly young (order of 10^6 - 10^8 years old), consisting of typically hundreds or thousands of members, observed in the galactic plane. Those stars have similar age due to the same birthplace from the embryonic Giant Molecular Cloud, while the gravitational force is not as strong to keep the members together for long time, hence the low age of commonly observed open clusters.

- Globular (stellar) Clusters (GCl) - those systems are very old, some of them born shortly after the Big Bang (13.7 10^9 years ago) ”remembering” the formation of the galaxies on consisting of the

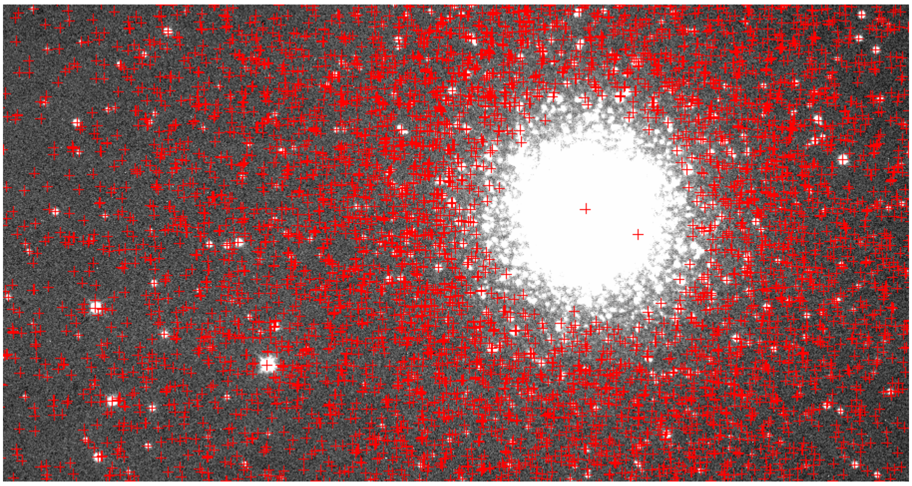

Figure 2: Globular Cluster M15 in Pegasus constellation - red crosses mark the positions of known, measured and catalogued stars in the USNO-B1.0 catalogue [47]

2^{nd} generation stars ($\sim 2^{\mathrm{nd}}$ population of stars with low metalicity). GCls contain mostly 10^3 - 10^6 members, which is the reason of the strong attractive gravitational force and long time-scale stability of those stellar systems. They are uniformly stretched in the galactic halo. Globular cluster M15 (Pegasus constellation) taken by the 50cm telescope in Ondrejov (CZ) observatory[1] with FLI-IMG CCD camera can be seen in figure 1.

For the purposes of the astronomical image processing the term *crowded field* is used [17] to express the optical digital data, in which the signal from the falling light of the (mostly stellar) sources is mutually significantly disturbed. This disturbance

- is stressed by the diffraction of the light in the atmosphere and the optical imaging system (e.g. telescope, space satellite, camera),
- is mainly caused by high number of the concentrated sources with similar order of the light flux
- and it does not necessarily have to be produced by the combination of more indistinguishable sources due to the wavelength of the falling light.

Typical representative of such crowded field is already mentioned GCl, whose members produce overlapping image signals on the digital sensor. Astrometry and precise photometry of this complicated image signal is commonly not processed automatically by the robotic telescopes and all-sky surveys.

---

[1] http://www.asu.cas.cz/

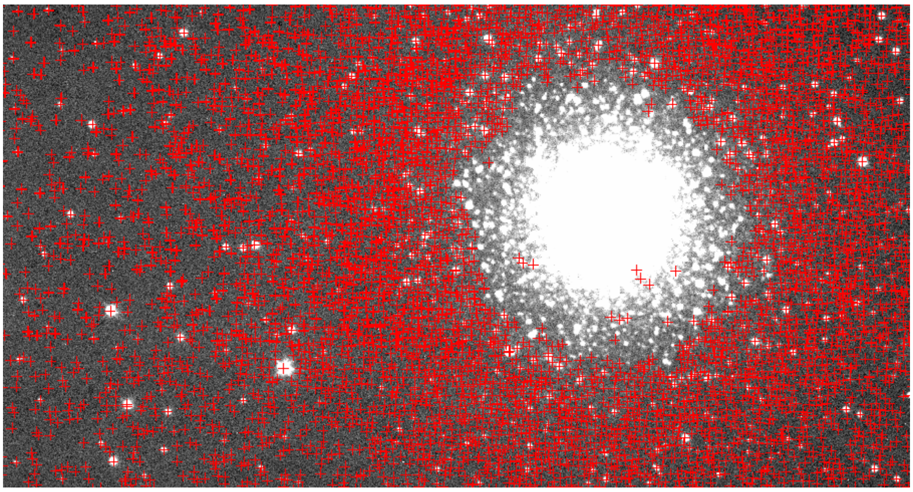

Figure 3: Globular Cluster M15 in Pegasus constellation - red crosses mark the positions of known, measured and catalogued stars in the GSC2.3 catalogue [38]

USNO-B is an all-sky catalogue [47] that presents positions, proper motions, magnitudes in various optical passbands, and star/galaxy estimators for more than 1042 million objects derived from 3643 million separate observations. The data were obtained from scans of 7435 Schmidt plates taken for the various sky surveys during 50 years. USNO-B1.0 is believed to provide all-sky coverage, completeness down to V = 21^{mag}, 0.2” astrometric accuracy at the astronomical epoch J2000, 0.3^{mag} photometric accuracy in up to five photometric colours, and 85% accuracy for distinguishing stars from non-stellar objects.

The Guide Star Catalog (GSC) is an all-sky database [38] of objects derived from the uncompressed Digitized Sky Surveys that the Space Telescope Science Institute has created from the Palomar and UK Schmidt survey plates and made available to the community. GSC-II was primarily created to provide guide star information and observation planning support for Hubble Space Telescope (HST). The GSC2.3 catalog contains astrometry, photometry, and classification for 945592683 objects down to the magnitude limit of the plates. Positions are tied to the International Celestial Reference System (ICRS) for stellar sources. Astrometric errors are 20% worse in the case of galaxies and approximately a factor of 2 worse for blended images. Outside of the galactic plane, stellar classification is reliable to at least 90% confidence for magnitudes brighter than RF = 19.5^{mag}, and the catalogue is complete to RF = 20^{mag}.

In figure 2 there is GCl (M15 in Pegasus), whose original image can be seen in figure 1, with the red cross marking the positions of all known, measured and catalogued stars in the USNO-B1.0 catalogue. The same thing done using the catalogue GSC is in figure 3. By comparing those two figures with the

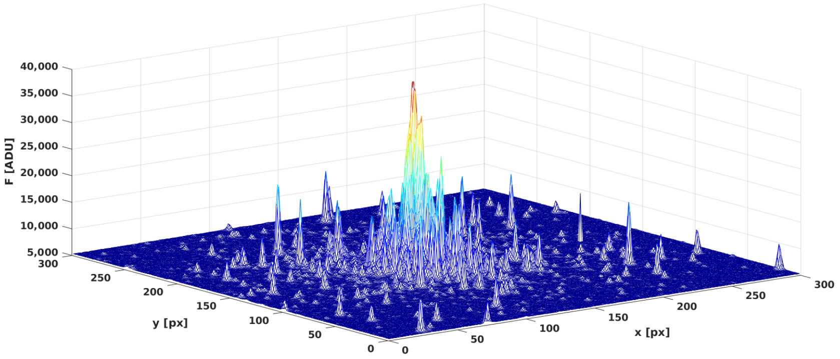

Figure 4: Globular Cluster M15 in Pegasus constellation from the figure 1 - the mesh of the image flux.

original one 1 one can easily see the void of catalogue entries in the area of the selected GCl. The need of effective method providing automatic astrometry and photometry of crowded fields is evident from those images.

To have the idea about how much the stars are blended in the mentioned GCl M15, one can see the meshed flux in figure 4.

3 State of the art

Data reduction algorithms of crowded fields is tied with the problem of profile photometry as described in the section 4.5 and therefore has to deal with the image's PSF and its time or spatial variabilities. Image processing detection of these data uses thresholding - some parameters representing the degree of confidence are taken into account in searching through the image for local density maxima which have the selected full-width half-maximum (FWHM) and a peak amplitude greater than the threshold above the local background [61]. More sophisticated detection algorithms can be based on the wavelet transform [21, 53, 5, 3]. When there are a few more stars or other nearby astronomical objects, manual PSF fitting photometry can be used, taking into account the Point-Spread Function (PSF), which can be either fixed or space-dependent around the image [59]. If no PSF is known, which happens in the case of images with crowded stellar fields (where PSF cannot be obtained from bright isolated stars) or in the case of images from observatories without adaptive optics and where the actual PSF is not known, various image processing deconvolution methods (including blind image deconvolution) have been published [15, 54, 37, 64] and are used in astronomy [57].

Historically, the IRAF astronomical package and specifically the DAOPHOT subpackage [59] attempted to deal with crowded fields, but the automatic solution was still an issue (self-iterative complex problem). The idea of preparing simulations is quite old, and as an example it was developed for the Hubble Space Telescope during its optics repair [40]. It attempted to deal with varying noise and then to use Richardson-Lucy deconvolution [54, 41]. Any astronomical space project from X-rays to radio prepares its own data simulator to estimate the imaging behaviour, while some imagers have recently focused even on crowded fields. For example the World Space Observatory - Ultraviolet (WSO-UV) instrument will eventually have a 1.7-meter telescope, and will probably have a small pixel scale, compact PSF and high sensitivity of the instrument [22]. This allows the use of known image abilities to develop a simulator of crowded fields for this specific instrument. Such a simulator[2], called CIS, was recently made available online, and takes into account a realistic conversion between physical flux and counts rate [55].

Common practice doesn't use any automatic methods of profile photometry for its complications and dependence on the input parameters (PSF, precise noise distribution) [18]. Because of other conditions often existing in astronomical observations lot of otherwise valuable data is not processed (the author's estimation is upto 15-20%) in the cases like

- presence of the GCls in the field of view,
- significant optical aberrations in the margins of the images [62],

---

[2] http://grupos.unican.es/glendama/CIS.html

- too low SNR to deal with using automatic thresholding methods [49],
- low spatial resolution in comparison with the observed objects ⇒ PSF is sampled on several pixels only. This problem is commonly present not only in wide-field astronomical cameras, but as well in high energy astrophysics field, where in the X-Ray and γ-Ray areas the light properties and instrumentation limits doesn't allow higher spatial resolution. The specific study about dealing with this problem in the case of INTEGRAL space satellite [70] at the expense of losing SNR can be found in [14].

The construction of the quality PSF spatial dependence on the image and modelling of the noise spatial distribution are intertwined. However for their complexness some basic approximations are still assumed in practice. Commonly during the data reduction of the time series of astronomical images (containing the same observational object) the imaging system is assumed to be time and spatial invariable (unless the data were measured using the Adaptive Optics system as mentioned in the section 4.5.2). This assumption is appropriate when only the slow changes of the imaging system itself is considered. However during the precise astronomical observations (like GRB optical afterglows or exoplanets' transits) or under worse observational conditions (omnipresent light pollution) the effects outside imaging system itself (namely atmosphere) apply stronger, influencing the resulting PSF. Moreover spatial invariant models of noise are used for its description during those measurements and the correction is widely done just with the simple subtraction of the darkframe [42].

Automatic and effective image data reduction is important namely for the autonomous telescope. The complex cybernetics management tools and control software are under development worldwide (e.g ASCOM or RTS2[3] [35]) and they are in need of data reduction algorithms dealing with complicated stellar in astronomical images.

In [26] algorithms searching for quality PSFs of specific non-point (non-stellar) objects are designed, while the tendency to "rediscover" the use of the wavelet transform (formerly rejected by hardcore astronomers) can be seen during the last years [53], [21]. The wavelet transform seems to be especially useful for the construction of stellar detection algorithms (*à trous*) [5].

In this thesis then the approach of the new automatic algorithm for deconvolution of crowded field is presented based on research of the deconvolution efficiency and two new ideas as discussed in chapters 12 and 13.

---

[3] http://rts2.org/

4 Astronomical data reduction

4.1 Astronomical image processing software

For the astronomical purposes FITS (Flexible Image Transportation System) format of the images is commonly used [69]. The file consists of text header with keywords according to the published standards and binary table of the raw data (image itself). The header keywords are important for the data reduction because it contains information about the conditions the measurements have been taken with (e.g. temperature, exposition, airmass, location, coordination system etc.).

- **IRAF** - IRAF[4] stands for the Image Reduction and Analysis Facility, a general purpose software system for the reduction and analysis of astronomical data. It is written and supported by the National Optical Astronomy Observatories (NOAO) in Arizona. The main IRAF distribution includes a selection of programs for general image processing and graphics, plus a large number of programs for the reduction and analysis of optical and IR astronomy data. Other external or layered packages are available for applications such as data acquisition or handling data from other observatories and wavelength regimes such as the Hubble Space Telescope (optical), EUVE (extreme ultra-violet), or ROSAT and AXAF or Chandra (X-ray). Big disadvantage of IRAF software is its complicated interface and user-unfriendliness. On the other side it provides uncountable number of tools for photometric or spectroscopic data processing. The most important part of IRAF for the purposes of crowded field image processing is DAOPHOT - software formed and theoretically introduced by Stetson in 1987 [59]. It is still widely used until today. The procedures of (non-automated) iterative profile photometry are described in the section 4.5.3 and deeper in the IRAF manual [17].

- **MUNIPACK**[5] - this is a free open source tool which tries to be a user-friendly tool for aperture photometry processing. It was designed in Brno (CZ) and is nowadays widely used for the fast and semi-automatic data processing of non-complicated astronomical signal.

- **SExtractor** - SExtractor[6] is a program that builds a catalogue of objects from an astronomical image. Although it is particularly oriented towards reduction of large scale galaxy-survey data, it can perform reasonably well on moderately crowded star fields.

- **OSA** - The INTEGRAL Off-line Scientific Analysis[7] is used to reduce and analyse data collected by the INTEGRAL X-Ray and γ-Ray satellite. It helps getting the spectral mosaics of high

---

[4] http://iraf.noao.edu/

[5] http://munipack.astronomy.cz/

[6] http://www.astromatic.net/software/sextractor

[7] http://www.isdc.unige.ch/integral/

energy astrophysical events by deconvolution of Science Windows (raw data) from the coded mask detector.

4.2 Astrometry

The position of the stars on the image can be determined by those several ways (or their combination):

- **Sensors on the telescope mount** - Incremental or absolute position sensors on the telescope mount can read the position of the coordinate wheels and save them to the FITS header. Such method is very inaccurate unless really expensive hardware and sensors are used. In professional astronomy this is rarely used unless the telescope field view has only a few stars to implement software recognition.

- **Wide-field cameras as pointers** - Nearly all professional telescopes have their own smaller fellow represented by Wide-field (WFC) or Ultra Wide-field (UWFC) cameras. They work as telescope pointers and astrometry processors. Because of lower magnitude limit they easily (in comparison with the main telescope) recognize the stars either by internal map or rather by software recognition [68].

- **Software recognition** - Information about the coordinates and the coordinate system (e.g. physical, celestial or galactic) can be saved in the FITS header [69] and for the equatorial case so called ”World Coordinate System” (WCS) is commonly used [24]. This parametric representation transforms directly the physical coordinates (width, height) of the specific image to the equatorial (right ascension, declination). The first published algorithm for matching image stars to catalogue stars automatically irrespective of the image scale presented Groth in 1986 [25]. The method uses the triangles, with many triangles contributing to each solution. Liebe [39] showed that the blind astrometry problem is easily solved when

    - there is a camera with a large field of view (tens of degrees),
    - the image scale is exactly known
    - and algorithm works with 1000 or so brightest stars on the sky.

  That method uses matching of the triangles of the stars. Other methods then mainly extend the algorithm from the triangles' to the polygons' similitude between the catalogue and the image data. In practice the astrometry is processed on the WF or UWF cameras assuming their precise parallelism with the main telescope.

4.3 Automatic detection of the objects

In 1987 Stetson presented DAOPHOT software package and algorithms [59] for the automatic object detection and crowded fields photometry. Those algorithms and their extensions are until today commonly used, while new approaches using wavelet transform are under development nowadays (e.g. [8]). Basically they use simple thresholding - few parameters representing the degree of the confidence are taken to search the images for local density maxima which have selected full-width half-maximum and a peak amplitude greater than threshold above the local background [49].

4.4 Aperture Photometry

Photometry in astronomy has to count the flux from the specific stellar (galactic, asteroid, ...) objects. Because of the historical tradition and logarithmic dependence of the human vision on the illumination, Pogson equation is used to differ the light fluxes F of two objects $1, 2$ in the magnitude quantity m [42]

$$m_1 - m_2 = -2.5 \log \frac{F_1}{F_2}. \tag{1}$$

Fluxes themselves can be in the most simple way counted as the sum of the flux on the pixels $F(\vec{x})$ inside the given *aperture*. Such an aperture can be easily positioned to the weighed flux center $\vec{x}_C$ (rather than local flux maximum)

$$\vec{x}_C = \frac{\sum_{x12} F(\vec{x})\vec{x}}{\sum_{x12} F(\vec{x})}, \tag{2}$$

where $\vec{x}$ is 2D position of the pixels on the image (if the PSF is known or approximated then its maximum can be used to precise the stellar center). The unknown radius of such an aperture is the largest disadvantage of the aperture photometry. If the radius is too small then the largest stars on the image would not be measured whole, while if the radius is too high then other smaller stars can be erroneously included to the measurement. The simple aperture photometry completely fail in the case of dense crowded stellar fields, where smaller stars are hidden in the wings of the brighter stars.

The photometric fluxes in astronomy are commonly counted using the specific spectral-band filters. There are lot of common photometric standards while probably the mostly used is due to the traditions Johnson UBVRI photometric system, whose filter transparencies can be seen in figure 5 [32]. The idea of calibration between RGB and Johnson filters is drafted in [66].

4.5 Profile Photometry

In the astronomical observations the original flux of the light and its spatial distribution $O(x, y)$ is deformed due to the conditions on its travel to the detector, while that degradation (e.g. caused by the

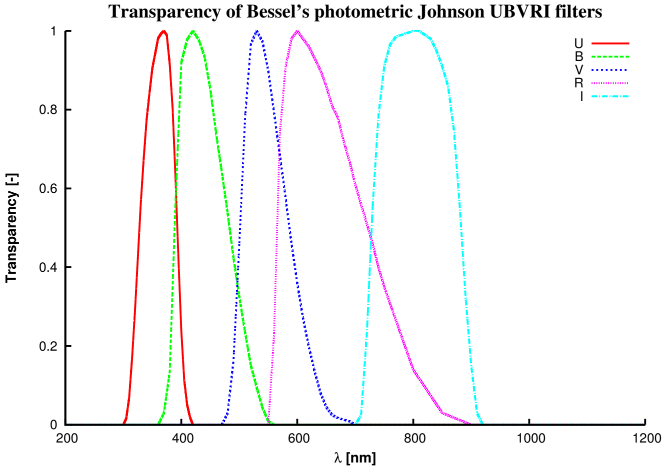

Figure 5: Transparency of Johnson standard photometric filters

atmosphere and the instrumental aberrations) can be in general described with some transfer function $P(x, y)$ - *Point-Spread Function* (PSF). Unless we could work in ideally isolated system with the temperature of 0 Kelvin, the additive noise $N(x, y)$ of many origins (e.g. thermal noise in the detector or fluctuations of the atmosphere) occurs. The "real" image $R(x, y)$ (for example captured on the CCD detector) is therefore [15]

$$R(x, y) = (P * O)(x, y) + N(x, y). \tag{3}$$

The construction of the PSF describing field of the point-shaped stars seems to be more simple than e.g. blind image deconvolution of general picture containing complicated shapes. On the other side the conditions during the exposition - namely high influence of the noise - make the simple 2D-deconvolution unusable. And furthermore the problem is

- *space-variant*, due to the aberrations of the optical system, and
- *time-variant*, because of the changing atmospheric conditions and observational positions on the sky with different zenit distance (and therefore different airmass).

There are several approaches in the literature to get the image stellar PSF :

- analytic - mathematical model (analytic function) is fitted on the real image data,
- iterative - the PSF is numerically iterated from the images alone to fulfill the optimization parameters.
- semi-empiric - optical abberations of the imaging system is measured, and

4.5.1 Analytic approach

Assuming only few-parametric analytic approximation of the PSF shape, several functions are widely used. The photons hitting the CCD detector provide the matrix of signal levels according to the Poisson distribution [42], but if we observe spatial distribution of that incidental process then with no other influential conditions one can expect elliptical Gaussian function to fit the stellar 2D profile

$$F_G(x,y) = F_G(0)\frac{1}{2\pi\sigma_x\sigma_y}\exp^{-\frac{(x-\mu_x)^2}{2\sigma_x^2}-\frac{(y-\mu_y)^2}{2\sigma_y^2}}. \tag{4}$$

However this function does not include other real circumstances e.g. optical system, atmospheric scatter etc. In practice the single stellar peaks have narrower and sharper shape therefore Lorentzian distribution can be used [49]

$$F_L(r) = F_L(0)\frac{2}{\pi}\frac{w}{4(r-\mu_r)^2+w^2}. \tag{5}$$

In 1969 Moffat derived the function by convolving Gaussian profile with diffraction profiles and the scattering function appropriate for photographic emulsions, which works on the images obtained by CCD as well [46].

$$F_M(r) = F_M(0)\left(1+\frac{r^2}{\alpha^2}\right)^{-\beta} \tag{6}$$

This analytic function is widely used as the first approximation to the real measured PSF of the stellar images. IRAF data reduction system [17] offers the combination of Gaussian core with Lorentzian wings producing the analytic function called ”Penny” [49] which may produce smaller standard deviation for the model fit.

4.5.2 Semi-empiric approach

If we assume that the optical system does not change or rather change its properties slowly, then laboratory measurements of the PSF before the astronomical use can be obtained. Such measurements can be done by the collimated illumination through the whole optical system and thus giving the information about the optical aberrations and dispersion on the optical elements (filters and lenses). But during the astronomical measurements on the ground-based telescopes the atmospheric variations play important role therefore ”artificial stars” in high altitudes provided by the lasers can be made and observed before or after any astronomical measurements to obtain the good PSF [51]. This procedure is used in combination with the *Adaptive Optics* system on the largest terrestrial observatories. Since PSF is known afterwards, profile photometry can be applied producing better results and measuring precision than aperture photometry.

4.5.3 Iterative numerical approach

This method can provide the best photometric results if no Adaptive Optics is used and if PSF is generally unknown. Which is acutally the most frequent case. It is well described in [17]. The largest disadvantage of this method is its non-regularity - iterative approach doesn't guarantee convergence in all cases. The PSF is constructed from some image data and is backward tested on the same image. Unfortunately this does not always provide good results and because of that this method is not automated yet. The usefulness of the results gotten by this method is in most cases determined by the experience with the choice of the parameters [17]. Advantage of this method (and in fact the reason, why it is so widely used) is that nothing else is needed except for the image data themselves.

In general this method use the shape of some ”typical” stars in the image getting them as the first iteration of the PSF. Higher iterations fit this PSF on those stars' surroundings trying to clear them from their stellar neighbours thus profiling the PSF shape. During every step the optimization test checks the suitability of the newer PSF. This is mostly done by simple subtraction of the adjusted stellar profile (constructed from the normalized PSF counted with the constant specific for each star gotten by the least-squares method fit) from the original (or already fitted and several times subtracted) image while looking on the created residua. The smaller the residua are, the better PSF is constructed. In practice that procedure is mostly insufficient and therefore several improvements can be used.

- Iterated PSF can be separated to the analytic part (analytic function with few free parameters e.g. Moffat or Gaussian) and residual part (so called *look-up tables*) dependent on the position of the star in the image. 1 look-up table is created for the PSF constant over the image, 3 look-up tables for the PSF dependent linearly on the position and 6 look-up tables for the PSF dependent quadratically.
- Sometimes fainter stars can be hidden in the wings of brighter stars. After iterated subtraction of the fitted bright stars on the image is proceeded, those faint stars occur and can be taken into account to reshape the PSF.

If (and that's not always) a good PSF is obtained and only negligible residua occur, then the advantage of this method for the astrometry and photometry of the stellar images is huge. Not only the precision of the measured magnitude is boosted, but as well fainter objects may be detected in the noise.

4.5.4 Procedure outline

In this subsection the procedure of iterative numerical approach is described on the example of the FITS image shown in figure 4.5.4.

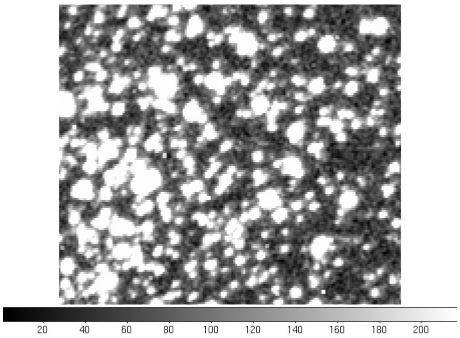

Figure 6: Original example image used for subtraction of PSFs

In general the iterative numerical method use the shape of some ”typical” stars (or all of them - the resulting differences can be seen in figures in the table 1) on the image getting them as the first iteration of the PSF. Higher iterations fit this PSF on those stars’ surroundings trying to clear them from their stellar neighbours thus profiling the PSF shape. During every step the optimization test checks the suitability of the newer PSF. This is mostly done by simple subtraction of the adjusted stellar profile (constructed from the normalized PSF counted with the constant specific for each star gotten by the least-squares method fit) from the original (or already fitted and several times subtracted) image while looking on the created residua. The smaller the residua are, the better PSF is constructed. In practice that procedure is mostly insufficient and therefore several improvements can be used.

- Iterated PSF can be separated to the analytic part (analytic function with few free parameters e.g. Moffat or Gaussian) and residual part (so called *look-up tables*) dependent on the position of the star in the image as can be seen in figures in the table 2.
- Sometimes fainter stars can be hidden in the wings of brighter stars. After iterated subtraction of the fitted bright stars on the image is proceeded, those faint stars occur and can be taken into account to reshape the PSF.

If (and that’s not always) a good PSF is obtained and only negligible residua occur, then the advantage of this method for the astrometry and photometry of the stellar images is huge. Not only the precision of the measured magnitude is boosted, but as well fainter objects may be detected in the noise. In figure 7 the example of the parameters’ space influence on the number of detected stars on the example image is shown.

In general the astrometric algorithms (based on polygon similarities between the catalogues and measured data) reveal the coordinates of the image successfully, while the research is mostly focused on the efficiency and limits of those algorithms. There is nearly no consensus until today on the object

1 brightest photometrical model star

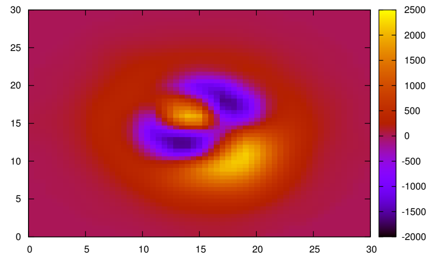

5 brightest photometrical model stars

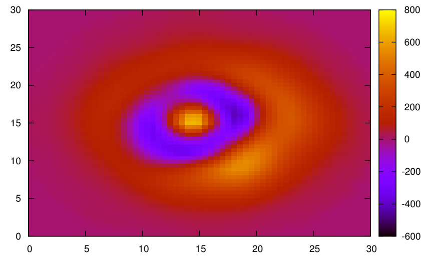

13 brightest photometrical model stars

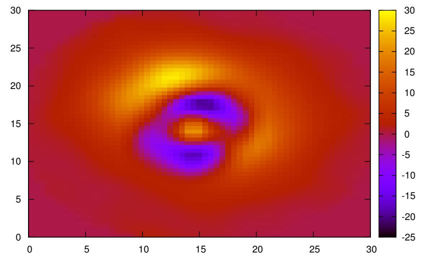

Table 1: Look-up tables (deviations from the analytic function) of PSFs constructed with different choice of model stars from the example image.

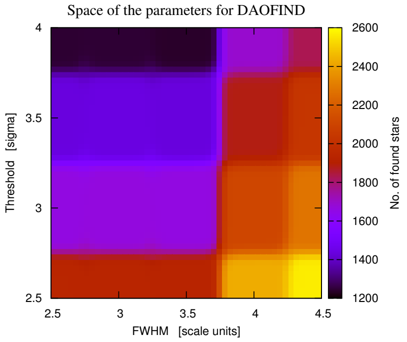

Figure 7: Number of stars found in dependence on threshold (in σ quantities) and supposed FWHM of the stellar PSF shape on the example image.

detection methods except the simple thresholding needing external parameters as the input. Some of the observatories and space telescopes use other variations and detection methods specific for the internal conditions that are not efficient generally yet. For the photometric tasks simple aperture photometry is automated and used in most cases instead of profile (PSF) photometry except the dense crowded stellar fields and complicated objects (like galaxies). The reason is the difficulty with the image PSF extraction.

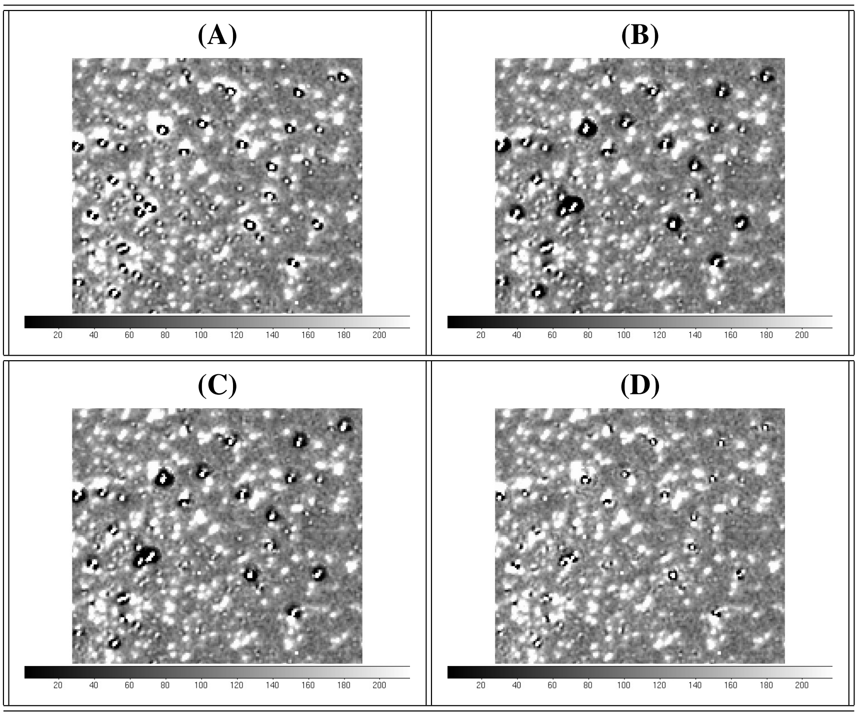

Table 2: Comparison of the subtracted image from the original figure 4.5.4. Occuring residua are evident.

(A) Only the analytic function is used to compute the PSF model. The PSF model is constant over the image.

(B) The analytic function and one look-up table are used to compute the PSF model. The PSF model is constant over the image.

(C) The analytic function and three look-up tables are used to compute the PSF model. The PSF model is linearly variable over the image, with terms proportional to 1, x and y.

(D) The analytic function and six look-up tables are used to compute the PSF model. The PSF model is quadratically variable over the image, with terms proportional to 1, x, y, x^2, xy, y^2.

5 Deconvolution algorithms used in astronomy

Convolution $*$ is linear mathematical operator. One of its advantages is its application in the dual space. Convolution of two functions becomes simple multiplication in the Fourier domain. If we define Fourier transform in one dimension of the given function $f(x)$ as

$$\hat{f}(\chi) = \frac{1}{\sqrt{2\pi}} \int_{\mathbb{R}} f(x) \exp^{-2\pi i \chi x} dx \tag{7}$$

and suppose $g(x)$ as the convolution of two functions $f_1(x)$ and $f_2(x)$

$$g(x) = (f_1 * f_2)(x) \tag{8}$$

then its Fourier transform is the multiplication of $\hat{f}_1(x)$ and $\hat{f}_2(x)$

$$\hat{g}(\chi) = \hat{f}_1(\chi)\hat{f}_2(\chi). \tag{9}$$

Deconvolution is trying to restore the image that has been degraded to its original condition [57]. If the PSF is unknown then ”Blind deconvolution”, the method widely used in the image processing, can be proceeded [15]. That is useful for the texture-type objects of the measurements with high SNR like planets or the Moon, but valuable information can be lost during the process in the case of the precise astrometric or photometric measurements. If the PSF is known (or at least approximated), one could suggest the use of the equations (8, 9, 3) to obtain the estimation of the original image from using the Inverse Fourier Transform of

$$\hat{O}(\chi, \psi) = \frac{\hat{R}(\chi, \psi)}{\hat{P}(\chi, \psi)} - \frac{\hat{N}(\chi, \psi)}{\hat{P}(\chi, \psi)}. \tag{10}$$

This is called *Fourier-quotient method* [57], but for the frequencies approaching the cutoff, the noise term grows on importance. In practice this method cannot be therefore in the presence of noise (all experimental cases) used. Even if the noise is slight (which is rarely in the astronomical observations) there is no guarantee that the inverse convolution (or ”deconvolution”) kernel exists [7]. Such a case described by (3) is an ill-posed problem with no unique and no stable solution [57].

Even though the convergence of the deconvolution in astronomy is not guaranteed and many of the methods diverge in general, some progress can be made using several constraints and limits. For example assumption that all the light from the single star falling on the detector in the photometric (not interferometric or spectroscopic) observations origins from the point source due to the large distances and corpuscular-wave dualism ability of the light. Another constraint can be made knowing the background values of the processing images providing the one-sided limit to the deconvolving algorithms.

5.1 Bayes approach

Using the variables defined in the head of this section the Bayesian approach constructs following probability density relation

$$p(O|R) = \frac{p(R|O)p(O)}{p(R)} \tag{11}$$

to maximize its right term [15].

5.1.1 Gaussian noise

If the observational object (original image) and noise is assumed to follow Gaussian distribution with zero mean then a solution of (11) leads to the *Wiener filter* [57]

$$\hat{O}(\chi, \psi) = \frac{\hat{P}^T(\chi, \psi)\hat{R}(\chi, \psi)}{|\hat{P}(\chi, \psi)|^2 + \frac{\sigma_N^2}{\sigma_O^2}}, \tag{12}$$

where σ_O is standard deviation of the original image and σ_N is the standard deviation of the Gaussian noise. The application of the Wiener filter is fast, but it needs quite precise spectral noise estimation. Its big disadvantage for the astronomical purposes is that the noise of the data from the digital sensors (e.g. CCD) produced by the falling photons is distributed correspondingly to those photons according to the Poisson distribution.

5.1.2 Poisson noise

Using the equation (11) and the assumption of the noise behaving according to the Poisson distribution the probability $p(R|O)$ is [57]

$$p(R|O) = \prod_{x,y} \frac{((P * O)(x, y))^{R(x,y)} e^{-(P*O)(x,y)}}{R(x, y)!}. \tag{13}$$

The maximum given by the derivative of the logarithm of (13) leads to the result [57]

$$1 = \frac{R(x, y)}{(P * O)(x, y)} * P^T. \tag{14}$$

This equation is afterwards used for the construction of the iterative Richardson-Lucy algorithm as described in the following section.

5.2 Iterative regularized methods

Further description of the deconvolution methods are based on the successive approximations in small steps eventually (not always) converging to the estimation of the original non-degraded signal.

5.2.1 Noise-less iteration

Let's use the term from (3) to define ”idealistic” noise-less blurred signal $I(x, y)$ which was captured by the detector

$$I(x, y) = (P * O)(x, y), \tag{15}$$

where $P(x, y)$ is PSF and $O(x, y)$ represents non-degraded original signal (non-blurred stellar light without noise). The difference between the noise-less blurred signal $I(x, y)$ and the captured real signal $R(x, y)$ is nothing more than the noise $N(x, y)$. If we set the condition that the noise is negligible then in the simplest (non-realistic) form the equation (3) changes to

$$0 = R(x, y) - I(x, y). \tag{16}$$

Adding the original signal $O(x, y)$ on the both sides we get

$$O(x, y) = O(x, y) + [R(x, y) - I(x, y)]. \tag{17}$$

By performing the operations on the right side of (17) we can iteratively compute a ”new version” of the original image $O^{(n+1)}(x, y)$ on the left side of the same equation [7]. Using the degraded CCD image $R(x, y)$ as the first iteration to seed the process we compute better and better estimation with another iteration assuming the ”correction term” $[R(x, y)-I(x, y)]$ is small in comparison with $O(x, y)$ (meaning the original signal was not degraded so terribly). The single iteration steps are therefore

$$O^{(n+1)} = O^{(n)} + [R - (P * O^{(n)})] \tag{18}$$

and sending $\lim\limits_{n\to\infty}$ we get back to $O = O + R - (P * O)$ and $R = (P * O)$, the noise-less blurred degradation from (3). However in the presence of the noise the algorithm in general diverges and the successive ”correction terms” may grow up instead of decreasing.

5.2.2 Van Cittert method

This method [64] is actually only the modification of the previous one providing the relaxation parameter α into (18)

$$O^{(n+1)} = O^{(n)} + \alpha[R - (P * O^{(n)})], \tag{19}$$

which allows to control the rate at which the iteration converges to the estimation of the original signal. If $\alpha < 1$ then only the part of the ”correction term” is added to the new iterated estimation and the method approaches the estimation of the original signal more slowly. That is more valuable if we replace scalar α parameter by the relaxation function $\alpha(O^{(n)}(x,y))$ [7]. The rate of convergence should be slowed for the noisy low-value background pixels, while allowing the low-noise pixels (bright stars) run at full speed. The relaxation function could be for example the sine function with arguments between 0 and $\pi/2$. Jansson [30] modified this technique by assuming the constraints on each iteration step. Commonly used constraints [57] are

- positivity - pixels on every new signal estimation have to be nonnegative,
- upper and lower bounds (e.g. background values of the image) or
- known spatial domain in the dual Fourier space.

5.2.3 Landweber method

In 1951 Landweber [37] presented the successive approximations based on maximum likelihood estimation of the signal with Gaussian noise [57]. During each iteration same constraints as discussed in the previous method can be used. The iteration uses additional convolution with transposed PSF $P^T(x,y)$ and relaxation parameter γ :

$$O^{(n+1)} = O^{(n)} + \gamma P^T * [R - (P * O^{(n)})]. \tag{20}$$

5.2.4 Richardson-Lucy method

While the Van-Cittert or Landweber methods are based on the additive correction, the Richardson-Lucy (or sometimes Lucy-Richardson) method, first presented in 1972 [54], uses the multiplicative correction [7]. One of its form [57] using the maximum likelihood results of Bayesian methodology given in (14) can be written as

$$O^{(n+1)} = O^{(n)} \left[\frac{R}{(P * O^{(n)})} * P^T \right]. \tag{21}$$

This algorithm is, due to the assumption of the Poisson noise distribution and resulting flux preservation, commonly used in astronomical data processing.

5.3 Analysis of standard deconvolution methods in the case of crowded field

In this subsection standard image processing algorithms as described above are tested on 2 different astronomical images 8 and 9. The figure 8 contains simple non-complicated stellar field around the variable star V795 Her in the constellation of Hercules [56], while the figure 5 contains complicated

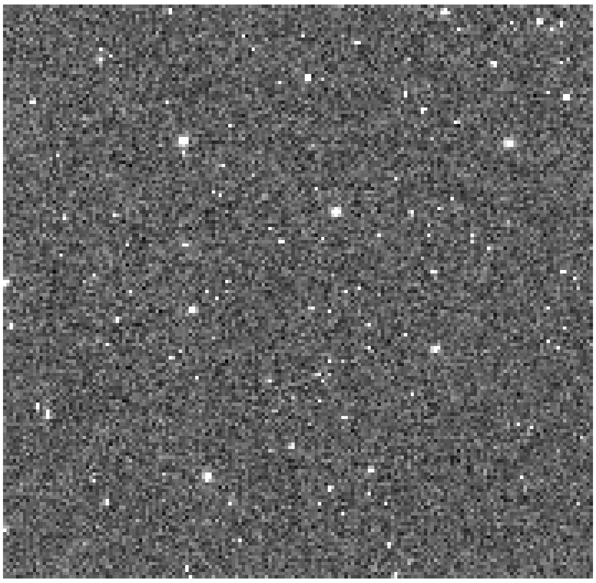

Figure 8: Astronomical image of the non-complicated stellar field around the variable star V795 Her.

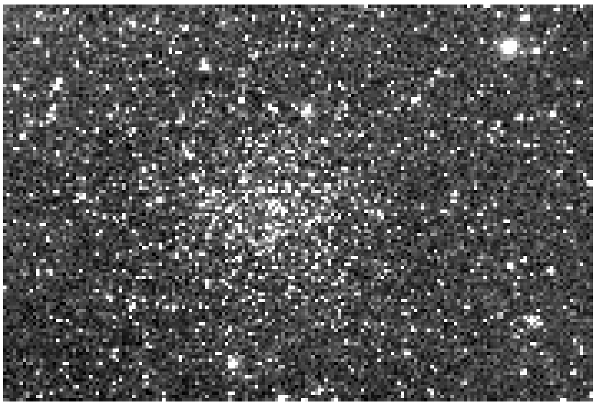

Figure 9: Astronomical image of the complicated crowded field of the stellar cluster NGC6791.

Table 3: Properties of the astronomical images used for the tests of the standard deconvolution algorithms

	V795 Her	NGC6791	
right ascension α	17 12 56.09	19 20 53	[$^{\mathrm{h\ m\ s}}$]
declination δ	+33 31 21.4	+37 46.3	[° ’ ”]
constellation	Hercules	Lyra	
date of exposition	2009-04-29	2008-04-01	[yyyy-mm-dd]
time of exposition UT	00:30:41	21:08:48	[hh:mm:ss]
image size	1056 x 1027	1092 x 736	[px]
exposure	20	30	[s]
photometric filter	V	R	
CCD camera	FLI IMG4710	G2-3200	
telescope diameter	50	65	[cm]
temperature during exposition	-40	-35	[° C]
sky value (background)	74	748	[ADU]
σ of the sky background	8.5	26	[ADU]
typical FWHM of bright stars	3.7	3.0	[-]

stellar crowded field of the cluster NGC6791 in the constellation of Lyra. Characteristics and properties of both testing images can be seen in the table 3.

In figure 10 there is the comparison of 3 iterative deconvolution methods described above (Van Cittert, Landweber, Richardson-Lucy). 3 matrices $M_{1,2,3}$ were convolved with simple symmetric PSF and deconvolved back with those three different algorithms. The dependence of RMSE (based on the difference between original and reconstructed signal) on the number of iterations can be seen on the graphs.

$$M_1 = \begin{pmatrix} 1 & 1 & 1 & 1 & 1 & 1 & 1 & 1 & 1 & 1 & 1 & 1 & 1 \\ 1 & 1 & 1 & 1 & 1 & 1 & 1 & 1 & 1 & 1 & 1 & 1 & 1 \\ 1 & 1 & 1 & 1 & 1 & 1 & 1 & 1 & 1 & 1 & 1 & 1 & 1 \\ 1 & 1 & 1 & 1 & 1 & 1 & 1 & 1 & 1 & 1 & 1 & 1 & 1 \\ 1 & 1 & 1 & 1 & 1 & 1 & 1 & 1 & 1 & 1 & 1 & 1 & 1 \\ 1 & 1 & 1 & 1 & 1 & 1 & 1 & 1 & 1 & 1 & 1 & 1 & 1 \\ 1 & 1 & 1 & 1 & 1 & 1 & 100 & 1 & 1 & 1 & 1 & 1 & 1 \\ 1 & 1 & 1 & 1 & 1 & 1 & 1 & 1 & 1 & 1 & 1 & 1 & 1 \\ 1 & 1 & 1 & 1 & 1 & 1 & 1 & 1 & 1 & 1 & 1 & 1 & 1 \\ 1 & 1 & 1 & 1 & 1 & 1 & 1 & 1 & 1 & 1 & 1 & 1 & 1 \\ 1 & 1 & 1 & 1 & 1 & 1 & 1 & 1 & 1 & 1 & 1 & 1 & 1 \\ 1 & 1 & 1 & 1 & 1 & 1 & 1 & 1 & 1 & 1 & 1 & 1 & 1 \\ 1 & 1 & 1 & 1 & 1 & 1 & 1 & 1 & 1 & 1 & 1 & 1 & 1 \end{pmatrix} \tag{22}$$

$$M_2 = \begin{pmatrix} 1 & 1 & 1 & 1 & 1 & 1 & 1 & 1 & 1 & 1 & 1 & 1 & 1 \\ 1 & 1 & 1 & 1 & 1 & 1 & 1 & 1 & 1 & 1 & 1 & 1 & 1 \\ 1 & 1 & 1 & 1 & 1 & 1 & 1 & 1 & 1 & 1 & 1 & 1 & 1 \\ 1 & 1 & 1 & 100 & 1 & 1 & 1 & 130 & 1 & 1 & 1 & 1 & 1 \\ 1 & 1 & 1 & 1 & 120 & 1 & 1 & 1 & 1 & 1 & 1 & 1 & 1 \\ 1 & 1 & 1 & 1 & 1 & 1 & 1 & 1 & 1 & 1 & 1 & 1 & 1 \\ 1 & 1 & 1 & 1 & 1 & 1 & 1 & 1 & 1 & 1 & 1 & 1 & 1 \\ 1 & 1 & 1 & 1 & 1 & 1 & 1 & 1 & 1 & 1 & 1 & 1 & 1 \\ 1 & 1 & 1 & 1 & 1 & 1 & 1 & 1 & 1 & 1 & 1 & 1 & 1 \\ 1 & 1 & 1 & 1 & 140 & 1 & 1 & 1 & 200 & 1 & 1 & 1 & 1 \\ 1 & 1 & 1 & 1 & 1 & 1 & 1 & 1 & 1 & 1 & 1 & 1 & 1 \\ 1 & 1 & 1 & 1 & 1 & 1 & 1 & 1 & 1 & 1 & 1 & 1 & 1 \\ 1 & 1 & 1 & 1 & 1 & 1 & 1 & 1 & 1 & 1 & 1 & 1 & 1 \end{pmatrix} \tag{23}$$

$$M_3 = \begin{pmatrix} 1 & 5 & 1 & 8 & 1 & 6 \\ 2 & 2 & 3 & 3 & 4 & 4 \\ 8 & 7 & 8 & 2 & 4 & 9 \\ 1 & 6 & 7 & 8 & 1 & 5 \\ 8 & 1 & 5 & 5 & 5 & 9 \\ 9 & 4 & 5 & 8 & 9 & 5 \end{pmatrix} \tag{24}$$

Because of the unknown original image $O(x, y)$ from (3) one has to develop different method for the purposes of the deconvolution algorithms' comparison than just the formation of the estimations $O'(x, y)$ of the original image.

Let us construct the estimation of the original unblurred and denoised signal $O'(x, y)$ with any of the deconvolution method discussed above and with the series of the prefabricated PSFs $P(x, y)$. Then it would be simply possible to convolve such a estimation back into $R'(x, y)$ with the same PSF and compare it with the former real image $R(x, y)$. Unfortunately some of the deconvolution methods do

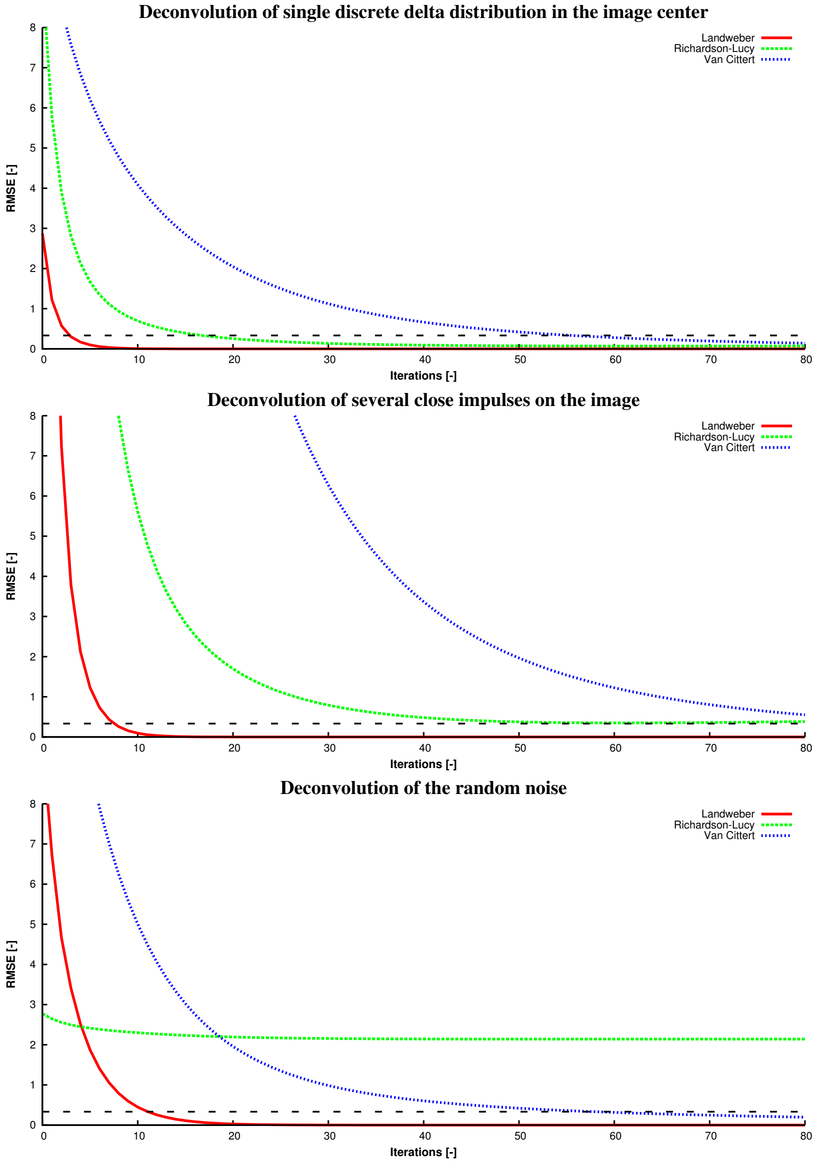

Figure 10: Comparison of Van Cittert, Landweber and Richardson-Lucy deconvolution methods in dependence on number of the iterations. The graphs from the top in sequence belong to the matrices $M_{1,2,3}$ defined in (22, 23, 24).

not preserve total flux and one have to normalize the resulted images. Such a normalization constant c_1 can be defined as

$$c_N = \frac{\sum_x \sum_y R'(x,y)}{\sum_x \sum_y R(x,y)}. \tag{25}$$

Then one of the metrics μ measuring the scale of the difference between

- the test image $R(x,y)$ and
- deconvolved and once again with the convolution reconstructed image $R'(x,y)$

can be defined as

$$\mu = \frac{1}{wh-1} \sum_x \sum_y \left(1 - \frac{R(x,y)}{c_N R'(x,y)}\right)^2, \tag{26}$$

where w and h are width and height of the image and c_N is the normalization constant (25). Such a metrics μ represents mean quadratic deviation (not standard deviation) between reconstructed and input signal and can be used as unbiased indicator of the efficiency (or error deficits) of the different deconvolution algorithms.

For the purposes of the tests several PSFs were constructed. Those were either analytic or semi-empiric - deducted with the profile photometry iterative method from the image 8 and 9 [17]. For each different variability across the test images (constant or space-variant PSF) automatic choice of the analytic function was used with the data reduction software IRAF[8] - those PSFs are boldfaced in the result tables 4 and 5. Even in the case of the semi-empiric PSFs with more look-up tables with primary analytic kernel the functions were in general

- Moffat (6) with different β parameters,
- Gauss (27),
- Lorentz (5)
- and Penny - Gaussian core with Lorentzian wings [49].

Deconvolution algorithms were implemented in the MATLAB[9] programming language. The comparison of the deconvolution methods with computed metrics μ (26) for the images 8 and 9 can be seen in the tables 4 and 5. The boldfaced PSFs represent the ones chosen by the IRAF software automatically as the most corresponding (square minimization) to the specific number of look-up tables.

---

[8] http://iraf.noao.edu

[9] http://www.mathworks.com/products/matlab/index.html

Table 4: Comparison of the Wiener (W), Van Cittert (VC), Landweber (L) and Richardson-Lucy (R-L) deconvolution methods for the testing image 8 (simple stellar field around V795 Her). The metrics μ is defined in (26). Boldfaced are the best fitting functions according to the automatic choice of IRAF software.

PSF	look-up tables	μ $[10^{-3}]$			
		W	VC	L	R-L
Moffat β = 3	0	22.00	12.87	304.08	12.23
Moffat β = 5	0	11.57	12.42	173.75	8.12
Moffat β = 7	0	9.39	12.10	89.13	11.54
Penny	0	18.18	12.59	12.59	7.75
Penny	1	5.37	12.52	12.52	7.34
Penny	3	5.36	12.52	12.52	7.33
Penny	6	4.80	12.49	12.49	7.25
Moffat β = 1.5	0	22.56	12.80	12.80	10.62
Moffat β = 2.5	0	20.65	12.62	12.62	8.03
Moffat β = 1.5	1	5.26	12.52	12.52	7.31
Moffat β = 2.5	1	5.28	12.52	12.52	7.33
Moffat β = 1.5	3	5.33	12.52	12.52	7.30
Moffat β = 2.5	3	5.31	12.52	12.52	7.32
Moffat β = 1.5	6	4.56	12.50	12.50	7.23
Moffat β = 2.5	6	4.69	12.49	12.49	7.24

Table 5: Comparison of the Wiener (W), Van Cittert (VC), Landweber (L) and Richardson-Lucy (R-L) deconvolution methods for the testing image 9 (crowded field of NGC6791). The metrics μ is defined in (26). Boldfaced are the best fitting functions according to the automatic choice of IRAF software.

PSF	look-up tables	μ [10^{-3}]			
		W	VC	L	R-L
Moffat β = 3	0	8.37	4.37	21.49	3.90
Moffat β = 5	0	3.02	4.02	18.55	1.79
Moffat β = 7	0	2.07	3.74	12.44	3.94
Moffat β = 1.5	0	9.99	4.38	4.38	3.42
Moffat β = 1.5	1	23.49	6.17	6.17	291.21
Lorentz	3	25.19	6.75	1736.14	2986.89
Penny	6	51427.40	2500091.10	22919.01	53934.23
Moffat β = 2.5	0	2.25	4.15	4.15	2.33
Moffat β = 2.5	1	18.25	5.18	5.18	37.00
Moffat β = 2.5	3	19.90	5.81	5.81	61.49
Moffat β = 1.5	3	10.61	4.43	7370.95	38.30
Moffat β = 2.5	6	1058.73	13.68	3343.19	9144.15

6 Imaging systems in astronomy with the need of crowded field image processing

In this section the list of several ongoing or planned astronomical experiments with their brief description is presented. The common feature of those projects is the absence of the effective algorithms solving the complicated image signal caused by some of the following effects :

- overlapping PSFs of nearby stellar sources (crowded fields),
- low SNR of the observed objects,
- low spatial signal sampling,
- and/or significant time or spatial dependence of the PSF.

6.1 Ground optical telescopes

6.1.1 BART

BART (figure 11) is a small intelligent robotic CCD telescope, devoted to rapid observation of prompt GRB transients [31]. Telescope is located in Astronomical Institute of the Czech Academy of Sciences in Ondrejov and was originally formed as a student project on the Charles University. The database of the observation includes the FITS images for over than 8 years and is waiting to be automatically processed to produce the photometric light curves of observed variable stars.

Figure 11: BART - Burst Alert Robotic Telescope in Ondrejov observatory (CZ)

6.1.2 D50

The D50 telescope (figure 12) is the second robotic telescope of High Energy Astrophysics department in Ondrejov observatory (CZ) [48]. It is located near the BART telescope. The goal was to build a

Figure 12: D50 - Robotic telescope in Ondrejov observatory (CZ)

low-cost alert telescope larger than the BART for the follow-up observing of GRBs and other interesting high-energy sources. The first light was captured in January 2008 and observations are not fully automated yet. The D50 is a Newtonian telescope with a primary parabolic mirror with a diameter of 500mm and a focal length of f=1.975m. The field of view is 20' x 20' with a resolution of 1.18" per pixel. The limiting magnitude of the main telescope in the V filter is 17.7^{mag} for 10 seconds of exposure time. The automated pipeline for data reduction of observed data would be necessary to fully robotize the telescope, while the goal is focused to optical transients of GRBs, which are faint and rapidly variable objects determined strongly by the noise while captured on CCD.

6.1.3 BOOTES

The Burst Observer and Optical Transient Exploring System (BOOTES) was considered as a part of the preparations for the ESA's satellite INTEGRAL and was developed Spain in collaboration with two Czech institutions [16]. The first light was obtained in July 1998. Today it consists of a net of robotic telescopes in Spain and New Zealand.

6.1.4 GLORIA

GLORIA is a citizen-science network of robotic telescopes, which would give free access and research to a virtual community via the Internet. GLORIA partners offer access to a growing collection of robotic telescopes via a Web 2.0 environment - 17 telescopes on 4 continents by the project's end. Many of

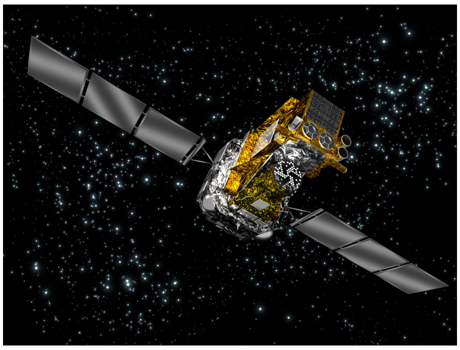

Figure 13: INTEGRAL - International Gamma Ray Astrophysics Laboratory (ESA)

the telescopes are already robotized using the same free/open-source RTS2 software [35] and the web access would be based on Ciclope Astro which currently provides the world's first free-access robotic telescope at Montegancedo Observatory[10]. The challenge is to involve people from around the world, to maximise their collective intelligence, and to foster their participation in astronomy research both in data analysis and actual observations. GLORIA is an e-Science network for the virtual community, demonstrating how networking and open e-Infrastructures can increase the quality of research.

6.1.5 MAIA

MAIA - double-station video observation of the meteor - is the project of both Czech Technical University and the observatory in Ondřejov [67]. The aim is to study sporadic meteors and less active meteor showers using the double station video experiment. The automatic instrumentation is developed within the project using commercial-off-the-shelf components. Simultaneously the methods of data recording, processing and storing will be prepared [4, 45, 20]. On the bases of recorded data the physical properties of the meteoroids belonging to the different populations of the sporadic background are studied.

6.2 X-Ray and γ-Ray space satellites - INTEGRAL

The ESA observatory INTEGRAL (International Gamma-Ray Astrophysics Laboratory) [70] is dedicated to the fine spectroscopy and fine imaging (angular resolution: 12" FWHM) of celestial γ-Ray sources in the energy range 15 keV to 10 MeV with concurrent source monitoring in the X-Ray (3-35 keV) and optical (V-band, 550 nm) energy ranges. INTEGRAL carries two main γ-Ray instruments, the spectrometer SPI optimized for the high-resolution spectroscopy (20 keV-8 MeV), and the imager IBIS optimized for high-angular resolution imaging (15 keV-10 MeV). Two monitors, JEM-X in the

---

[10] http://om.fi.upm.es

Figure 14: Project WILLIAM - Wide-field all-sky image analyzing monitoring system - run by Multimedia Technology Group of Czech Technical University.

(3-35) keV X-ray band, and OMC in optical Johnson V-band complement the payload. INTEGRAL was launched on 17 October 2002 and is still operating. The illustration of the INTEGRAL satellite is in figure 13. The complexity of the data reduction of faint and overlapping objects is described in [9, 10]. The participation of Czech team in the reduction of INTEGRAL data can be found in [28].

6.3 Small digital cameras

6.3.1 WILLIAM

Project WILLIAM[11] (Wide-field all-sky image analyzing monitoring system) is the prototype of the all-sky experimental camera for astronomical and meteorological support being currently developed in the Department of Radioelectronics of Czech Technical University (CTU) in Prague [29]. It provides additional support for bright astronomical phenomena, telescope controller and day/night meteorological conditions. The day weather conditions is being processed by the idea of colour segmentation [11] using the K-means algorithms [6] for various colour spaces other than RGB [65].

6.3.2 Astrophotography

The use of telescopes for GRB optical transients is limited by their speed to track the possible explosion on the sky as soon as possible. Therefore the use of cheap all-sky digital cameras combined in the worldwide net was suggested. The data reduction from those UWFC is mostly complicated by low spatial sampling of the signal and significant optical aberrations, both influencing the PSF and its

---

[11] http://william.multimediatech.cz

Figure 15: The all-sky camera image from the observatory Karlovy Vary.

spatial variance significantly. In figure 15 is the example of the image from the all-sky camera recently operating at the observatory Karlovy Vary.

In [50] it is discussed the use of low-cost digital cameras for the astronomical scientific purposes. Although lots of additional problems occur, the benefits of the gain of statistically enormous number of data cannot be overlooked.

7 GlencoeSim Simulator

For the purposes of testing the efficiency of any given deconvolution algorithm on different types of astronomical images, one has to compare the result (the positions and fluxes of astronomical objects) with the undegraded original conditions. Simulations of artificial astronomical fields provide a platform for such efficiency tests by providing the undegraded original conditions (stellar positions and fluxes), which can be statistically compared with the deconvolution results under many varying circumstances (e.g., PSF, noise or stellar spatial distributions and overlapping).

Developed GlencoeSim is a simulator of optical data of crowded stellar fields in the FITS format that is used in astronomy [12]. Its purpose is to create image simulations as similar as possible to realistic images from astronomical telescopes, while providing knowledge of the initial conditions (a map of stellar positions and fluxes). The GlencoeSim libraries and GUI can be downloaded from the webpages `mmtg.fel.cvut.cz/glencoe/` of the Multimedia Technology Group (MMTG) of the Czech Technical University in Prague. Implementation is being developed under the MATLAB/Octave platform [23, 19]. Similar tasks were traditionally widely performed by the IRAF astronomical package [61], with lower capabilities for random simulations and joined functional efficiency. The main strength of the MATLAB/Octave platform is its great matrix-computational advantage. All GlencoeSim functions can be used separately in any step of the algorithm, or together using GUI with a graphical check of the intersteps. The algorithm is illustrated in figure 16 in the form of a block diagram, and it can be divided into three basic steps - PSF acquisition, stellar map creation and noising. The red path in figure 16 shows the default settings in GUI, and it is recommended for simple simulations.

7.1 PSF acquisition in GlencoeSim

The `create_kernel_stellar_image.m` function prepares either a Moffat profile [46] or a Gaussian profile with given parameters or reads 2D data from an external FITS file. A given size of the resulting specific PSF radius and profile type parameters (α and β for Moffat, or σ for Gaussian) can be set. Moffat's radial profile is given by [46] in the equation (6 and the simplified Gaussian profile is given by

$$I(x,y) = I_0 e^{-\frac{x^2+y^2}{2\sigma^2}}. \tag{27}$$

Either way the profile is normalized to a peak equal to one. An example of a given PSF made from a Moffat profile with $\alpha = 1.1$ and $\beta = 0.8$ is shown in figure 17.

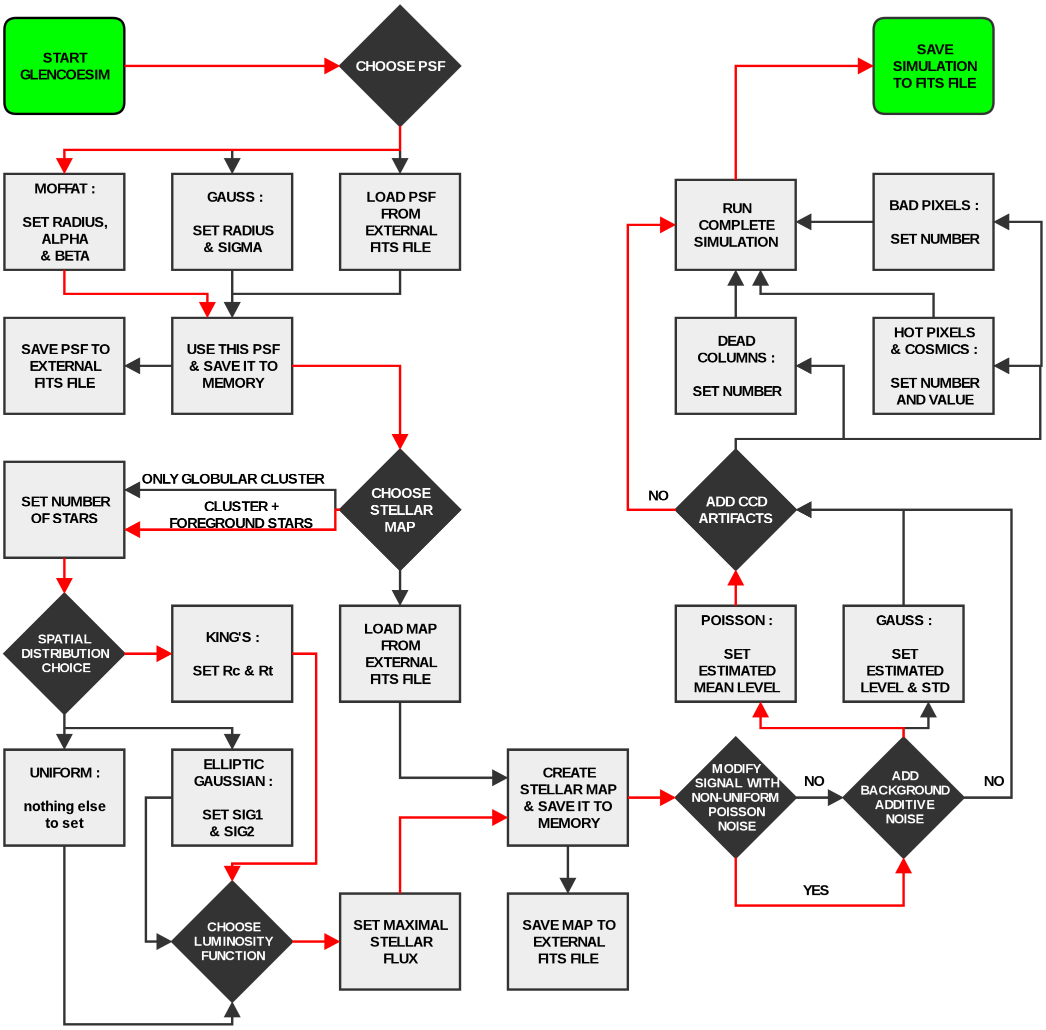

Figure 16: Block diagram of the GlencoeSim algorithm [12]. Red colour shows the basic recommended path, which is the default in GUI.

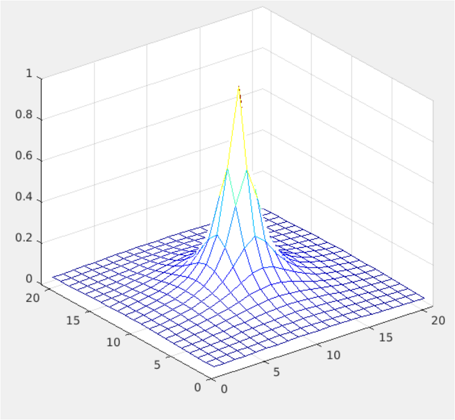

Figure 17: Example of Moffat PSF made by GlencoeSim with $\alpha = 1.1$ and $\beta = 0.8$.

7.2 Stellar map simulation in GlencoeSim

The `create_astro_positions.m` function makes a 2D map of random points with random intensities according to given constraints and parameters. They represent the undegraded positions and fluxes of simulated stars. As for the spatial stellar distribution, one can set either King's distribution [33], a 2D elliptic Gaussian distribution (both simulating the stellar Globular Cluster), or a uniform distribution representing random foreground stars not belonging to the globular cluster itself. GUI offers to prepare a stellar map including both cluster stars and uniformly distributed foreground stars at the same time. The cluster stars can be generated namely according to King's law of stellar surface density $f(r)$ [33]. It is implemented as

$$f(r) = k \left[\frac{1}{\sqrt{1 + \left(\frac{r}{R_C}\right)^2}} - \frac{1}{\sqrt{1 + \left(\frac{R_T}{R_C}^2\right)}} \right]^2 \tag{28}$$

with k as a normalization factor and R_C, R_T as functional parameters. R_C can be called the core radius, and R_T is a radius where the surface stellar density f goes to zero [33]. The other option is elliptic Gaussian spatial distribution, where parameters σ_x and σ_y control the ellipticity and the size of the distribution in the image center (μ_x, μ_y)

$$f(x, y) = k \exp\left(-\frac{(x - \mu_x)^2}{2\sigma_x} - \frac{(y - \mu_y)^2}{2\sigma_y} \right). \tag{29}$$

Stellar fluxes to an already created map can be randomly attached following different distributions. As a default, the measured luminosity function of the globular cluster M68 is attached to simulated point stars [43]. This luminosity function is shown in figure 18. The left part shows a semi-logarithmic

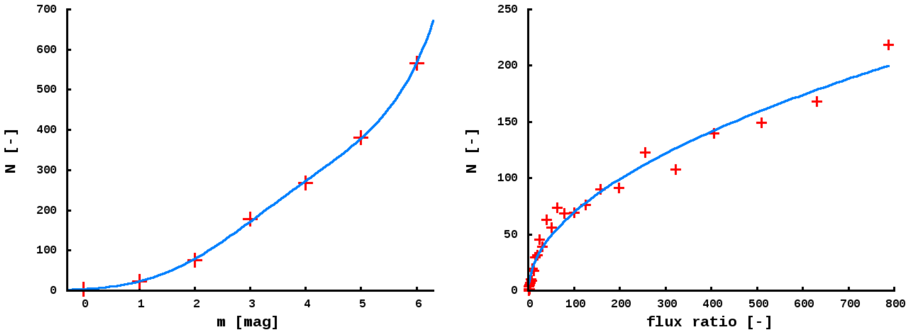

Figure 18: Luminosity function of Globular cluster M68 [43] used in GlencoeSim as a deafult flux distribution.

distribution in astronomical magnitudes as measured in [43] (with a fitted function of the fifth polynomial degree), and the right part shows the corresponding distribution of stellar counts N in dependence on flux ratio Φ

$$\Phi = \frac{I_{max}}{I(N)}. \tag{30}$$

The maximal flux value I_{max} has to be given to the simulator as a parameter. Such a representation is algorithmically easier, due to the good fit with a simple luminosity representation

$$N = k \cdot \Phi^P, \tag{31}$$

where the normalizing constant k depends on the given total amount of desired stars in the simulation and the shaping parameter $P = 0.513 \pm 0.025$. The simulator creates stars according to the fit (31) up to one thousand times fainter than the given I_{max} (which corresponds to the 6 magnitudes of measured data difference in [43]). Other options for the luminosity functions are uniform intensity distribution or exponential distribution with growth towards fainter stars. Again, any stellar map can be loaded from or saved into a FITS file [69].

7.3 Noise in GlencoeSim

Noise is the most important part of (3). This makes issues in deconvolution, especially since in astronomy the contribution of noise is extremely large, for example in comparison with image processing in car plate recognition. The simulator can separate the contribution of noise to astronomical images (which are mostly taken by cooled CCD cameras [27]) into 3 steps :

- non-uniform Poisson noise, dependent on the signal level modifying the stellar model itself,
- additive background noise, and

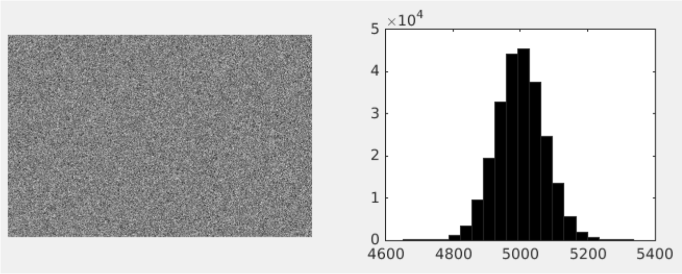

Figure 19: Example of noise with a Poisson distribution and a mean value of 5000 ADU.

- instrumental artifacts.

GlencoeSim [12] can disable noise completely, or can just simulate some of the steps independently.

Additive background noise made by the provided `create_background.m` function represents the total sum of the additive parts, such as CCD darkframe, the total background light contribution (atmospheric emission), and extremely faint unresolved astronomical phenomena (background galaxies, moonlight). The user has to choose between desired types of additive noise - Poisson noise (with only the estimated mean flux given) or white noise (Gaussian, with both estimated mean flux and standard deviation added to the algorithm).

The `create_simulation.m` function joins the previous preparations together. It convolves the sky model (a map of both the globular cluster and optional contamination with foreground stars) with given PSF, modifies the signal (if desired) with non-uniform Poisson noise dependent on the signal level, and finally adds the additive noise from the previous paragraph. In GUI, the additive noise histogram, together with the stellar luminosity distributions in a semi-logarithmic histogram, can be visually checked. An example of an additive Poisson noise contribution with a mean value of 5000 ADU is shown in figure 19.

In most cases, this may be sufficient for deconvolution tests, and the simulation can be saved into a FITS file. However, real astronomical images from CCD cameras often contain damaged pixels or other instrumental artifacts. In the function called `create_instrumental_artifacts.m` GlencoeSim offers three types of image deterioration.

- Hot pixels & cosmics - hot pixels have higher dark current than their neighbours and have higher pixel values, while cosmic particles can form a ray of several overexposed pixels. Both effects are simulated in GlencoeSim with a given number of overexposed pixels (with a user-given level) and between one pixel (hot pixels) and three pixels in length in eight different random directions (cosmics).

- Bad pixels - a given number of pixels on random positions would get 0 ADU values.

- Dead columns - in real images, for both mechanical and electronic reasons, some of the columns of the pixels of CCDs have the same signal level in parallel vertical directions. To simplify the algorithm, GlencoeSim creates all the number of desired columns made of dead pixels with 0 ADU values.

7.4 GUI and examples

The package and its graphical interface can be downloaded online[12], and Matlab runtime is recommended. Detailed information can also be found in the help manuals of the functions themselves. Two examples of simulation with different parameters are shown in figures 20 and 21. The first image shows a simulation of GCl with good seeing parameters and a high signal-to-noise ratio, while in image 21 there is a detail of blurred and dense GCl with a high number of faint background stars and an extremely low signal-to-noise ratio. Such a simulation is an example of the test image for deep analysis of the efficiency of potential new deconvolution methods. A detail of an example made by the default GUI settings with added instrumental artifacts (cosmic rays, hot pixels and dead columns) is shown in figure 22.

---

[12] http://mmtg.fel.cvut.cz/glencoe

Table 6: Default values and explanations of the most important global parameters in GlencoeSim simulator [12]

	Default value	Description
ImageRows	600	Size of the simulated image (Y)
ImageCols	800	Size of the simulated image (X)
MaxClusterIntens	40000	The top limit for the point stellar flux of single stars - I_0 in (6) or (27) - in the yet non-blurred not-noised simulated map of point stars in the cluster spatial distribution (stars of globular cluster).
SimClusterStars	8000	Estimated number of the stars in the GCl
SimForegrStars	100	Estimated number of the foreground stars
MaxForegrStars	20000	The top limit for the stellar flux of single stars - I_0 in (6) or (27) - in the yet non-blurred not-noised simulated map of point foreground stars in the uniform spatial distribution
SpatialDistrib1	150	R_C of King's spatial distribution (28) or σ_x of Gaussian spatial distribution (29)
SpatialDistrib2	400	R_T of King's spatial distribution (28) or σ_y of Gaussian spatial distribution (29)
NoiseIntensity	10000	Estimated value of mean additive noise (Poisson or Gaussian)
NoisseGaussStd	200	Estimated standard deviation of additive noise (only for Gaussian noise)
StellarKernelRad	10	Half of the size (square radius) of simulated PSF
Alpha	5	α parameter from Moffat PSF (6)
Beta	7	β parameter from Moffat PSF (6)
Sigma	4	σ parameter from Gaussian PSF (27)
HotpixCount	0	Number of hot pixels
HotpixFlux	65535	Flux of the hot pixels
BadpixCount	0	Number of bad pixels (0 value)
DeadCols	0	Number of dead columns
SignalPoisson	1	modification of the signal by the non-uniform Poisson noise dependent on the signal level

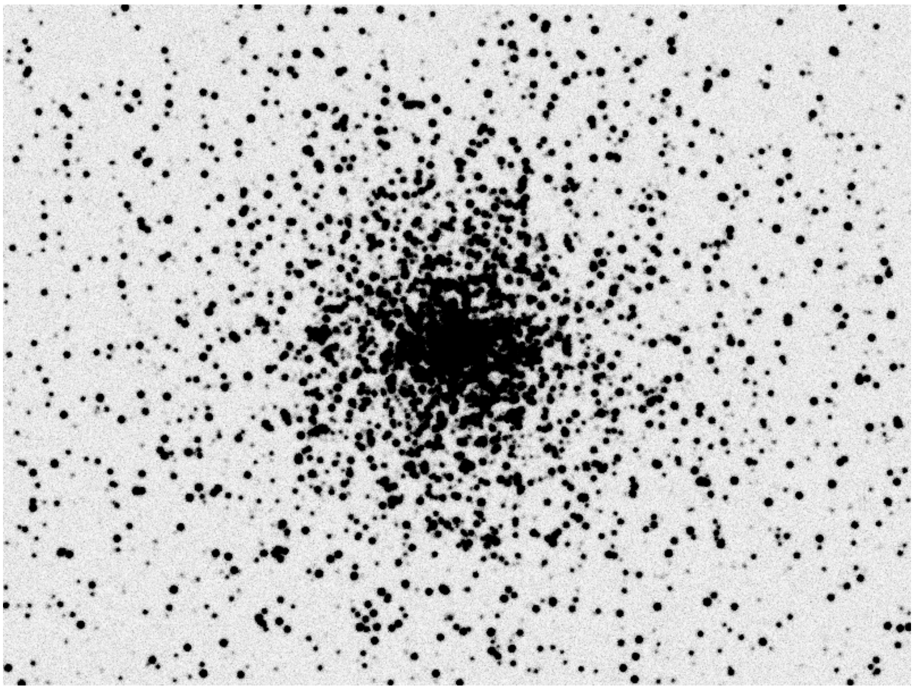

Figure 20: Example of GlencoeSim simulation (inverted colours). PSF radius 100 px, Moffat approximation $\alpha = 3.9$ & $\beta = 4.1$, King's distribution with $R_C = 160$ & $R_T = 800$, 6000 estimated stars in GCl and 2000 estimated stars of Universe background, exponential luminosity function, maximal single stellar flux of 4000 ADU and mean overall Poisson noise contribution of 2000 ADU with stellar flux corrupted with signal-dependent Poisson noise.

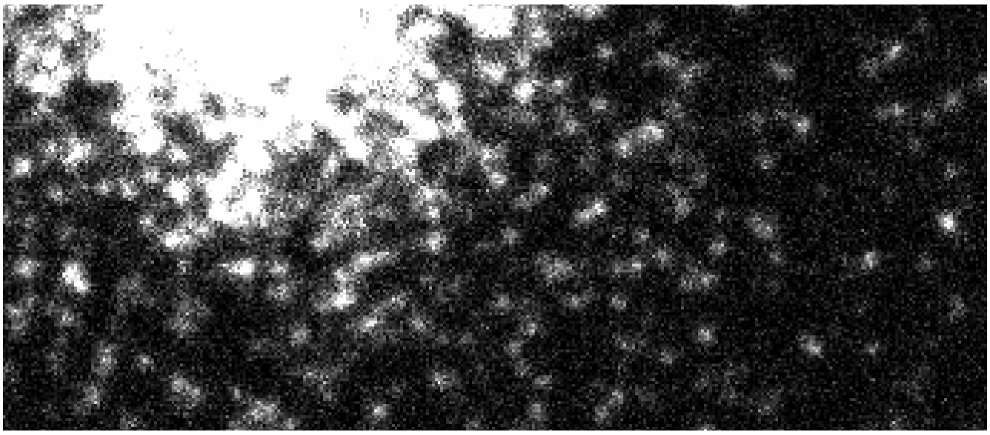

Figure 21: Simulation of complicated degraded GCl - detail of an extremely noisy and blurred signal in the periphery of the simulation. PSF radius 100 px, Moffat approximation $\alpha = 5$ & $\beta = 3$, King's distribution with $R_C = 80$ & $R_T = 500$, 15000 estimated stars in GCl and 5000 estimated stars of foreground stellar contamination, exponential luminosity function, maximal individual stellar flux of 500 ADU and a mean overall Poisson noise contribution of 10000 ADU with stellar flux corrupted with signal-dependent Poisson noise.

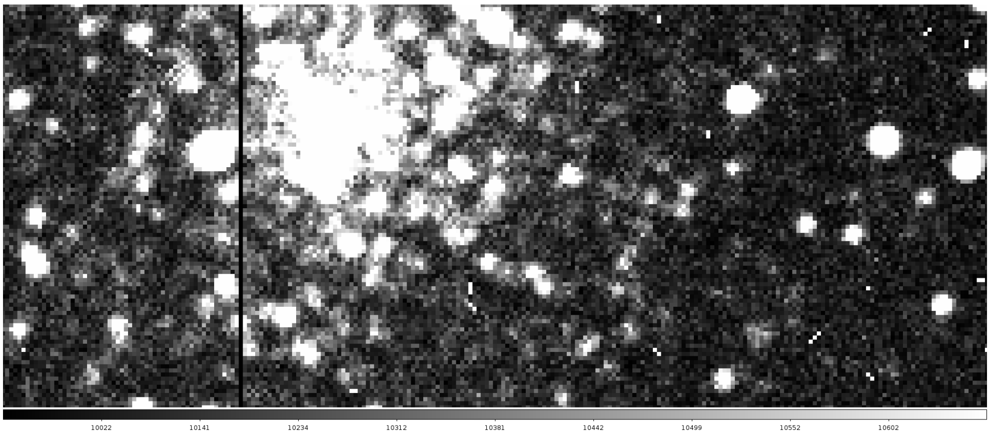

Figure 22: Simulation of complicated degraded GCl - PSF radius 10 px, Moffat approximation $\alpha = 5$ & $\beta = 7$, King's distribution with $R_C = 150$ & $R_T = 400$, 8000 estimated stars in GCl and 100 estimated stars of foreground stellar contamination, luminosity function of M68, maximal single stellar flux of 40000 ADU noised by non-uniform Poisson modification and the mean overall additive Poisson noise contribution of an estimated mean level of 10000 ADU. The detail shows a dead column and several hot pixels and cosmic particles.

8 Astronomical image simulations

In this chapter, the creation of image simulations for many various conditions is described. These simulations would be used for deconvolution tests based on the initial knowledge of stellar fluxes and positions. For this purpose the author's simulator GlencoeSim (described in the previous section) was used [12]. The following analysis would be including statistical dependence and data mining in the space of various input and output parameters on which the simulations were created (or deconvolved, or proceeded by astrometry and photometry, ...).

8.1 Variable input parameters

From (3) according to [15] the resulting simulation generally (beside other minor influences) consists of 3 main steps:

- **INITIAL MAP** - point stellar positions with attached fluxes according to specific spatial distribution,
- **BLURRING** - described by PSF, in the simple case spatially invariant
- **NOISE** - given by two parts - additive noise and non-uniform Poisson modification of a stellar signal.

The initial simulated maps were chosen to be distributed by King's distribution [33] with various number of stars and various maximal values of flux with randomized fluxes according to the luminosity distribution of GCl M68 [43] as given by (31) in the figure 18. The maximal fluxes were set to 64, 1024, 16384 and 65536 ADU (Analog-Digital unit - quantization step representing the instrumental flux). The number of stars was similarly set to four options - 64, 1024, 16384 and 65536 estimated stars around the image. The spatial distribution is dependent on two King's parameters - the core radius R_C having the values of 50, 100 and 150 pixels and the zero surface stellar density R_T having the values of 150, 300, 450 and 600 pixels. Those values have been chosen regarding the attributes of the simulated images having 400x300 pixels size. It is important to keep in mind that the number of the estimated stars is not the real number of stars at the simulation (statistically some stars can be distributed behind the edge of the image). All these combinations make 4 (flux) x 4 (stars) x 4 (R_T) x 3 (R_T) = **192 simulated maps** files occupying just 2.6 MB of a hard drive space.

For the various PSFs the Moffat function shape from 6 was chosen with variable parameters α (influencing "fatness" of PSF) having 2, 4, 6, 8 and 10 values and the second parameter β (influencing the "sharpness" of PSF) having the values of 1.5, 2, 2.5, 3, 3.5, 4, 4.5, 5. The radius of PSF (half of the

Table 7: List of combinations for noising of simulations

estimated mean value [ADU]	estimated deviation [ADU]	non-uniform Poisson noise
0	0	no
0	0	yes
4	2	yes
16	4	yes
64	8	yes
256	16	yes
1024	32	yes
4096	64	yes
16384	128	yes
65536	256	yes

kernel/PSF size) is set to 25 pixels. That combination makes 40 simulated images of various PSF FITS files occupying just 300 kB of a hard drive.

The most important part influencing the efficiency of the deconvolution is the noise - both the level of additive noise and if the signal is modified by non-uniform Poisson noise. Eight additive noise (”darkframes”) following the Poisson distribution 41 were created, while for the simulation tests and comparisons it is useful to include the options when no additive noise is added with both the cases when the original signal is modified AND unmodified by non-uniform Poisson noise. Table 7 is showing the summary of the all 10 noise combinations considered for following simulations.

If combined with each other all 40 PSFs, 10 noise options and 192 initial maps create totally **76800 simulated FITS images occupying 14.8 GB** of space on hard drive. These simulations together with all darkframes, maps and simulations can be found at the address of MMTG group[13]. The preview of all conditions under which the simulations were created by the GlencoeSim simulator [12] can be seen in figure 8.

8.2 Methodics for comparison of deconvolution results with simulations

As discussed at the beginning of the thesis in the state of the art, the valuable information for scientific purposes are namely positions (astrometry) and flux measurements (photometry), so the algorithm

---

[13] http://dbq.multimediatech.cz/users/blazek/public/thesis

Table 8: List of all presets and variable settings combinations for all 76800 simulations created by GlencoeSim [12]

Fixed parameters :	
Image size	400x300 px
PSF type	Moffat (6)
PSF kernel size (radius)	50 px (25 px)
Spatial distribution	King's [33]
Luminosity function	M68
Estimated foreground stars	0
Hot & bad pixels, dead columns	0
Variable parameters :	
PSF α	2, 4, 6, 8, 10
PSF β	1.5, 2, 2.5, 3, 3.5, 4, 4.5, 5
Number of estimated GCl stars	64, 1024, 16384, 65536
Maximal initial stellar flux	64, 1024, 16384, 65536
R_C King's core radius	50, 100, 150
R_T King's zero surface density	150, 300, 450, 600
Additive noise (darkframes)	0,4,16,64,256,1024,4096,16384,65536
Non-uniform Poisson noise	yes & no (see table 7)

quality analysis have to focus on these two tasks. The first deconvolution efficiency tests should make it easier with already perfectly known PSF, yet the result is not secure due to the noise and the deconvolution method itself (which sometimes fails and sometimes not). The reason for following analysis is to find out the dependencies of the efficiency of selected deconvolution methods (as described in previous sections) on the parameters under which the simulations were created. This would help to enhance the strength and to eliminate the weakness of any following algorithms.

As for positioning the deconvolution tests in the following analysis have it ”easy” as they know the correct PSF for each simulation, so the registration of stars between the initial map and the result of the deconvolution can have an extremely tight number of the degrees of freedom in the spatial accuracy. As the fluxes and stellar densities vary extremely through all the simulations there is no ”general” automatic astrometric method [57] to objectively compare all the analysed options (as one would like to get for instance the spatial differences between the initial and deconvolved positions) - the aperture would have to vary as well depending on the noise and α Moffat parameter [46]. So the simple aperture astrometry would not compare the efficiency of the deconvolution itself, but rather the efficiency of following ”aperture astrometry settings for each condition”, which is not our task. So let’s look rather on the efficiency of the deconvolution methods to ”point the faint correct stars out and to eliminate the fake discoveries”. For that we will be looking more at ”tendencies in the efficiency” in the dependence on various change of parameters to get the idea of the influence of these parameters in the case of crowded fields (GCl).

Three options can happen in general (and mostly their mix) after the deconvolution :

- some stars were registered correctly between the result after the deconvolution and the initial map,
- some stars from the initial map (mostly the faint ones) were not recognized in the result after the deconvolution. This depends strongly on the method of astrometric registration (flux thresholding, aperture size, local surrounding noise estimation, peak finding method - 4-neighbours, 8-neighbours, local maxima, ...), but as we are not looking for the values themselves and much more focused on the tendencies in different deconvolutions then these presets can be fixed.
- And some stars can be found after the deconvolution which were never in the initial map (from the reasons discussed in the previous bullet).

So for the following analysis these parameters will be used for objective quality assessment:

- **Mapped stars** N_*- How many stars were counted in the initial map (there are 192 different unblurred unnoised maps simulated by GlencoeSim).

- **Found stars** N_{OK} - How many stars were registered and identified together between the initial map and the analysed deconvolution result.
- **Missing stars** N_{NOT} - How many stars from the initial map of point stars were not found in the result after deconvolution.
- **Fake stellar discoveries** N_{OVER} - How many indwelling fake stars were "discovered" in the deconvolution results not being in the initial map.

For the comparisons of different simulations (with different numbers of stars) much more interesting is to use following ratios

$$\frac{N_{OK}}{N_*}, \frac{N_{NOT}}{N_*} \text{ and } \frac{N_{OVER}}{N_*}.$$

When regarding the efficiency of the deconvolution method in the term of photometric (flux) measurements one has to use some statistic method due to the large number of individual stars, maps and noise combinations. From (1) it is evident that the magnitude difference (so-called differential photometry) or appropriate flux ratio is the important information for astronomers to scientifically analyse the data afterwards. It is logical as the light flux depends on the exposure time and the same two stars would have ideally (isolated, not noised conditions) twice higher measured flux with doubled exposure time, yet their ratio in ADUs would keep the same. From this argument it is easier to deal with the statistical analysis of the results after deconvolution process when comparing it with the point stars with attached point flux values in the initial maps. The values after deconvolution may vary a lot (depending on the deconvolution algorithm and its settings), yet in the ideal case overall the image the found and registered stars would have the values multiplied (or divided) by the same ratio compared to the initial map. This assumption is valid even regardless the photometric method used after deconvolution process (integration under fitted PSF, aperture photometry, peak values in the case of symmetric and spatially invariable PSF, ...).

Let the number of the registered stars on one deconvolved image be N_{OK} and the measured flux of each registered star i at one image is $F_{D,i}$. Then the total flux F_D of measured and *registered* stars (excluding not found mapped stars and fake discoveries) on one image would be

$$F_D = \sum_i^{N_{OK}} F_{D,i}. \tag{32}$$

Similarly, the flux of each corresponding star from the corresponding initial map would be $F_{M,i}$ and the total flux F_M of the registered stars (not all of them mapped!) would be

$$F_M = \sum_i^{N_{OK}} F_{M,i}. \tag{33}$$

Let define the ratio R between these two sums of the measured fluxes as

$$R = \frac{F_D}{F_M} \tag{34}$$

while keeping in mind that it does not include the stars which were originally in the map (mostly faint stars) nor the fake.

The **metrics** which would describe statistically the ”similitude between the photometric measurement results” for each simulation-deconvolution pair of images with simple factor can be similar to standard deviation of the flux measurements

$$\sigma^2_{MET} = \frac{1}{N_{OK}-1}\sum_{i}^{N_{OK}} \sigma_i^2, \tag{35}$$

where σ_i is the difference for each star i in one image between the flux of that star in the initial map $F_{M,i}$ and the measured flux $F_{D,i}$ in the deconvolved image adjusted properly by the ratio R that in the ideal case of hundred percent efficient deconvolution this difference would provide $\sigma_i = 0$ for all stars i. Each star would contribute to this metrics by following part

$$\sigma_i = F_{M,i} - \frac{F_{D,i}}{R}. \tag{36}$$

The important assumption is that the ”normalizing factor” R would correct the fluxes after deconvolution regardless the photometric method or their actual values. This is definitely not true in the case of spatially variable PSF or in the case of PSF with complicated shape (especially non-concave shape with unclear peak). However this does not apply in the case of our simulations and tests right now - the conditions of the simulations and following deconvolution efficiency tests (namely the known analytic PSF) allows us even to use just the peak values of found stars to be compared with the initial point values in the initial map. The proposed metrics σ_{MET} from (32, 33, 34, 35, 36) would then be

$$\sigma_{MET} = \sqrt{\frac{1}{N_{OK}-1}\sum_{i}^{N_{OK}}\left(F_{M,i} - F_{D,i}\frac{\sum_i^{N_{OK}} F_{M,i}}{\sum_i^{N_{OK}} F_{D,i}}\right)^2}. \tag{37}$$

Such a metric (single number for one combination of initial map - deconvolution result) includes the information about the number of accurate stars, photometric flux accuracy and the efficiency of deconvolution. Yet the values σ_{MET} from the tests with different maximal flux values have to be compared carefully - weighing is necessary, as the unit of σ_{MET} is in ADU (with maximal flux varying from 64 to 65536 ADUs in our simulations). It is important to keep in mind that the number of stars used in this metric is N_{OK}, not N_* as defined at the beginning of this section - the value is not ”smoochy” due to the extremely faint non-registered stars, yet the value itself is not absolute and depends on the astrometric results as defined at the beginning of this section. It can be used for the results processed under the same astrometric conditions as a relative indicator (showing the tendencies), not the absolute one.

8.3 Richardson-Lucy deconvolution of prepared simulations

This section describes the application of Richardson-Lucy (R-L) algorithm [54, 7] on the simulations created by GlencoeSim [12] under the various conditions (see Table 8). This standard algorithm was used according to the tests in the previous chapters (tables 4, 5 and the figure 10). The Wiener deblurring [57] is extremely dependent on the good estimation of the noise level (no automatization for 76800 calculations) and beside it counts with Gaussian white noise [23]. The number of iterations was chosen safe - 100 iterations - according to the results in the figure 10. For the deconvolution in this section the appropriate known PSF for each of 76800 simulations (various astronomical images) was used. For such a huge number of simulations it would be computationally overwhelming to try all different shapes of PSF for each simulation (it would provide 3 millions of images), while the task of this section is to see the dependence of R-L algorithm on the parameters of the simulator (number of stars, noise level, ...). The R-L deconvolution created **76800 images occupying 60.2 GB** of space on hard drive and the data can be found on the address[14].

The simulations and tests created over 230 thousands of the images, which is impossible to present all in this text. Therefore few examples can be seen in the figures 23, 24, 25, 26, 27 and 28. In all these figure the middle top 3D graph shows the fluxes and positions of the stars in the initial map, left bottom picture shows the FITS image of the convolved and blurred simulation and the right bottom FITS image shows the result after R-L deconvolution.

Figures 23 and 24 show the same initial map with the different level of noise in the simulation, producing different results after deconvolution. Figures 25, 26 and 27 show various simulations (and deconvolutions) with different spatial distributions and star numbers. The last example in the figure 28 shows the simulation with extremely high SNR. The variable conditions under which the simulations were created can be seen in the table 9.

8.4 Stellar registration

For our purposes the extractor of stars in the deconvolved images is based on 8-neighbour local peak maxima finder (symmetric and concave PSF assumption of the simulated data). Due to the reasons discussed in the section 8.2 (same PSF for simulation and deconvolution, ...) extremely tight positional conditions can be set to register the peaks from deconvolution results with the stars in the initial map - just one pixel difference of the peak position on the deconvolved image towards the original mapped position is allowed.

Extremely important (as always in any photometric or analysis) is setting of the signal threshold in the deconvolved images. Local peak maxima detector is generally extremely ”liberal” detector (com-

---

[14] http://dbq.multimediatech.cz/users/blazek/public/thesis

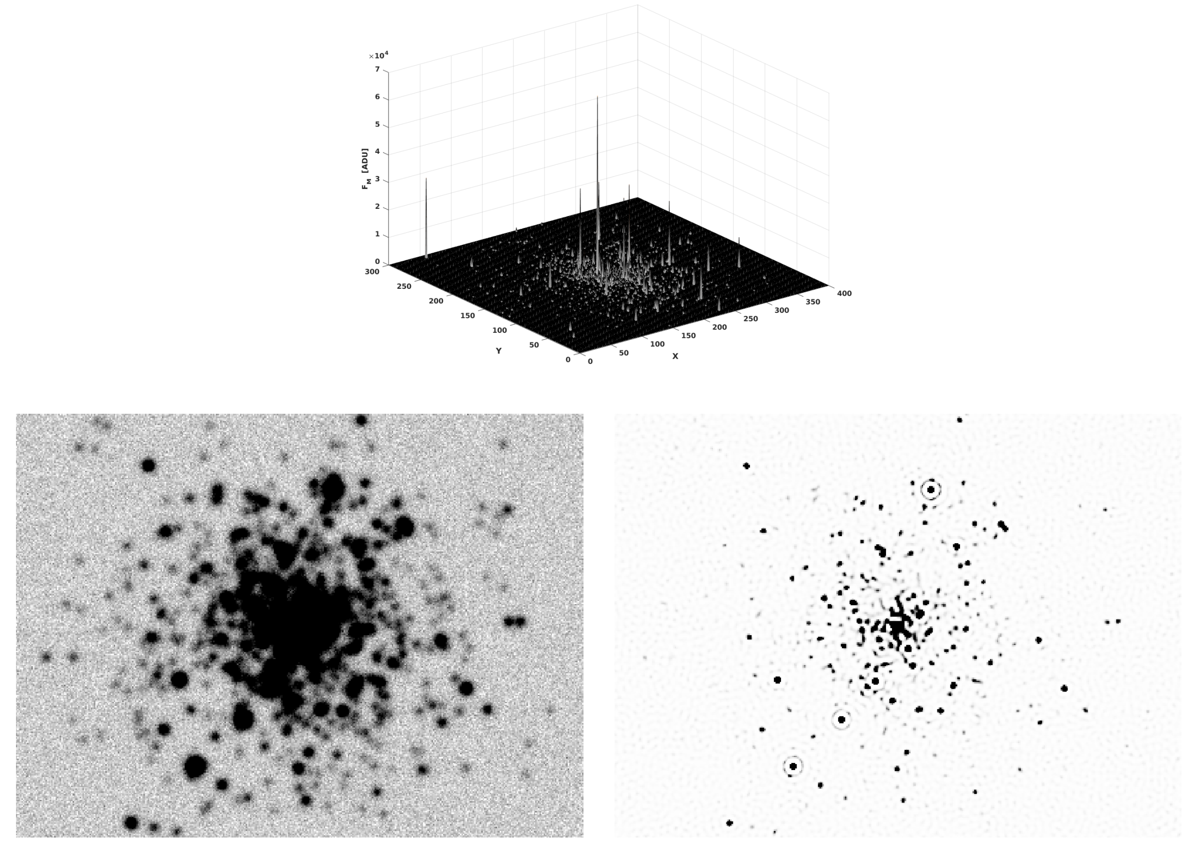

Figure 23: Example from GlencoeSim [12] and deconvolution results - initial point stellar map (top), blurred and noised simulation (bottom left) and simple R-L deconvolution result (bottom right). 1024 stars estimated with potential maximal flux 65536 ADU, Moffat PSF having $\alpha = 6$ and $\beta = 3.5$, King's spatial distribution with parameters $R_C = 100$ and $R_T = 300$. Additive Poisson noise has 65536 ADU mean level.

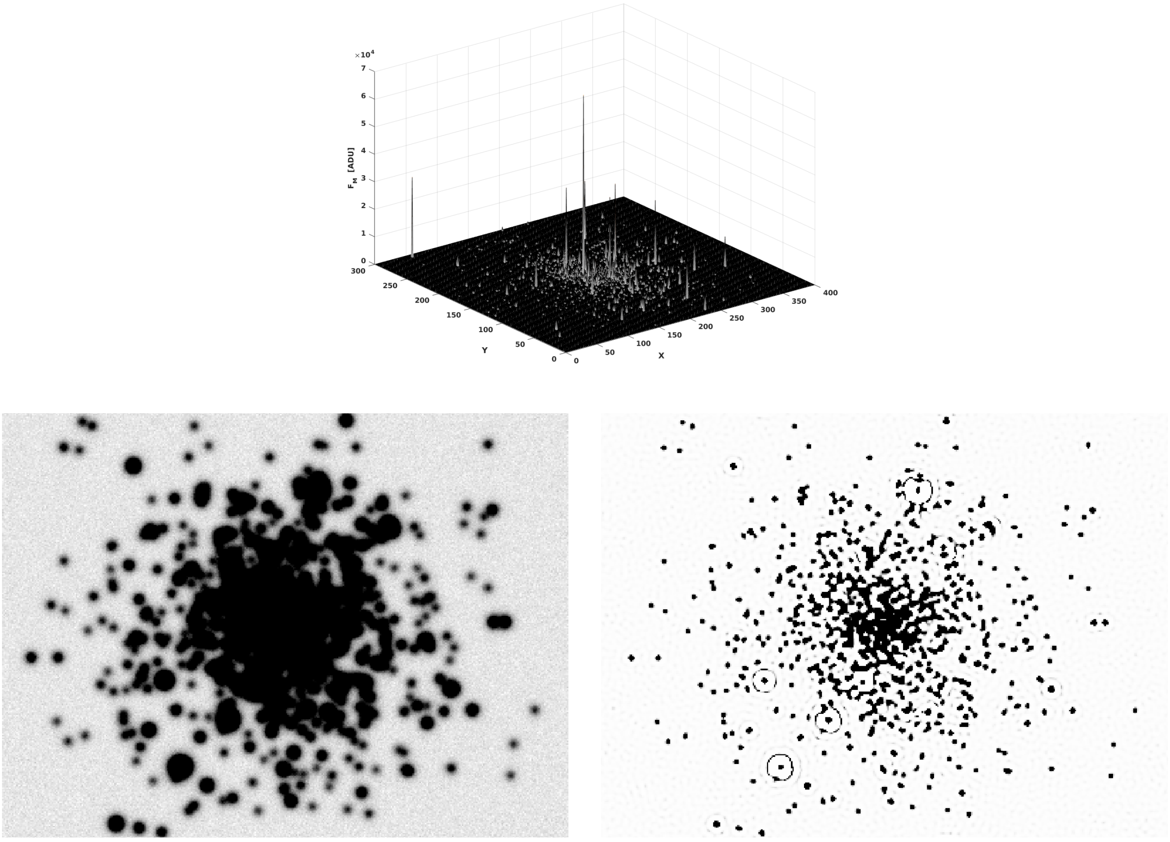

Figure 24: Example from GlencoeSim [12] and deconvolution results - initial point stellar map (top), blurred and noised simulation (bottom left) and simple R-L deconvolution result (bottom right). 1024 stars estimated with potential maximal flux 65536 ADU, Moffat PSF having $\alpha = 6$ and $\beta = 3.5$, King's spatial distribution with parameters $R_C = 100$ and $R_T = 300$. Additive Poisson noise has 1024 ADU mean level (higher SNR than in the figure 23).

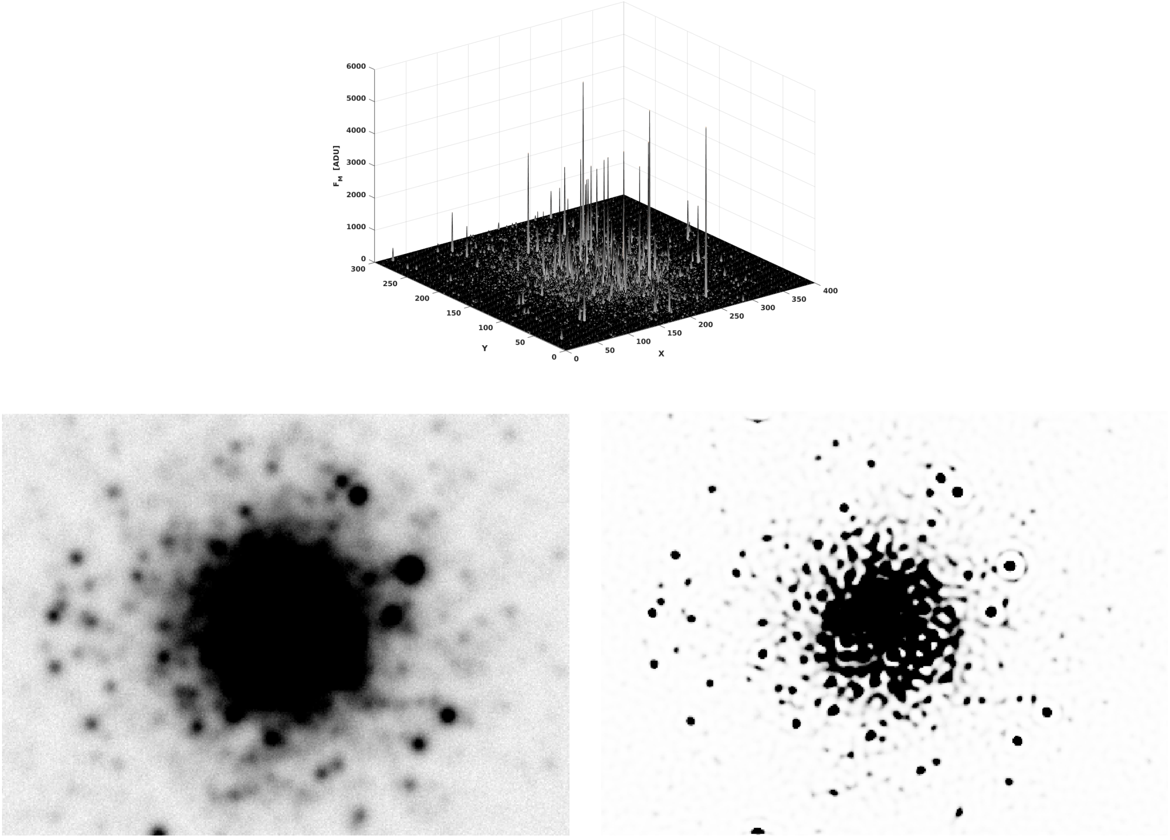

Figure 25: Example from GlencoeSim [12] and deconvolution results - initial point stellar map (top), blurred and noised simulation (bottom left) and simple R-L deconvolution result (bottom right). 16384 stars estimated with potential maximal flux 16384 ADU, Moffat PSF having $\alpha = 8$ and $\beta = 2.5$, King's spatial distribution with parameters $R_C = 50$ and $R_T = 450$. Additive Poisson noise has 4096 ADU mean level.

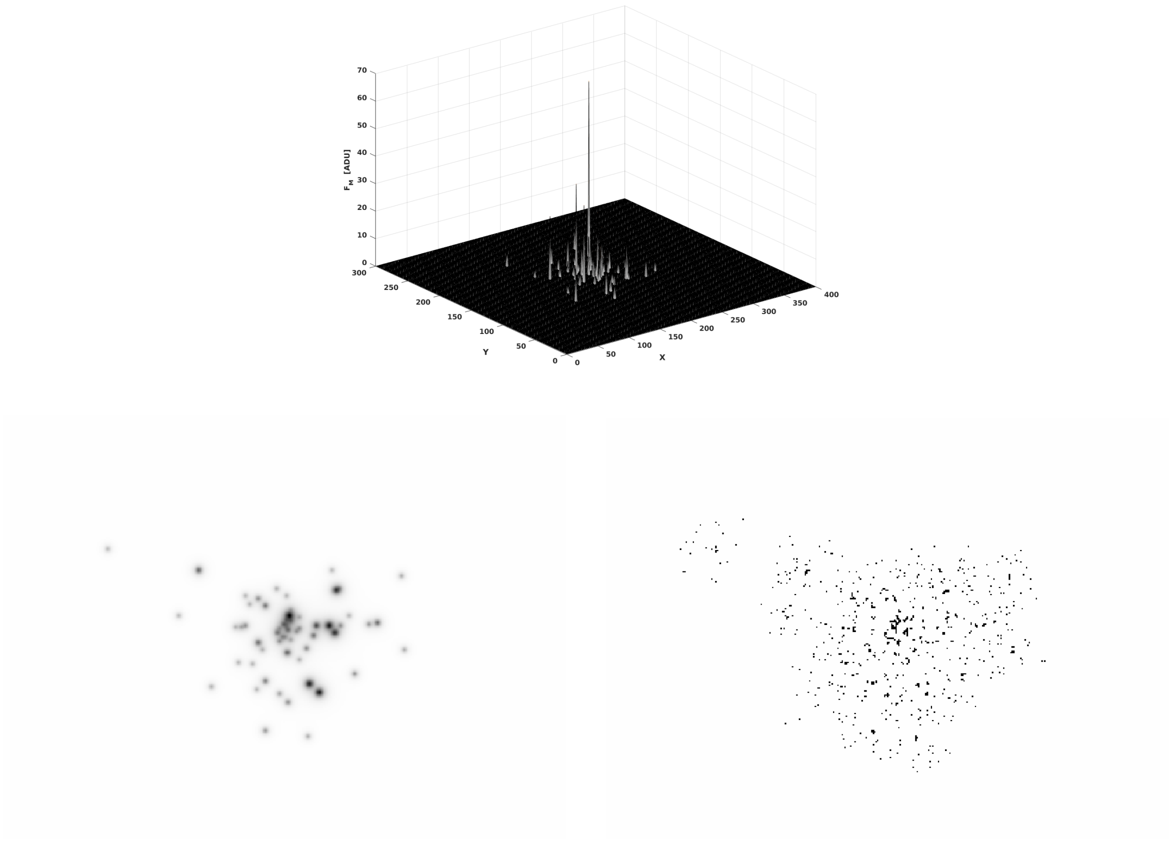

Figure 26: Example from GlencoeSim [12] and deconvolution results - initial point stellar map (top), blurred and noised simulation (bottom left) and simple R-L deconvolution result (bottom right). Only 64 stars estimated with potential maximal flux 64 ADU, compact Moffat PSF having $\alpha = 2$ and $\beta = 1.5$, King's spatial distribution with parameters $R_C = 50$ and $R_T = 150$. This image is blurred only without any additive Poisson noise and any signal modification by non-uniform Poisson noise.

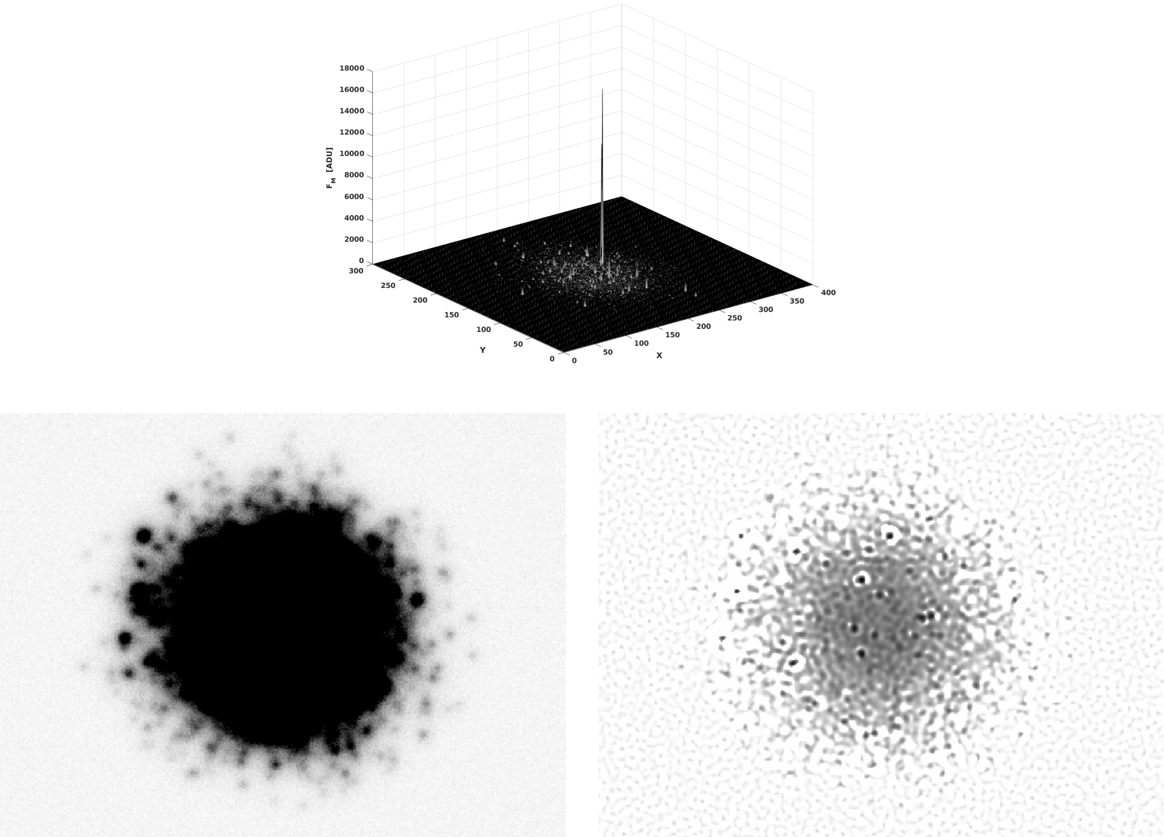

Figure 27: Example from GlencoeSim [12] and deconvolution results - initial point stellar map (top), blurred and noised simulation (bottom left) and simple R-L deconvolution result (bottom right). 16384 stars estimated with potential maximal flux 16384 ADU, Moffat PSF having $\alpha = 4$ and $\beta = 1.5$, King's spatial distribution with parameters $R_C = 50$ and $R_T = 150$ creating extremely dense and compact GCl. Additive Poisson noise has only 16 ADU of the mean level.

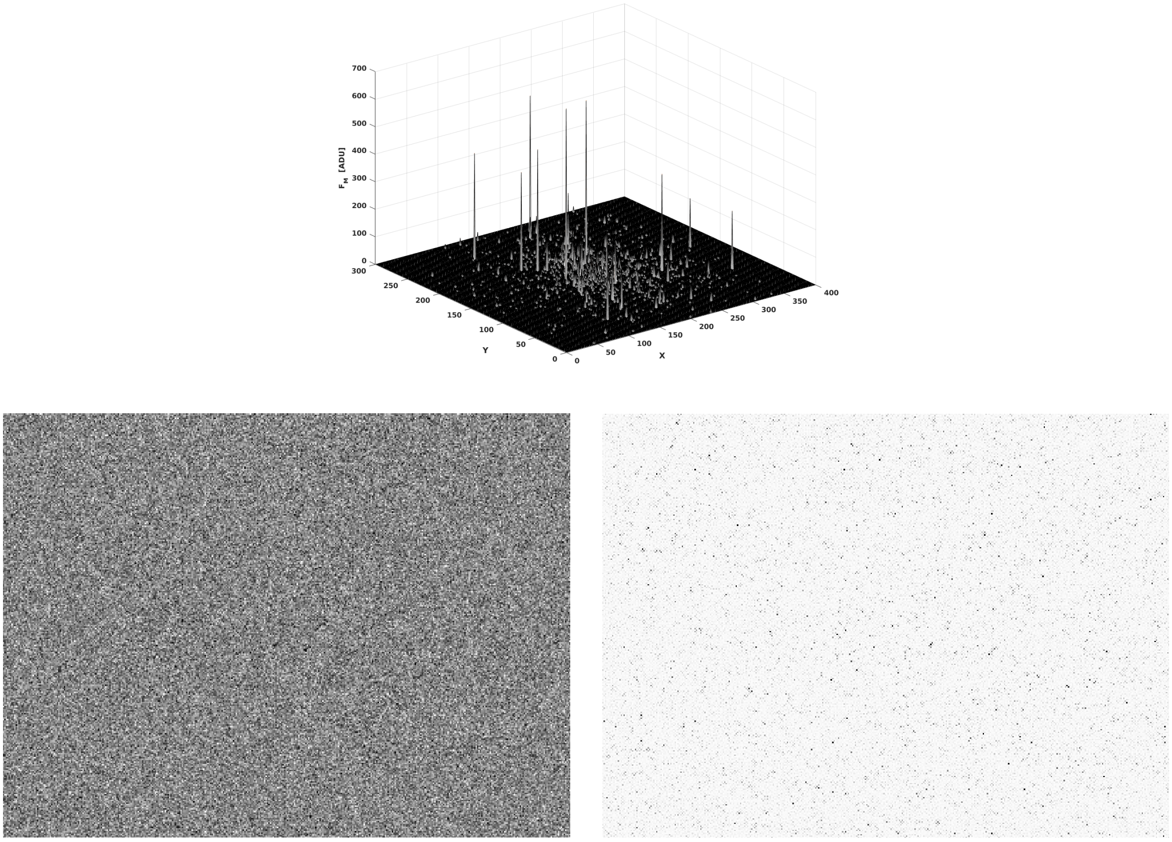

Figure 28: Example from GlencoeSim [12] and deconvolution results - initial point stellar map (top), blurred and noised simulation (bottom left) and simple R-L deconvolution result (bottom right). 1024 stars estimated with potential maximal flux 1024 ADU, Moffat PSF having $\alpha = 2$ and $\beta = 5$, King's spatial distribution with parameters $R_C = 150$ and $R_T = 300$. Additive Poisson noise has 16384 ADU mean level - this image has most of the stars hidden inside the noise standard deviation of 128 ADU (square root of Poisson mean level).

Table 9: List of condition and settings for the simulations and R-L deconvolutions in the figures 23, 24, 25, 26, 27 and 28.

Fig.	Estim. stars	Estim. max flux [ADU]	PSF α	PSF β	R_C	R_T	Additive noise level	Non-uniform Poisson noise
23	1024	65536	6	3.5	100	300	65536	yes
24	1024	65536	6	3.5	100	300	1024	yes
25	16384	16384	8	2.5	50	450	4096	yes
26	64	64	2	1.5	50	150	0	no
27	16384	16384	4	1.5	50	150	16	yes
28	1024	1024	2	5	150	300	16384	yes

monly used only with additional methods - see section 4.4). But for such an extremely large set of data (230 thousands images) it is the most suitable *automatic* detector when properly thresholded and interpreted - the numbers of the found stars or fake discoveries have always to be discussed in terms of SNR conditions. On the other hand we are not interested much in absolute values of N_{OK}, N_{NOT} or N_{OVER}, rather into their tendencies viewed inside some parametric sets so the simple peak detector is valid under following circumstances.

As to minimize the number of events where no potential stars were automatically extracted or where extremely high number of fake discoveries are announced, the following procedure of image histogram fitting was used to estimate the noise level and the threshold. Assuming

1. the noise is following the Poisson distribution in the simulation and
2. **assuming the succesful deconvolution process increases strongly the value differences between the expected stars and the noise** (stars gets higher ADU values with every iteration in places of the highest probability compared to the noise pixels which get lower values)

the threshold can be estimated on the $3-\sigma$ level (99.7 % statistical assurance) from the corresponding simulation image. In that case the histogram of all the pixels in the *simulation* is fitted with the Poisson function gaining the (partly inaccurate - due to stars) estimation of the noise level $\bar{D}$. Then the threshold for the deconvolved images would be

$$THR = 3\sigma = 3\sqrt{\bar{D}}. \tag{38}$$

Two things are important to keep in mind :

- The thresholded pixels on the deconvolved images would be not above $\bar{D} + 3\sqrt{\bar{D}}$ [ADU] level, but they would be just and only above $0 + 3\sqrt{\bar{D}}$ [ADU].
- The second boldfaced assumption may never be guaranteed theoretically in the presence of the noise [7] (or better mathematically there is no guarantee that the convolution kernel of (10) exists). Other image processing methods from various astronomical observations have to be used additionally to prove the results of the deconvolution process when using our assumption!

When the stars are successfully registered for each image (pair simulation and its deconvolution) then the metrics describing such a combination by simple indicators can be calculated from these registered stars and their flux values. This metrics σ_{MET} is defined in previous sections by (37) while using the ratio number R from (34). The table with the "astrometric and photometric" results containing following measurements

- **Total number of stars in the map** N_*
- **Found and registered stars** N_{OK}
- **Missing non-registered stars** N_{NOT}
- **Fake stellar discoveries** N_{OVER}
- **Flux ratio** R from (34)
- **Flux efficiency metrics** σ_{MET} from (37)

has 76800 rows so just the small part for the illustration is shown in the table 10. The rest can be found on the address of MMTG group[15]. First seven columns in the table 10 show the variable parameters of GlencoeSim settings (see table 8). Not noised simulations are marked 'NaN' in the (+) column with estimated mean noise levels. The results are in the columns 'Registered stars' and 'Metrics' as described and discussed above.

8.5 Principal Component Analysis of the efficiency criteria

Principal Component Analysis (PCA) [44] is a statistical tool which looks for relations in different variables in datasets with normal distribution. It looks for correlations between these variables and can suggest lower number of parameters to describe these datasets (in case some of these variables seem to be partly correlated). In generally our two approaches of efficiency tests (astrometric and photometric) are based on diametrically different principles - the first one is indicating the number of positively

---

[15] http://dbq.multimediatech.cz/users/blazek/public/thesis

Table 10: First page out of 1600 pages with the results of simple R-L deconvolution of GlencoeSim simulations. First seven columns refer to the variable GlencoeSim parameters (see table 8) with each line representing one simulation image. Following four columns show the 'astrometric' results after R-L deconvolution as defined in the section 8.2 and last two columns show the results of the deconvolution efficiency as declared by (34, 37). The column marked **(+)** contains the noise levels (see table 7), while the not-noised images with no non-uniform Poisson signal modification is marked by 'NaN'. The whole table can be downloaded from dbq.multimediatech.cz/users/blazek/public/thesis.

GlencoeSim parameters							Stellar registration				Metrics	
PSF		MAX	MAX	R_C	R_T	(+)	N_*	N_{OK}	N_{NOT}	N_{OVER}	R	σ_{MET}
α	β	STAR	FLUX			[ADU]						[ADU]
2	1.5	64	64	50	150	0	62	62	0	4	0.61173	6.503
2	1.5	64	64	50	150	4	62	31	31	0	0.53733	14.703
2	1.5	64	64	50	150	16	62	14	48	23	0.39105	37.743
2	1.5	64	64	50	150	64	62	12	50	307	0.41582	47.658
2	1.5	64	64	50	150	256	62	15	47	1210	0.93071	49.872
2	1.5	64	64	50	150	1024	62	29	33	5176	3.7773	21.7
2	1.5	64	64	50	150	4096	62	44	18	11511	13.731	15.096
2	1.5	64	64	50	150	16384	62	51	11	11453	56.276	11.808
2	1.5	64	64	50	150	65536	62	51	11	11433	189.61	13.902
2	1.5	64	64	50	150	NaN	62	62	0	4	0.61173	6.503
2	1.5	64	64	50	300	0	61	60	1	10	0.61258	8.0213
2	1.5	64	64	50	300	4	61	47	14	1	0.61375	9.9256
2	1.5	64	64	50	300	16	61	25	36	23	0.44029	25.431
2	1.5	64	64	50	300	64	61	16	45	295	0.37284	52.482
2	1.5	64	64	50	300	256	61	12	49	1218	0.62688	74.948
2	1.5	64	64	50	300	1024	61	25	36	5165	2.6582	30.266
2	1.5	64	64	50	300	4096	61	52	9	11502	13.848	12.544
2	1.5	64	64	50	300	16384	61	46	15	11458	38.046	13.851
2	1.5	64	64	50	300	65536	61	48	13	11435	142.6	13.956
2	1.5	64	64	50	300	NaN	61	60	1	10	0.61258	8.0213
2	1.5	64	64	50	450	0	60	53	7	9	0.61853	3.9749
2	1.5	64	64	50	450	4	60	10	50	1	0.42347	27.532
2	1.5	64	64	50	450	16	60	4	56	22	0.33791	81.262
2	1.5	64	64	50	450	64	60	3	57	304	0.29881	110.92
2	1.5	64	64	50	450	256	60	6	54	1218	1.1082	48.845
2	1.5	64	64	50	450	1024	60	23	37	5176	7.7503	15.917
2	1.5	64	64	50	450	4096	60	40	20	11511	32.62	10.709
2	1.5	64	64	50	450	16384	60	42	18	11464	106.91	5.3507
2	1.5	64	64	50	450	65536	60	47	13	11436	436.23	5.1807
2	1.5	64	64	50	450	NaN	60	53	7	9	0.61853	3.9749
2	1.5	64	64	50	600	0	58	46	12	8	0.63954	4.2019
2	1.5	64	64	50	600	4	58	8	50	1	0.40179	19.237
2	1.5	64	64	50	600	16	58	3	55	23	0.25332	65.7
2	1.5	64	64	50	600	64	58	6	52	298	0.72893	32.138
2	1.5	64	64	50	600	256	58	9	49	1213	1.8417	27.962
2	1.5	64	64	50	600	1024	58	31	27	5169	11.963	12.585
2	1.5	64	64	50	600	4096	58	42	16	11513	40.279	10.548
2	1.5	64	64	50	600	16384	58	43	15	11461	143.9	10.565
2	1.5	64	64	50	600	65536	58	45	13	11437	522.58	10.368
2	1.5	64	64	50	600	NaN	58	46	12	8	0.63954	4.2019
2	1.5	64	64	100	150	0	63	52	11	7	0.61708	4.5449
2	1.5	64	64	100	150	4	63	5	58	0	0.25228	49.836
2	1.5	64	64	100	150	16	63	3	60	23	0.20994	72.676
2	1.5	64	64	100	150	64	63	2	61	305	0.24228	147.79
2	1.5	64	64	100	150	256	63	8	55	1218	1.6675	31.242
2	1.5	64	64	100	150	1024	63	31	32	5168	12.28	12.277
2	1.5	64	64	100	150	4096	63	54	9	11503	53.138	9.5027
2	1.5	64	64	100	150	16384	63	48	15	11456	150.02	9.5859
2	1.5	64	64	100	150	65536	63	43	20	11441	463.56	10.418
2	1.5	64	64	100	150	NaN	63	52	11	7	0.61708	4.5449
2	1.5	64	64	100	300	0	62	61	1	6	0.60694	6.9997
...	...	...	...	...	...	...	...	...	...	...	...	...
...	...	...	...	...	...	...	...	...	...	...	...	...
...	...	...	...	...	...	...	...	...	...	...	...	...
...	...	...	...	...	...	...	...	...	...	...	...	...
...	...	...	...	...	...	...	...	...	...	...	...	...

registered stars N_{OK} (or fake stars N_{OVER}) and the second one is calculating the photometric flux metrics σ_{MET} from the (37) - one scalar number for all the stars in one image.

This section deals with the datamining from the table 10 (which has 76800 rows, each row containing results for one simulated image) using PCA analysis.

As the input for the PCA analysis have been chosen 3 dependent variables from the table 10 :

$$\frac{N_{OK}}{N_*}, \frac{N_{OVER}}{N_*} \text{ and } \frac{\sigma_{MET}}{\text{MAXFLUX}}.$$

The PCA analysis shows following distribution of the main components in term of their strength on variance :

Component X1 :	99.98928 %
Component X2 :	0.01072 %
Component X3 :	0.000000009 %

The components weights plot can be seen in the figure 29. These results suggest some statistical correlation between our three different metrics (two astrometric and one photometric here chosen for PCA). And indeed one good connection exists! With the help of PCA after deep datamining the connection between photometric metrics σ_{MET} and the number of well registered stars N_{OK} was found. The figure 30 shows the dataset results for the number initial stars in the simulations set at 65536 stars (similar graphs with different magnitudes occur for the other initial stellar numbers). Each point of the graph represents one simulation (containing 65536 initial stars $\sim N_*$). For x axis there is the ratio of the number of well registered stars $\frac{N_{OK}}{N_*}$ and for the y axis there is the ratio in log scale of (37) metrics weighed over maximal flux set for all stars in appropriate simulation. **This graph shows strong evidence of power-law dependence, which confirms our good choice of efficiency criteria N_{OK} and σ_{MET} even though they are based on completely different principles!** According to the expected

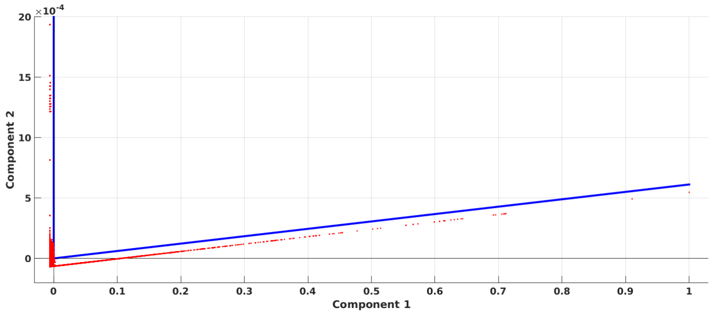

Figure 29: PCA component weights plot for the astrometric and photometric simulation results from the table 10.

'goodness' of these criteria the more stars are well registered at the simulations (right part of graph) the more precise (and lower) the metrics σ_{MET} should be (bottom part of the graph).

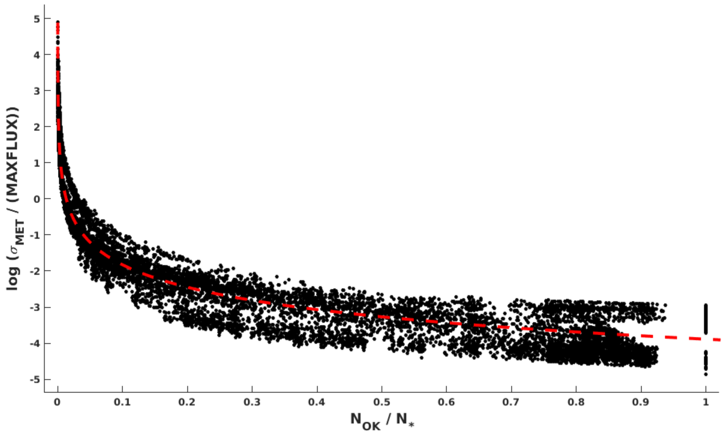

Figure 30: The power-law relation between two by principle different criteria - N_{OK} and σ_{MET} from (37). Even though these two efficiency criteria are given by way different principles (see section 8.2) they correspond together in the term of describing the *goodness* of the deconvolution tests. Each point at this graph represent one simulation containing 65536 initial stars (similar graphs occur for the other initial numbers). The relation on this graph was found due to the PCA analysis of the table 10.

9 Analysis of R-L deconvolution of simulations

The influence of the input parameters (from GlencoeSim, see table 8) on the efficiency of the simple R-L deconvolution [57, 54] (under assumptions and conditions discussed in the previous section 8.3) is presented and discussed. Following results and figures are trying to find the influence of many initial conditions on the final deconvolution success. All the figures are plotted from the data from the simulations and deconvolutions as described in the section 8. Small sample of the data is shown in the table 10 (the rest can be found on the address http://dbq.multimediatech.cz/users/blazek/public/thesis).

9.1 Influence of spatial distribution

In this section we investigate how the efficiency of deconvolution depends on spatial distribution of globular cluster. In figures 31, 32, 33 and 34 there are four efficiency parameters (σ_{MET}, N_{OK}/N_*, N_{NOT}/N_*, N_{OVER}/N_*) in dependence on GCl spatial distribution parameters R_C, R_T and on the number of estimated stars in GCl.

From the figure 31 it is evident that the efficiency of positive stellar discoveries declines with the number of stars, which is logical and expected (the denser the GCl is, the harder it is to distinguish stars from each other). In the diagrams the dense GCl ($R_C = 50$ and $R_T = 150$) represents bottom left corner while sparse GCL ($R_C = 150$ and $R_T = 600$) is pointed in upper right corner of each diagram. One could expect the higher efficiency of astrometric accuracy after deconvolution of more sparse GCl, but the figure 31 does not show any strong evidence for such a hypothesis (only weak tendention in the case of 1024 stars towards higher R_T). The same happens for two other astrometric results in figures 32 and 32 - **no reliable evidence of astrometric efficiency dependence on GCl spatial distribution.**

Different situation is in the case of the 'photometric efficiency' in figure 34. Darker values towards right upper corners of diagrams in the case of 64 and 1024 stars are fulfilling the expectations that sparse GCl would get better deconvolution results - in this case **the σ_{MET} metrics from (37) reveals statistically the more accurate estimation of the original stellar fluxes in the case of sparse GCl** (with higher both R_C and R_T). However this tendency is fainter towards higher total number of stars in the cluster. The differences of σ_{MET} are negligible in the case of 16384 stars and no general tendency can by found in the case of 65536 stars - in this case probably such a huge number of stars is the reason itself for lower efficiency compared to the influence of spatial distributional parameters.

64 stars 1024 stars

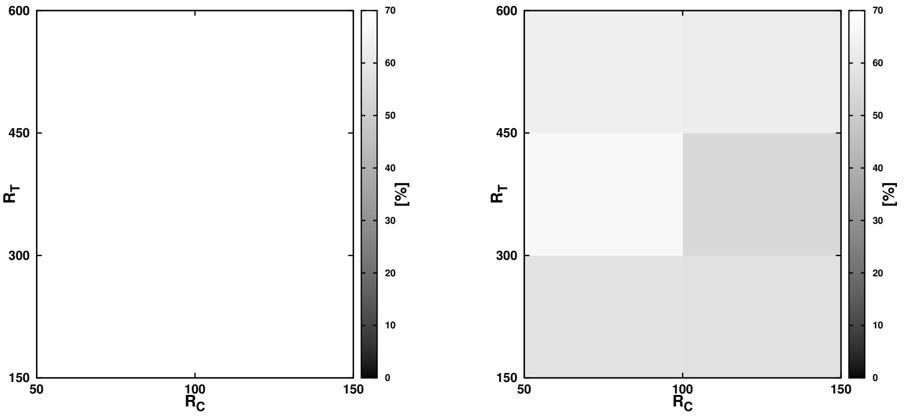

16384 stars 65536 stars

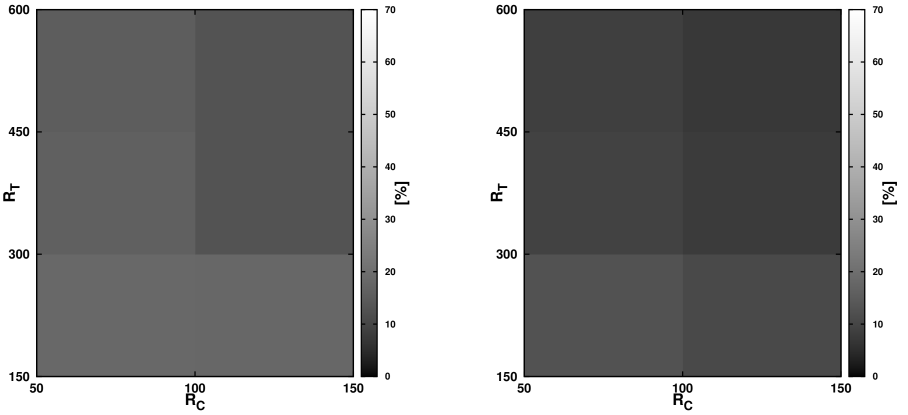

Figure 31: Dependence of the stars found after deconvolution (ratio N_{OK} / N_*) on number of initial stars and spatial distribution parameters R_C, R_T.

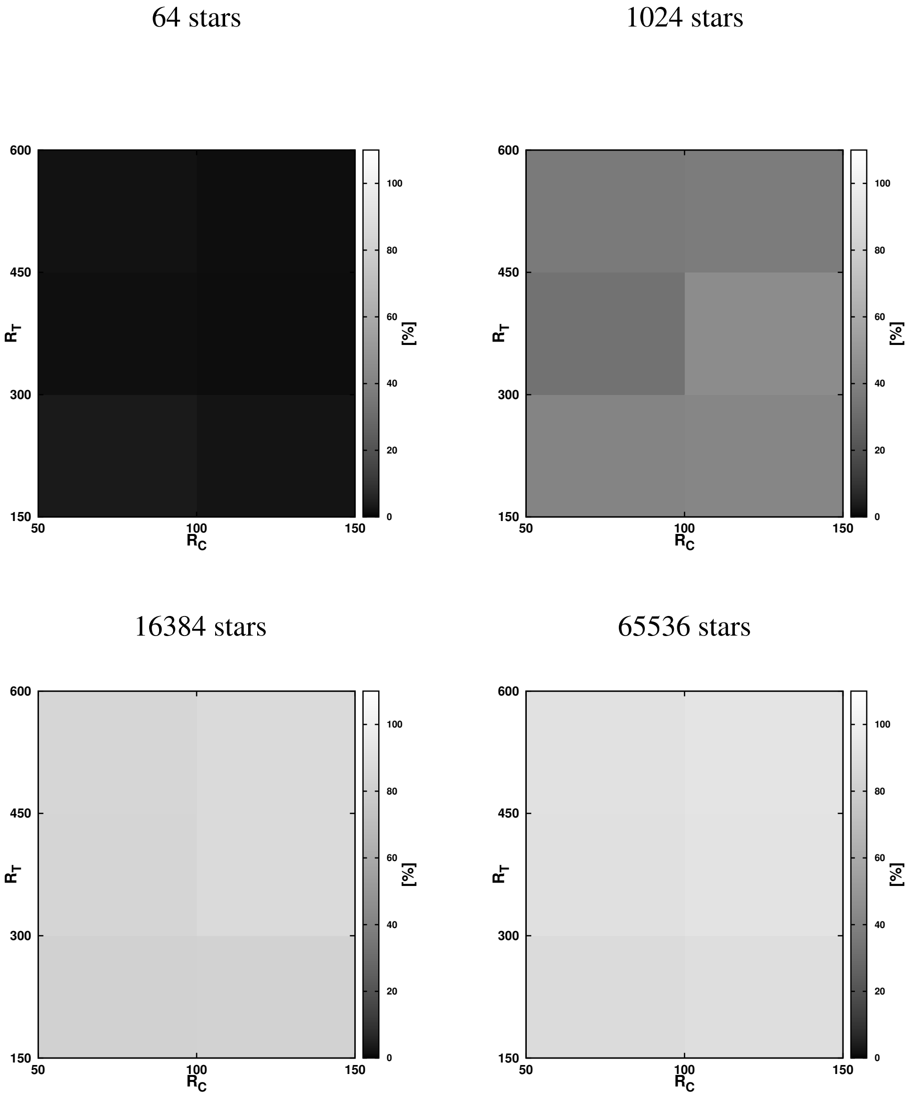
64 stars

1024 stars

16384 stars

65536 stars

Figure 32: Dependence of the non registered stars after deconvolution (ratio N_{NOT} / N_*) on number of initial stars and spatial distribution parameters R_C, R_T.

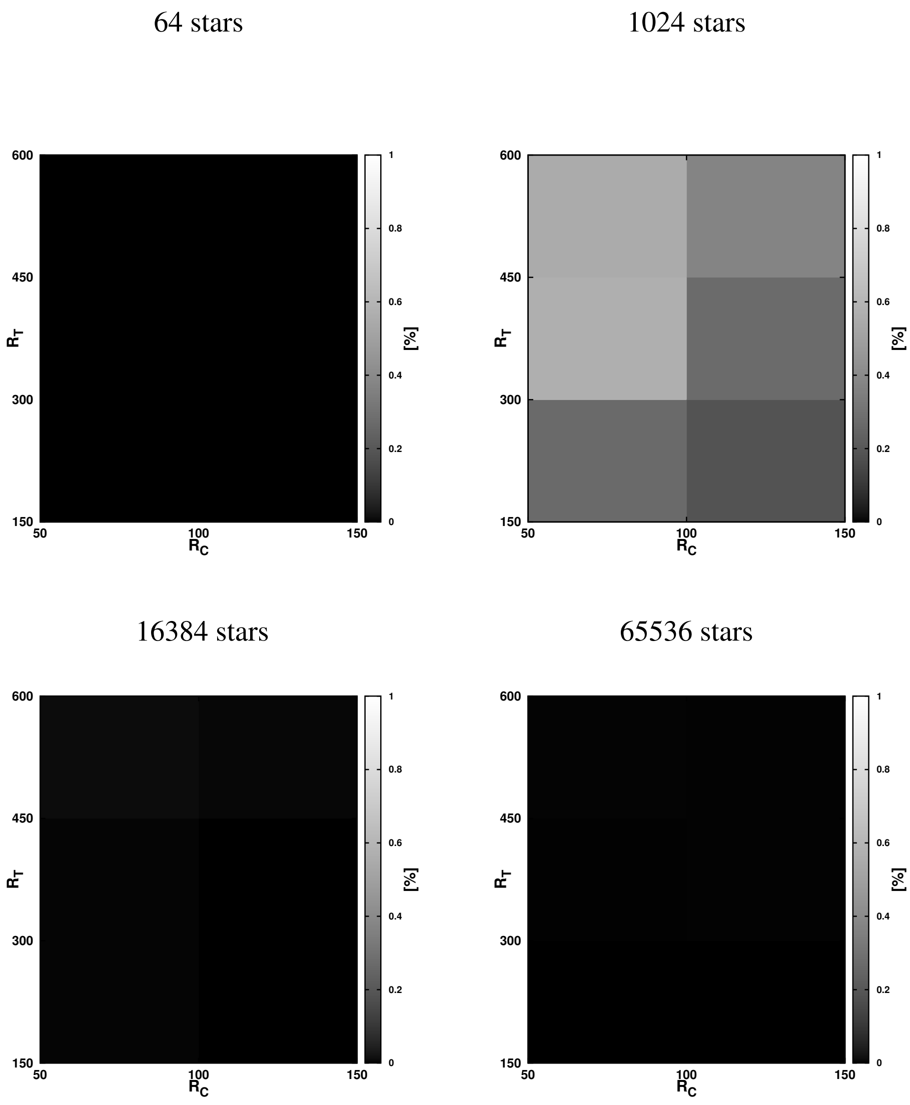

Figure 33: Dependence of the fake discoveries (ratio N_{OVER} / N_*) on number of initial stars and spatial distribution parameters R_C, R_T.

64 stars 1024 stars

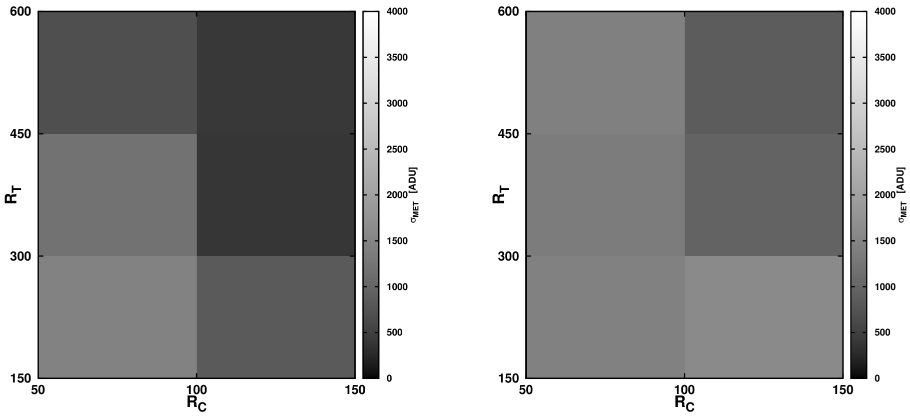

16384 stars 65536 stars

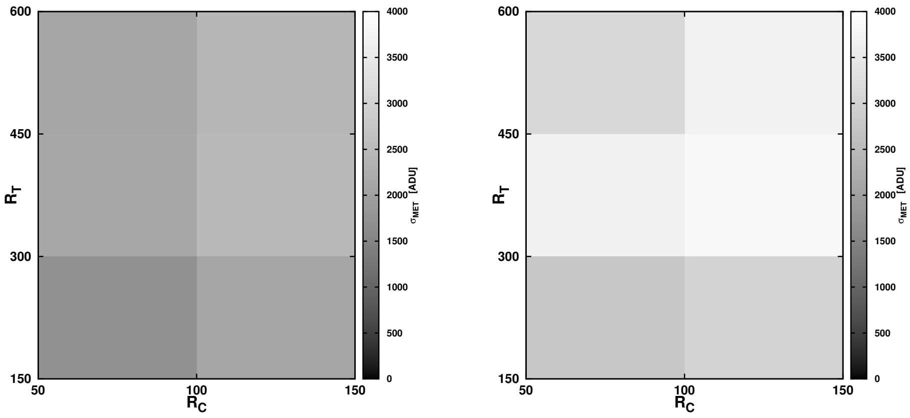

Figure 34: Dependence of σ_{MET} from (37) on number of initial stars and spatial distribution parameters R_C, R_T.

9.2 Influence of noise

Similar analysis (positioning and flux estimation accuracy) can be done regarding the noise level of the background and the signal. Following figures 35, 36, 37, 38, 39, 40, 41 and 42 are grouped into 12 graphs for each of four regarded result parameters

$$\sigma_{MET}, \frac{N_{OK}}{N_*}, \frac{N_{NOT}}{N_*}, \frac{N_{OVER}}{N_*}. \tag{39}$$

Each of the 12 graphs is plotted for one combination of spatial distribution parameters R_C-R_T. Inside each graph there are four lines of data results belonging to 64, 1024, 16384 and 65536 estimated initial stars in the initial map in dependence on the noise level. Ten noise levels are described in the table 7 - logarithmic scale shows the mean level of additive noise from GlencoeSim simulator, *POISSON ONLY* value contains the simulation without additive noise yet with non-uniform Poisson signal modification and *NO NOISE* describes the case with no noise modification at all. All graphs and data were taken from the table 10. For visualizations of multidimensional datasets the following parameters were set fixed in this section - PSF shape $\alpha = 4$, $\beta = 2$ and **maximal flux of the initial stars in the map set to 16384** (to test the behaviour in the case of signal being lower than the noise).

9.2.1 Stellar positions accuracy

'Astrometric efficiency' (number of stars registered well between the deconvolution result and the initial map) can be seen in figures 35 and 36. As expected always the highest percentage of the ratio $\frac{N_{OK}}{N_*}$ gets the red case of 64 estimated initial stars (often close to 100 % efficiency) with green line (1024 stars) having lower efficiency between 50-80 % for no noise level. Last two lines (pink and purple) for 16384 and 65536 estimated initial stars rarely exceed 20 % of the efficiently found and registered stars. The other expected tendency is the lower efficiency of the ratio with well registered stars with higher noise level (except the last two points of each line - as discussed later in this section).

As the total number of initial mapped stars N_* is equal to

$$N_* = N_{OK} + N_{NOT} \tag{40}$$

then the figures 37 and 38 showing the ratio $\frac{N_{NOT}}{N_*}$ are actually the complementary graphs to previously discussed figures 35 and 36 with $\frac{N_{OK}}{N_*}$ ratio information. It is important to keep in mind that the total number of initial mapped stars N_* is not exactly equal to the GlencoeSim parameter of the number of estimated initial stars! It often can be the same, but due to the random process of creating of simulations and sometimes wider spatial distribution than the size of the test images, it is not always the same and may vary a bit!

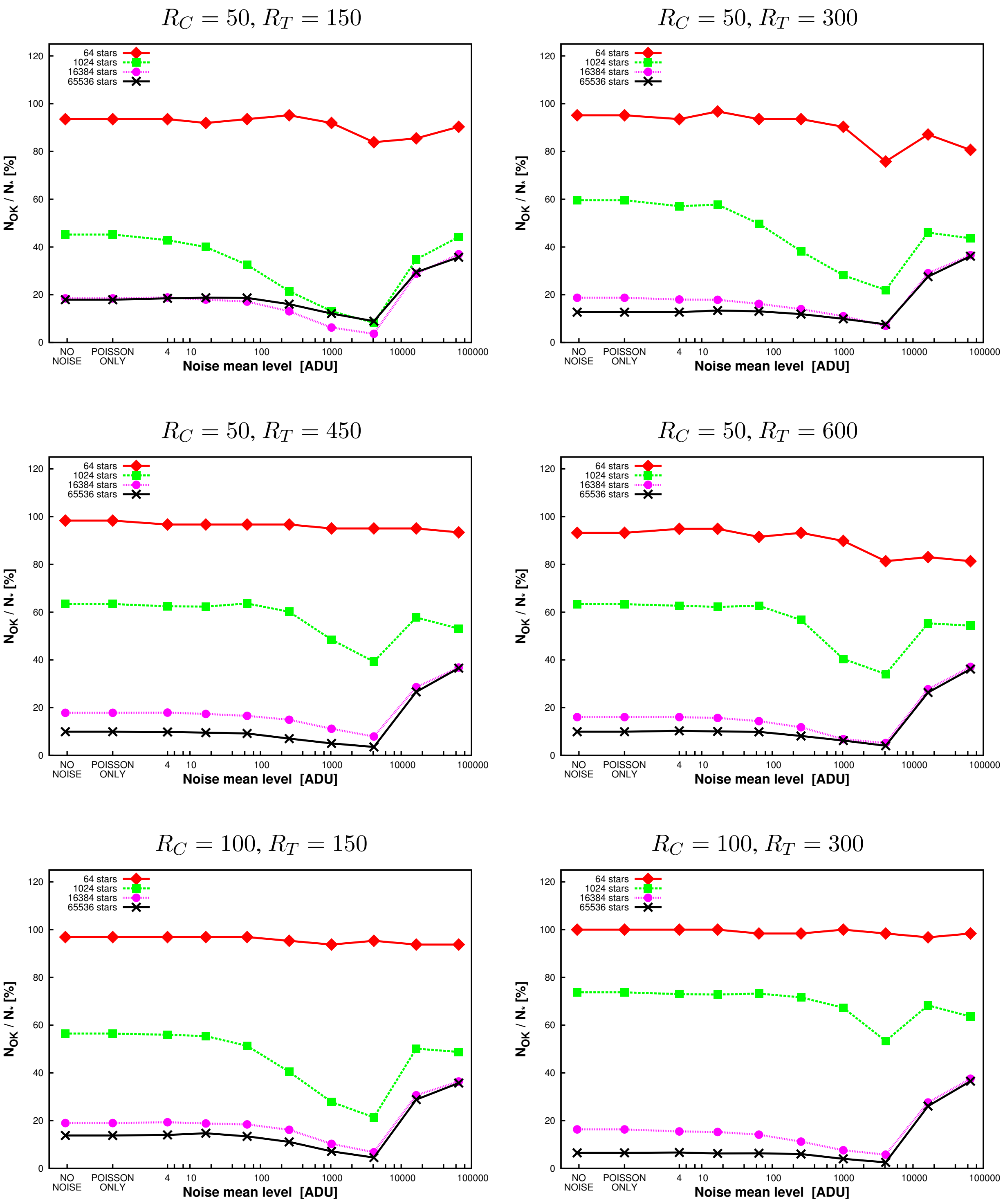

$R_C = 50$, $R_T = 150$

$R_C = 50$, $R_T = 300$

$R_C = 50$, $R_T = 450$

$R_C = 50$, $R_T = 600$

$R_C = 100$, $R_T = 150$

$R_C = 100$, $R_T = 300$

Figure 35: Evolution of the number of the found stars (ratio N_{OK} / N_*) on the noise level for various spatial distribution parameters (part **A**). *Poisson only* - no additive noise, only non-uniform Poisson signal modification. *No noise* - no noise modification at all.

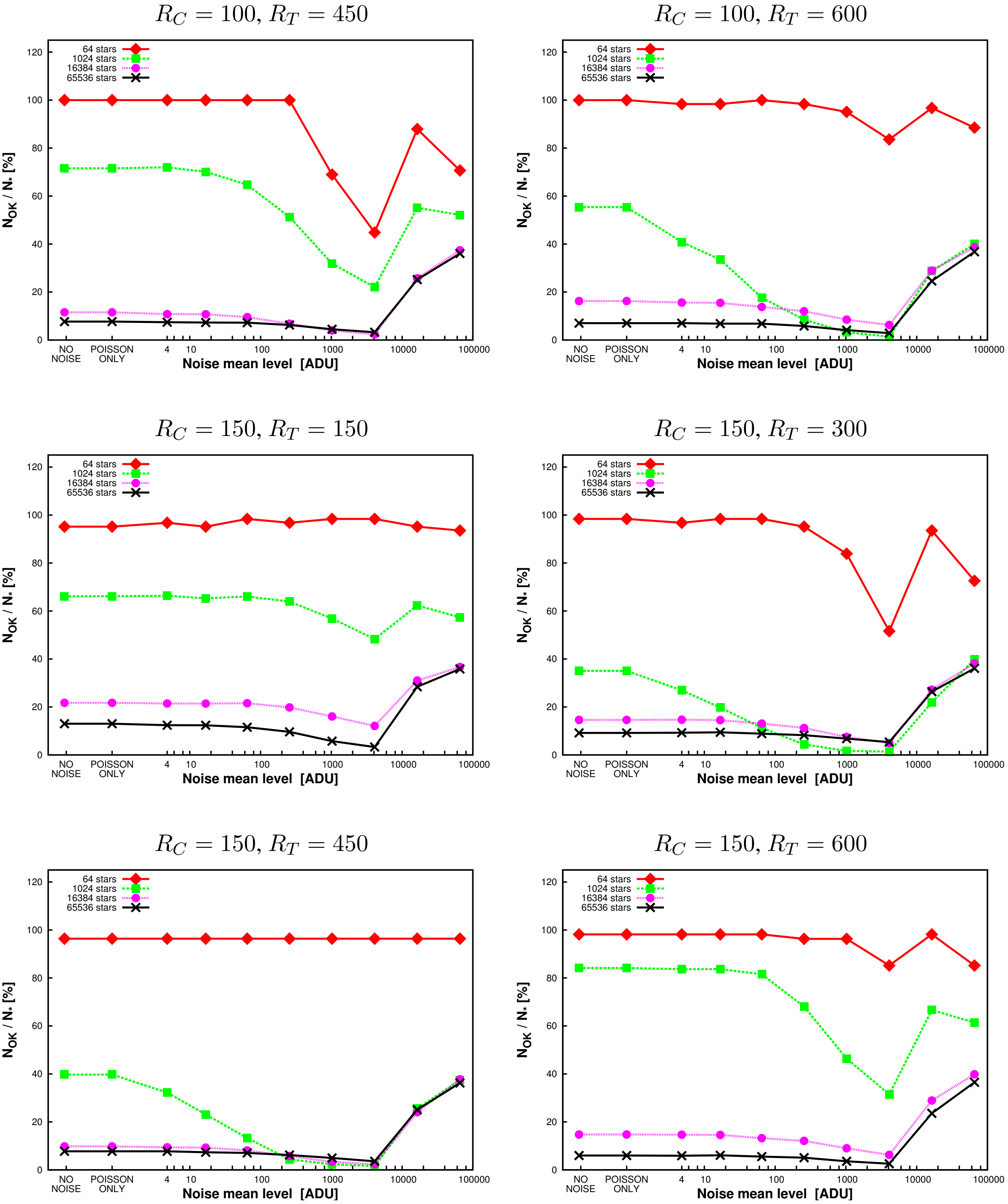

$R_C = 100, R_T = 450$

$R_C = 100, R_T = 600$

$R_C = 150, R_T = 150$

$R_C = 150, R_T = 300$

$R_C = 150, R_T = 450$

$R_C = 150, R_T = 600$

Figure 36: Evolution of the number of the found stars (ratio N_{OK} / N_*) on the noise level for various spatial distribution parameters (part **B**). *Poisson only* - no additive noise, only non-uniform Poisson signal modification. *No noise* - no noise modification at all.

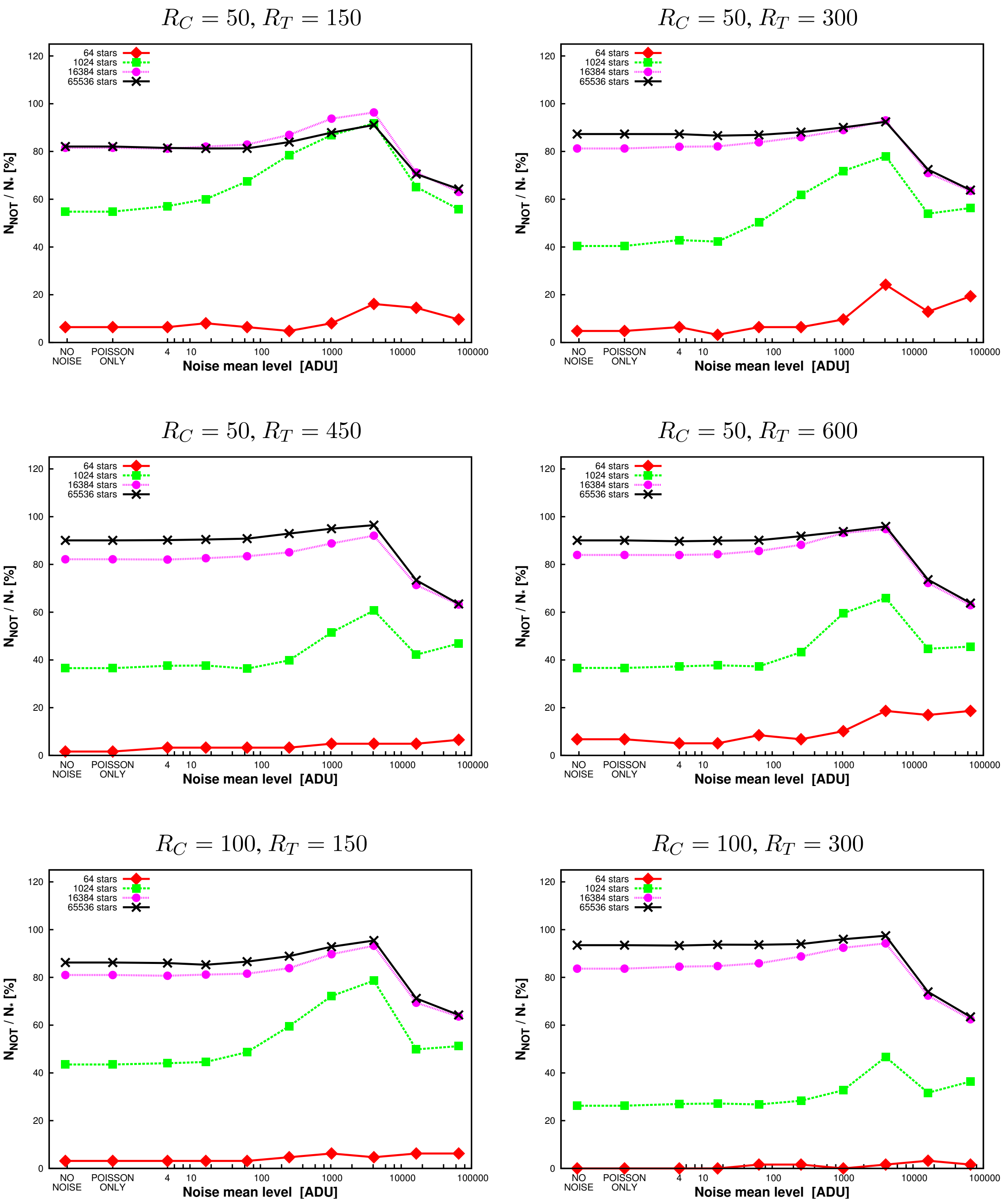

$R_C = 50$, $R_T = 150$

$R_C = 50$, $R_T = 300$

$R_C = 50$, $R_T = 450$

$R_C = 50$, $R_T = 600$

$R_C = 100$, $R_T = 150$

$R_C = 100$, $R_T = 300$

Figure 37: Evolution of the number of faint non-registered stars (ratio N_{NOT} / N_*) on the noise level for various spatial distribution parameters (part **A**). *Poisson only* - no additive noise, only non-uniform Poisson signal modification. *No noise* - no noise modification at all.

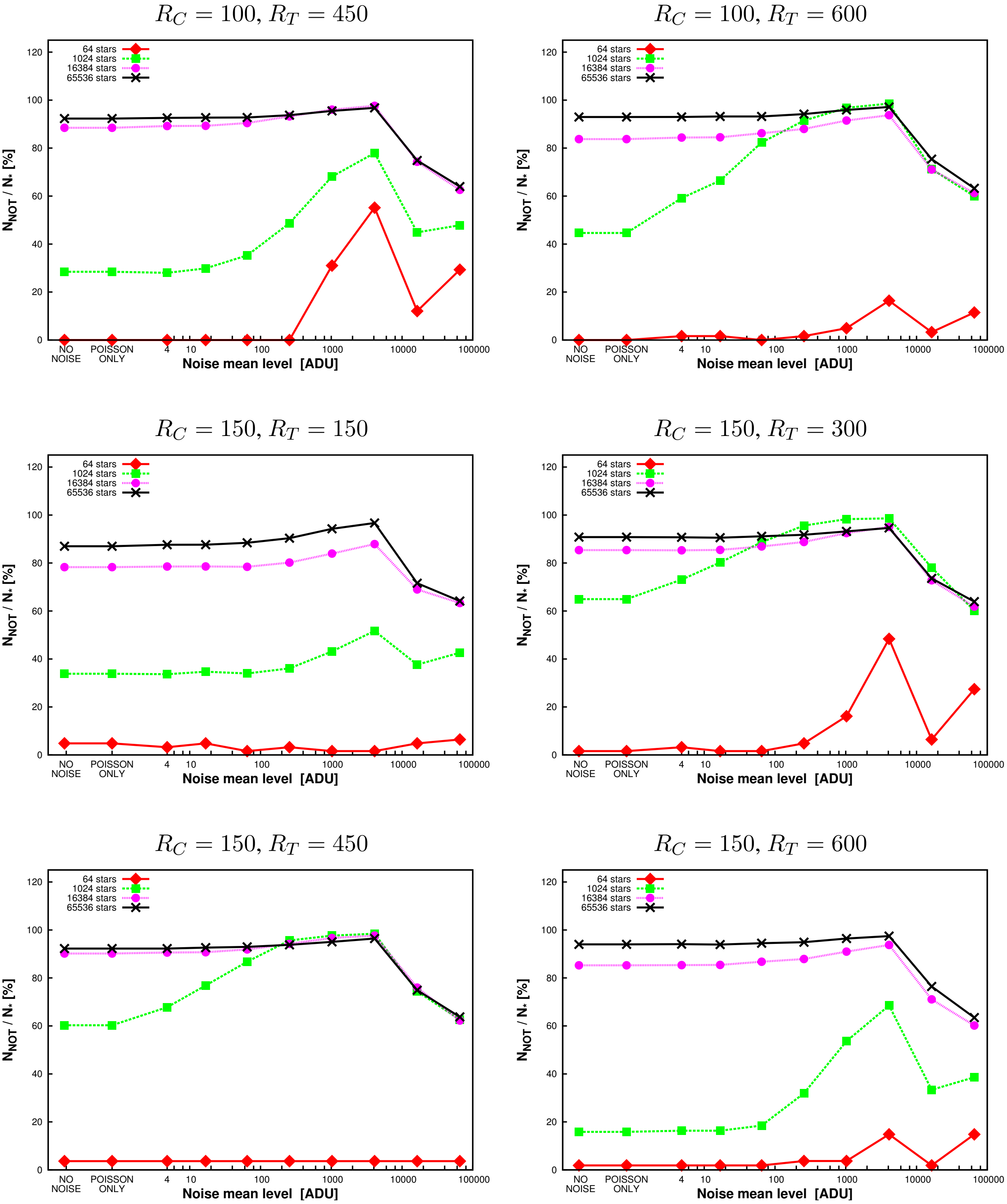

Figure 38: Evolution of the number of faint non-registered stars (ratio N_{NOT} / N_*) on the noise level for various spatial distribution parameters (part **B**). *Poisson only* - no additive noise, only non-uniform Poisson signal modification. *No noise* - no noise modification at all.

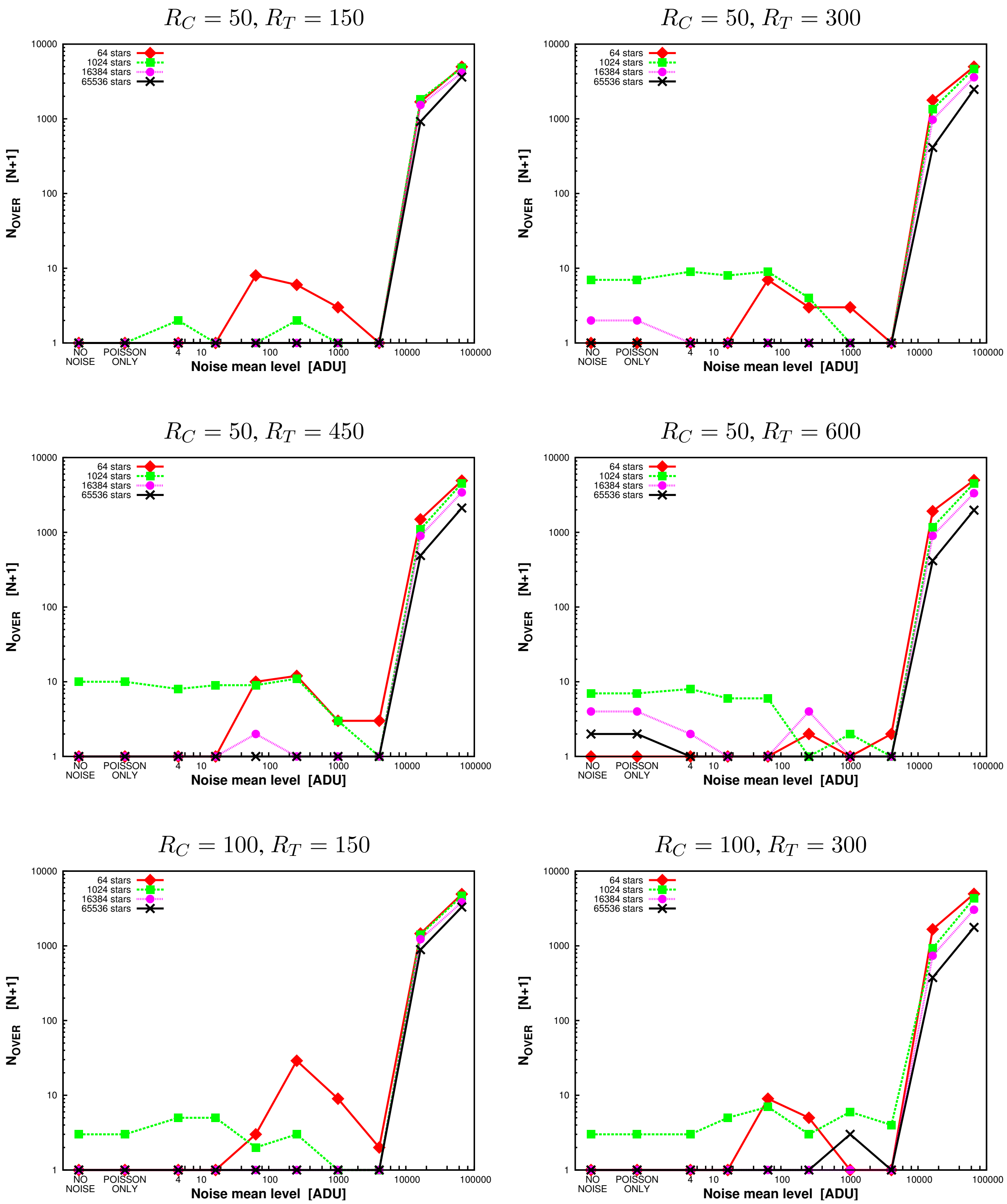

Figure 39: Evolution of the number of the fake stars (ratio N_{OVER} / N_*) after deconvolution on the noise level for various spatial distribution parameters (part **A**). *Poisson only* - no additive noise, only non-uniform Poisson signal modification. *No noise* - no noise modification at all.

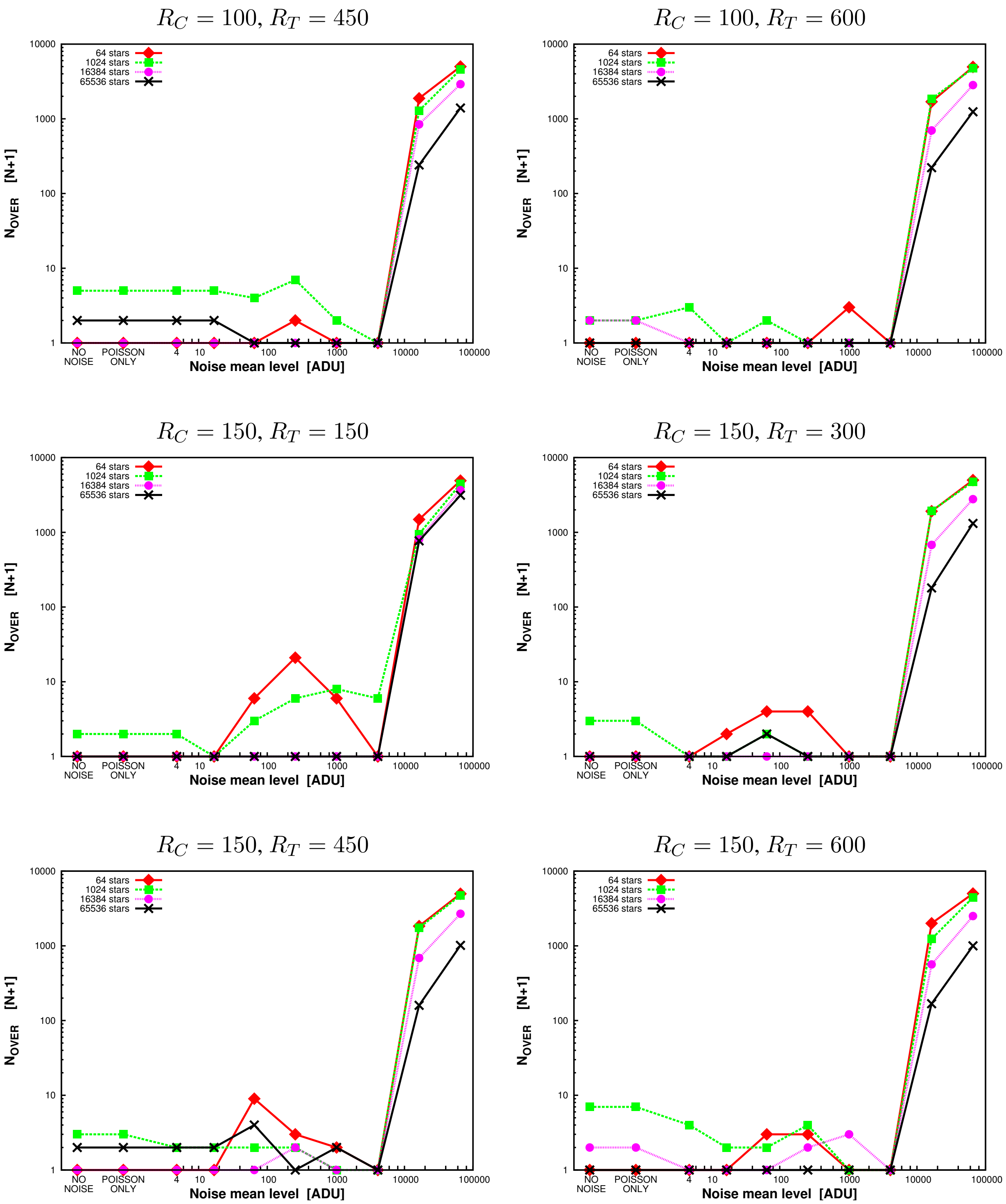

Figure 40: Evolution of the number of the fake stars (ratio N_{OVER} / N_*) after deconvolution on the noise level for various spatial distribution parameters (part **B**). *Poisson only* - no additive noise, only non-uniform Poisson signal modification. *No noise* - no noise modification at all.

9.2.2 Fake discoveries with dependence on SNR level

The last two points of nearly all mentioned graphs in figures 35, 36, 37 and 38 behave ”queer”. For instance the efficiency ratio $\frac{N_{OK}}{N_*}$ for 65536 stars ”magically jumps” up for two cases of extremely high noise level (additive Poisson noise 16384 and 65536 ADU). **In these cases the SNR ratio is statistically always below 1** as the maximal estimated signal flux of initial stars is 16384 ADU in the datasets in this chapter! This information is well seen in figures 39 and 40, where the parameter $\frac{N_{OVER}}{N_*}$ is plotted. In these figures the numbers of fake discoveries after the deconvolution can be seen. As the exact number depends on the methodics used for registration (as discussed in the section 8.2), the general tendency does not - and all the logarithmic graphs in figures 39 and 40 show only several (max 10) fake stars after deconvolution for all noise levels up to 4096 ADU, but extreme growth afterwards up to thousands and 10 thousands of fake discoveries for 16384 and 65536 ADU noise levels! This is the reason why the last two points in all graphs in figures 35, 36, 37 and 38 are not valid registration information. This explanation fits well with our thresholding calculated from the background noise. Actually this situation is not surprising when we look at such a case in the example figure 28, where the simulation, the initial map and the deconvolution result is shown. No surprise the deconvolution fails even for 64 stars only.

9.2.3 Flux efficiency

The efficiency of the deconvolution marked by the metrics σ_{MET} from (37) can be seen in figures 41 and 42. As discussed in the section 9.2.2 the last two points do not represent ”good values” but just fake stellar discoveries due to the noise level (min. 16384 ADU) being significantly higher than the signal level (max. 16384 ADU).

The lowest metrics represents good coincidence between the deconvolution result and the initial stellar map fluxes. It is important to keep in mind that the ”absolute” value of this metrics (37) is not absolute and for instance it does not imply that non-zero σ_{MET} means bad quality of flux estimation after deconvolution. On the other hand the higher σ_{MET} calculated the same way (R-L, same number of iterations, ...) under some circumstances (e.g., high noise) compared to other σ_{MET} under different circumstances (e.g., lower noise) gives the information about statistically better coincidence in the stellar flux estimations.

As expected in general the lowest σ_{MET} has the red line with 64 estimated initial stars and the higher the number of the stars the higher the σ_{MET} metrics. And as expected the higher the mean noise level the higher metrics σ_{MET}. Usually the metrics starts growing significantly around the noise level of 256-1024 ADU. Interesting correlation shows the graphs with lowest $R_T = 150$, where the σ_{MET} with low noise does not depend on the number of stars. Interesting thing is the generaly lower and stably growing line profiles of lowest R_C, R_T compared to their higher values. While for lower noise the line profiles are generally more predictable, for higher noise they become more random when regarded on all 12 R_C-R_T combinations.

The σ_{MET} is actually close to sort of statistical photometric error by its meaning, the interesting thing is that even for high noise values the metrics does not grow quadratically or exponentially, but just roughly linearly with the quadratic growth of total number of stars (64-1024-16384-65536). This is probably caused by the 2-D surface shape of the ”image” itself with the flux values being its simple 3rd dimension where the concentration of the stars statistically growth with just the square root of the number of stars.

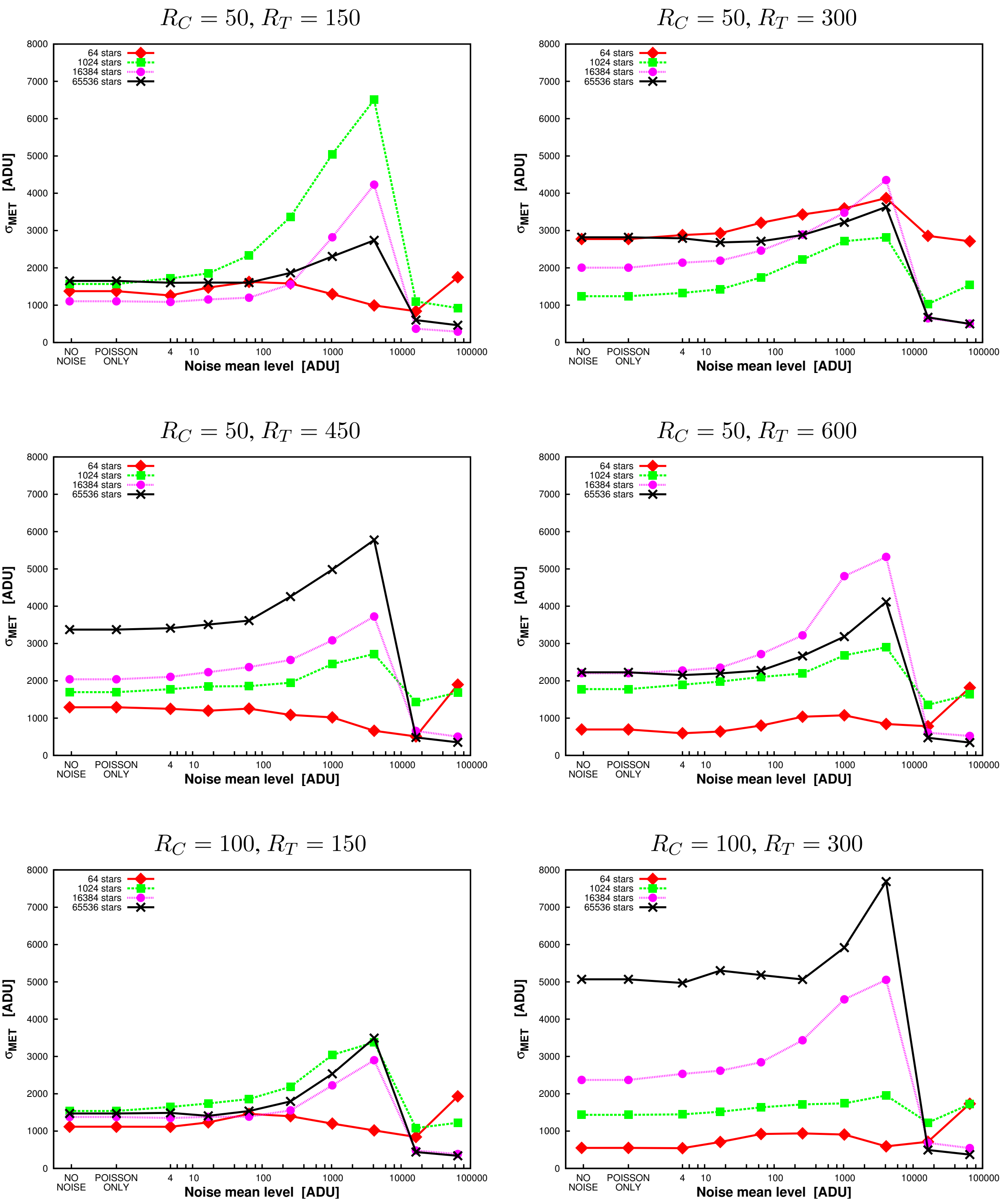

Figure 41: Evolution of σ_{MET} on the noise level for various spatial distribution parameters (part **A**). *Poisson only* - no additive noise, only non-uniform Poisson signal modification. *No noise* - no noise modification at all.

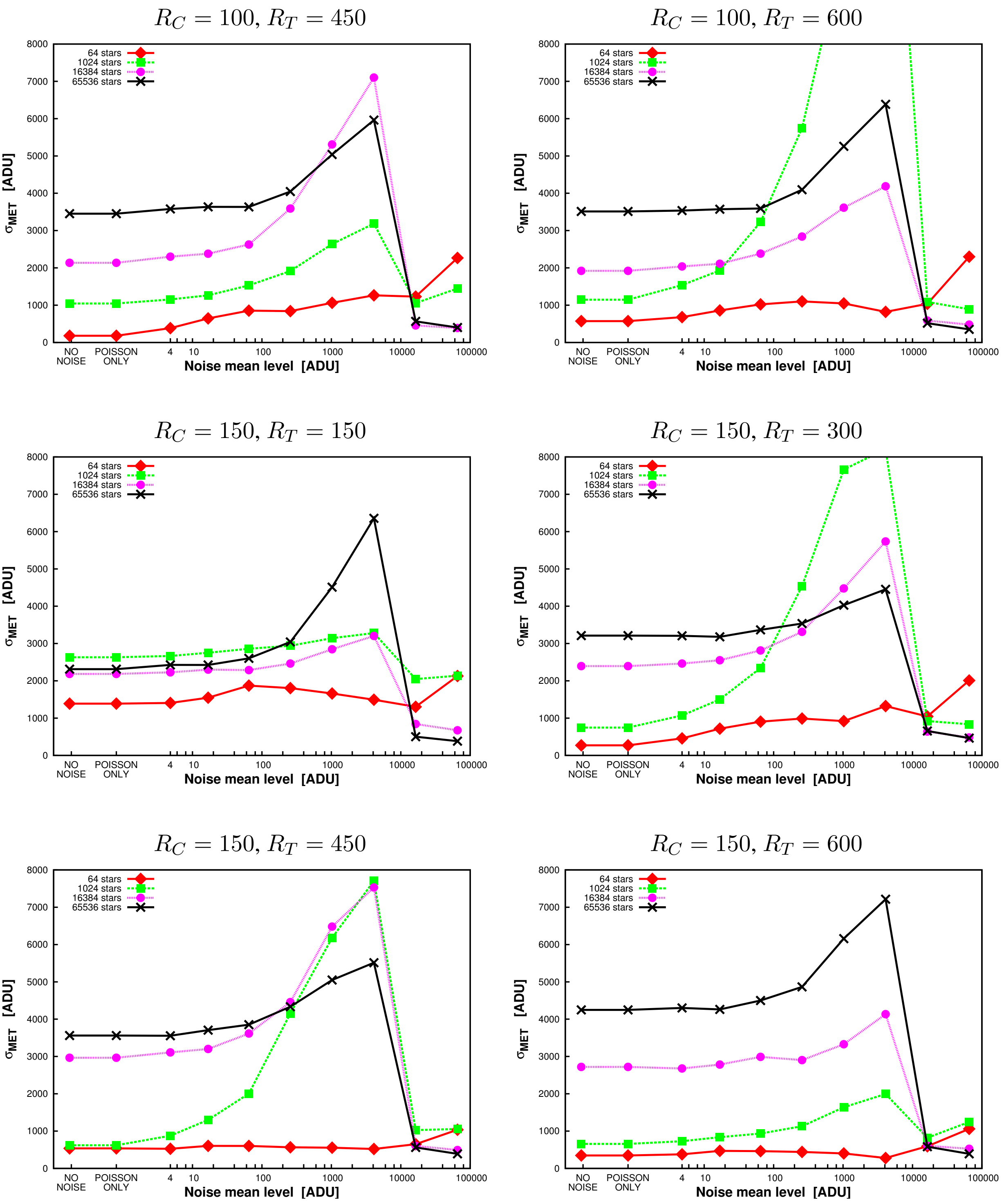

Figure 42: Evolution of σ_{MET} on the noise level for various spatial distribution parameters (part **B**). *Poisson only* - no additive noise, only non-uniform Poisson signal modification. *No noise* - no noise modification at all.

9.3 Influence of PSF shape

In this section the influence of the Moffat PSF shape [46] used for deconvolution on the resulted astrometric and photometric accuracy is discussed. All following diagrams show the four discussed accuracy parameters this time in their absolute value - N_{OK}, N_{NOT}, N_{OVER}, σ_{MET}. Their dependance on the Moffat PSF paramaters α and β is shown in figures 43, 44, 45, 46, 47, 48, 49 and 50. Each couple of figures is marked for two sets of numbers of stars - low 64 initial stars and high 16384 initial stars. In each figure there are 6 diagrams with same resolution and colour range for 6 different noise situations (*No additive noise* marks only non-uniform Poisson signal modification). For visualizations of multidimensional datasets the following parameters were set fixed in this section - spatial King's distribution set to sparse GCl - $R_C = 150$ and $R_T = 600$ - and maximal flux of the initial stars in the map set to the highest option 65536 ADU.

The figures 43 and 44 show the success of the stellar registration for 64 and 16384 initial stars. Surprisingly or not, it is evident that **for any level of the noise the the astrometric efficiency in the terms of N_{OK} decreases with larger α and lower β Moffat parameters**. Interesting thing is that all 6 diagrams with various noise look roughly (not exactly) the same which indicates strong dependance on the shape of PSF regardless the noise level for high signal-to-noise ratio (all the 6 diagrams show the cases when the signal flux is statistically significantly higher or maximally roughly equal in last diagram with $\bar{D} = 65536$ ADU). The figures 45 and 46 show the complementary diagrams with the information about N_{NOT} confirming the previous observations.

Much more interesting situation starts with the figures 47 and 48 showing the number of fake discoveris. As expected there are no fake stars after deconvolution for the cases of no noise. Yet the number grows significantly with the higher noise (unlike the previous observations). There is as well obvious tendency for higher parameters α and lower parameters β - this time though making the R-L deconvolution safer and more robust in the terms of fake discoveries! **Unlike in previous astrometric accuracy the larger α and lower β Moffat parameters makes deconvolution less vulnerable to leave fake residua which could be potentially called as fake discoveries!**

Another interesting observation can be made from the figures 49 and 50 containing the metrics σ_{MET}. Like in astrometric accuracy analysis, the efficiency of accurate flux estimation decreases (σ_{MET} gets higher) with larger α (related to larger astronomical *seeing* and larger FWHM) and lower β Moffat parameters (related to the higher *sharpness* of the PSF shape). In this case **the higher the noise level is, the higher are σ_{MET} differences between various shapes of PSF.** This information is actually predictable, the higher noise level, the lower flux estimation accuracy after deconvolution. While as discussed above the noise level does not influence much if the star was registered well or not unless the SNR gets close to or under 1 ratio significantly.

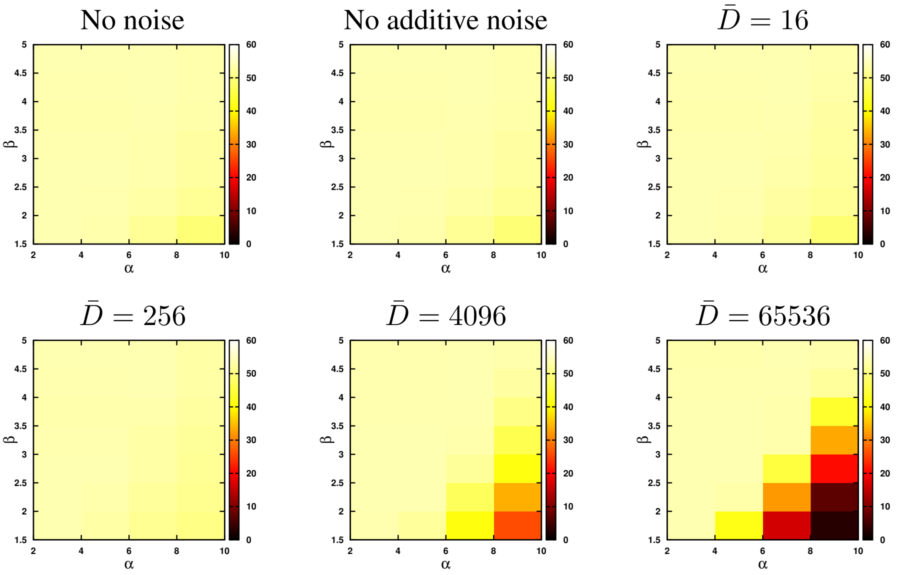

Figure 43: Dependence of the number of correctly registered stars N_{OK} after deconvolution on the PSF shape - Moffat parameters α and β - for the cas of **64 initial stars** on the simulation. Each image represents various noise levels (central-top for only non-uniform Poisson signal modification).

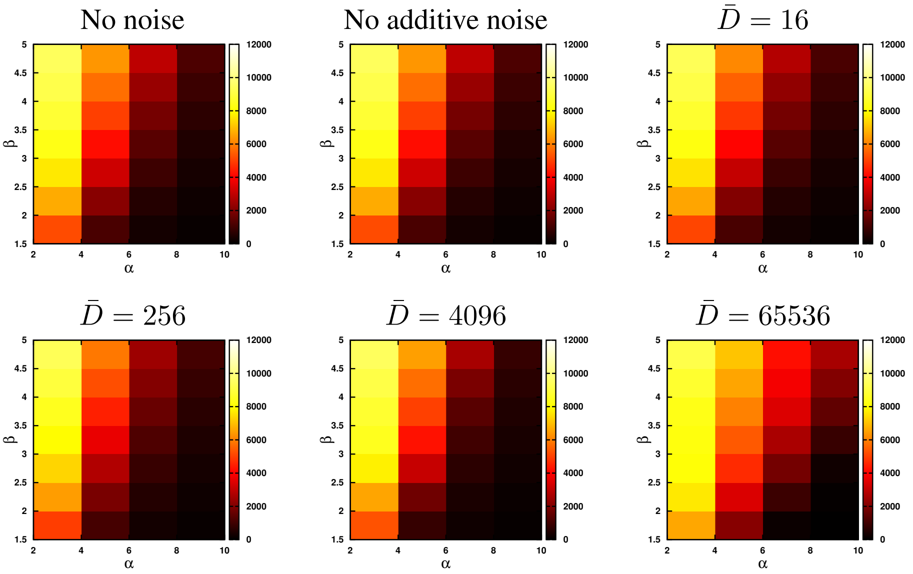

Figure 44: Dependence of the number of correctly registered stars N_{OK} after deconvolution on the PSF shape - Moffat parameters α and β - for the cas of **16384 initial stars** on the simulation. Each image represents various noise levels (central-top for only non-uniform Poisson signal modification).

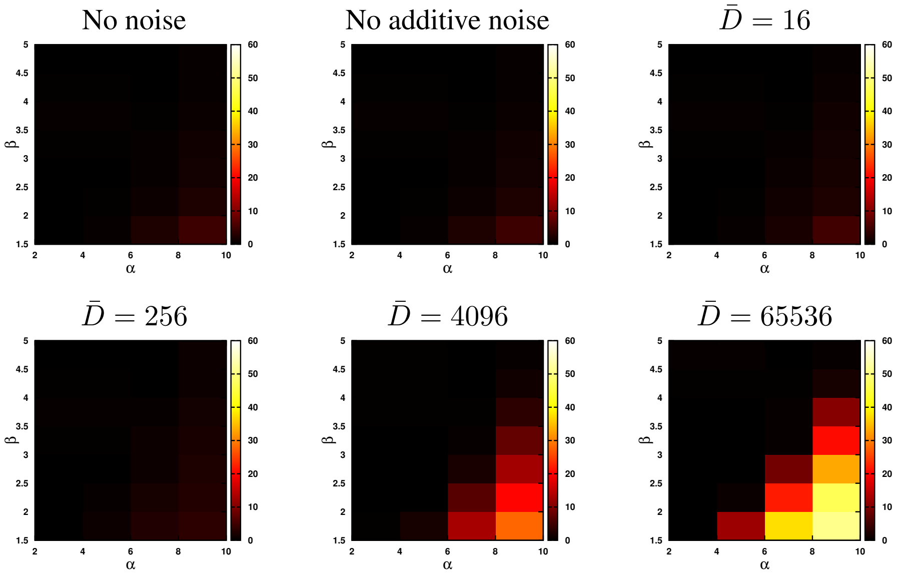

Figure 45: Dependence of the number of non-registered stars after deconvolution N_{NOT} on the PSF shape - Moffat parameters α and β - for the cas of **64 initial stars** on the simulation. Each image represents various noise levels (central-top for only non-uniform Poisson signal modification).

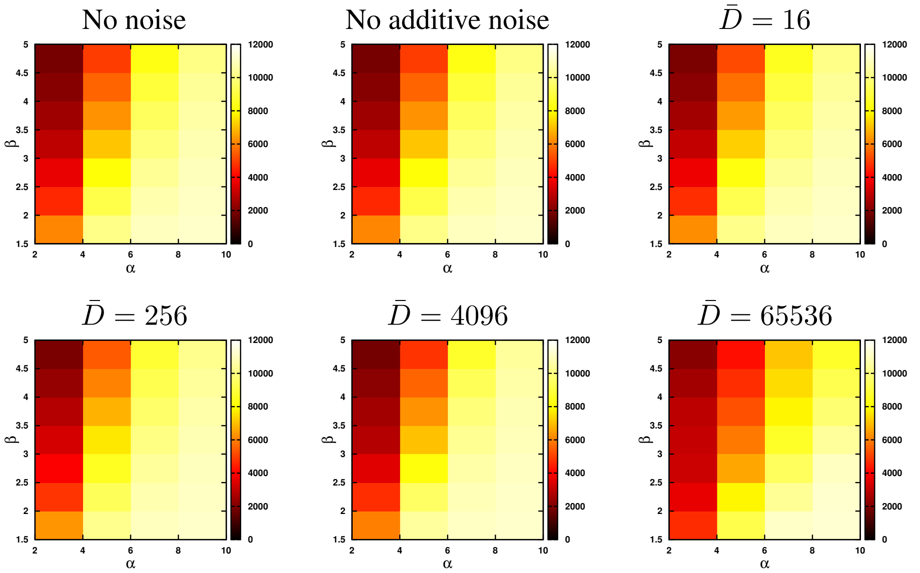

Figure 46: Dependence of the number of non-registered stars after deconvolution N_{NOT} on the PSF shape - Moffat parameters α and β - for the cas of **16384 initial stars** on the simulation. Each image represents various noise levels (central-top for only non-uniform Poisson signal modification).

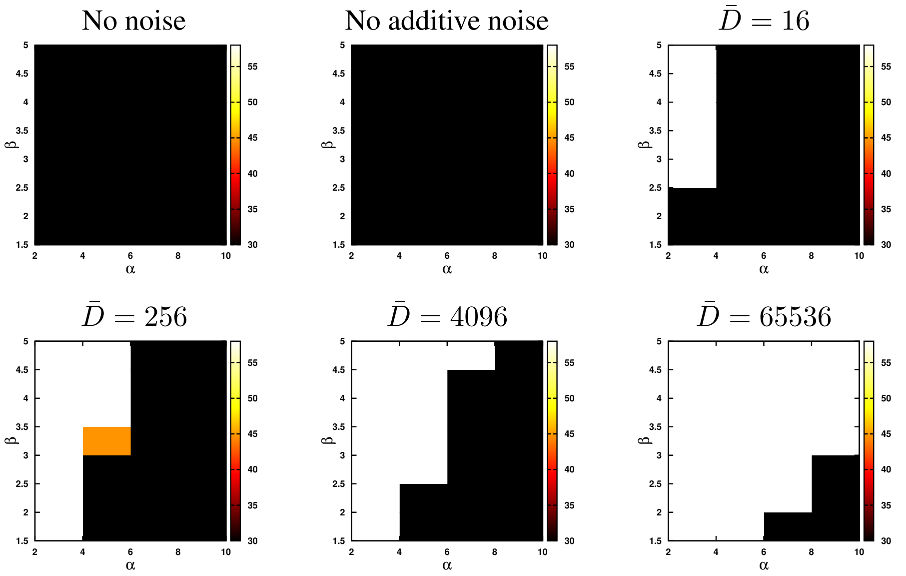

Figure 47: Dependence of the number of fake discoveries N_{OVER} on the PSF shape - Moffat parameters α and β - for the cas of **64 initial stars** on the simulation. Each image represents various noise levels (central-top for only non-uniform Poisson signal modification).

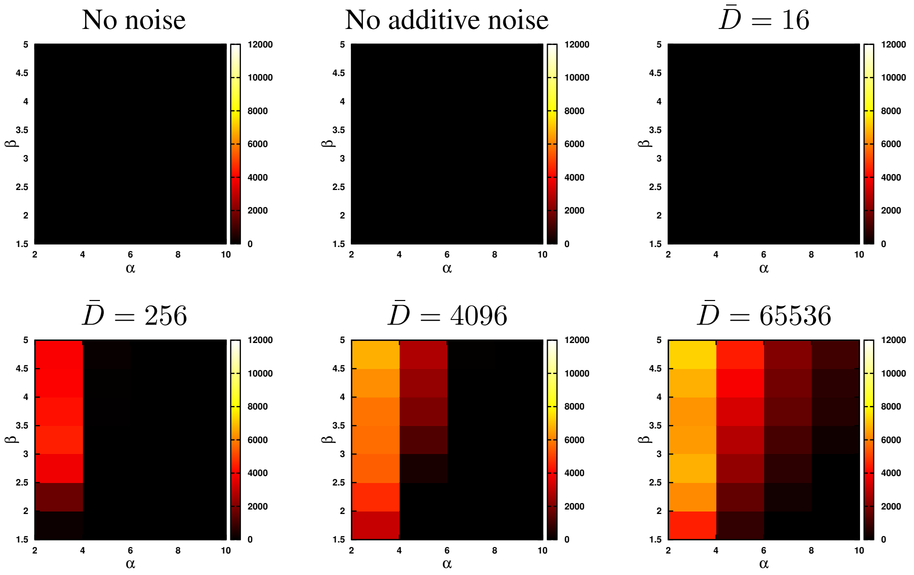

Figure 48: Dependence of the number of fake discoveries N_{OVER} on the PSF shape - Moffat parameters α and β - for the cas of **16384 initial stars** on the simulation. Each image represents various noise levels (central-top for only non-uniform Poisson signal modification).

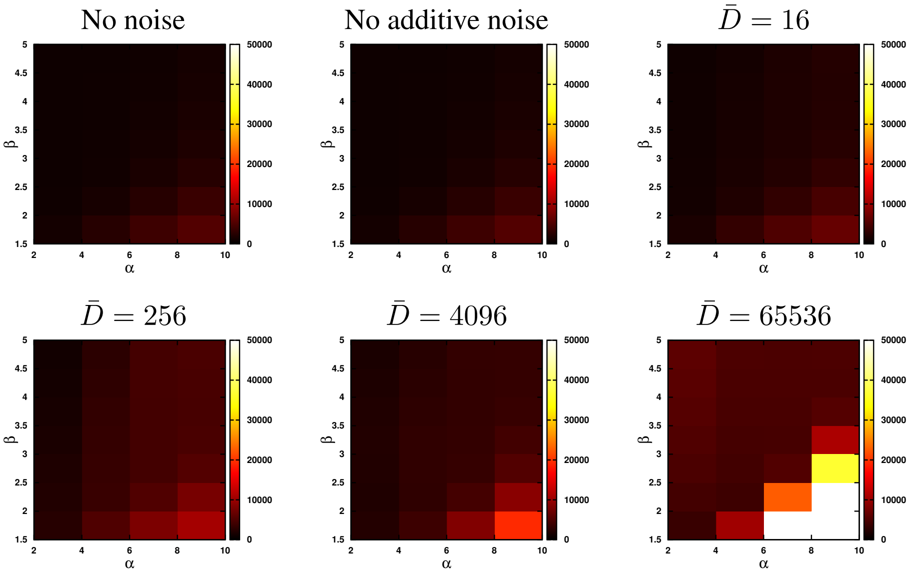

Figure 49: Dependence of σ_{MET} from (37) on the PSF shape - Moffat parameters α and β - for the cas of **64 initial stars** on the simulation. Each image represents various noise levels (central-top for only non-uniform Poisson signal modification).

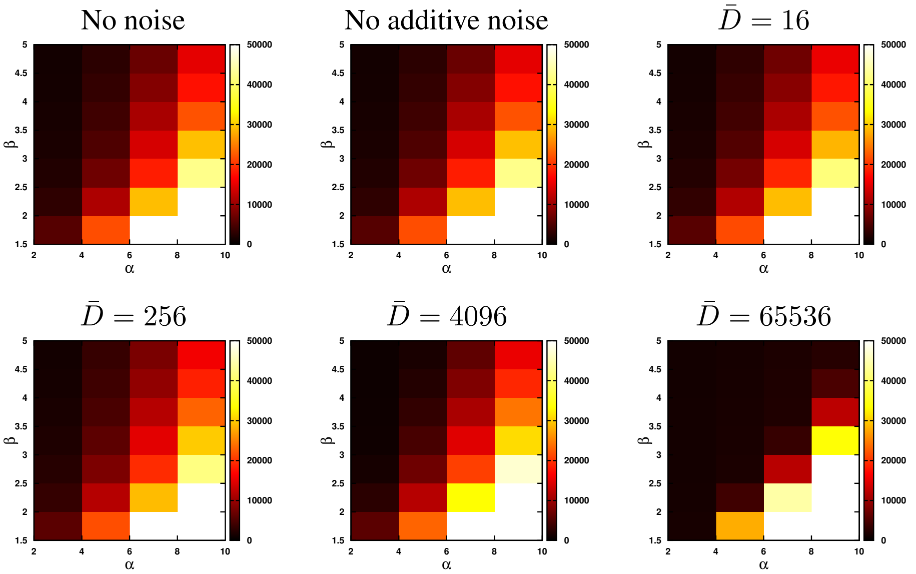

Figure 50: Dependence of σ_{MET} from (37) on the PSF shape - Moffat parameters α and β - for the cas of **16384 initial stars** on the simulation. Each image represents various noise levels (central-top for only non-uniform Poisson signal modification).

10 Nelder-Mead optimization in search of image properties

This section describes the effort to estimate the image characteristics (PSF, the number of stars, noise level, ...) of the simulations of crowded fields by the Nelder-Mead optimization method [36]. Simulations were created as before by the software GlencoeSim [12] described in the section 7. The idea is to combine the deconvolution process with parameter optimization. As in previous sections, the advantage of having simulations is to compare the results with the original initial maps of point stars - non-blurred and not noised. With any proper metrics, one can then test the efficiency of any algorithm to get the estimation of such a map from blurred and noised simulation.

The Nelder-Mead method [36] is a mathematical unconstrained nonlinear optimization looking for a scalar minimum of a generally complicated function with a higher number of variables. The idea of the algorithm is following:

1. Create the initial map, PSF and noised simulation by GlencoeSim.
2. Apply R-L deconvolution [54, 7, 57] with various input parameters (number of iteration, convergence criteria, PSF shape) on the simulation.
3. Calculate any metrics to describe the difference between the deconvolution result and the initial map.
4. **Repeat the steps 2 and 3 continuously by Nelder-Mead optimization method [36] with many different types of variables (PSF shape, convergence criteria, ...) until the metric converges to the minimum.**
5. Estimate the parameters of the image according to the optimization results.
6. Analyse the efficiency of such a procedure in term of which parameters are influencing the deconvolution results the most, for many possible variations of simulations (as given in table 10 in section 8).

Such an algorithm should work first for unnoised and only blurred simulations (no additional noise nor any non-uniform Poisson noise) before it can be enhanced to noised simulations. There can be many metrics chosen as one scalar number (necessary for the Nelder-Mead mathematical optimization) for expressing the 'proximity' of the initial maps and the deconvolution results :

- the sum over an image of the divisions between the deconvolution result and the initial map,
- the sum of the only pixels being over the image median value (getting the information about higher disproportion of the deconvolution result, which is generally wanted - from blurred stars,

it should ideally create narrow point stars backwards with many other pixels becoming less important and with lower values),

- simple RMSE (calculated as standard deviation of the pair - deconvolution result and the initial map),
- metrics σ_{MET} from (37) used in the section 8.2 for deconvolution efficiency,
- number of maximal values above median (similar to quantile statistics [44])
- and finally, some metrics containing the information about the 'sharpness' of the deconvolution result.

When assuming the better deconvolution result ideally gets sharper shapes of stars with higher disproportion between the pixels containing larger and smaller values when the more efficient the deconvolution is, then the last mentioned metrics and the RMSE should fit best for our case. While RMSE is not exactly best because any deconvolution may result into a situation of pixel values having a difference in degrees to other deconvolution result, so the minimal RMSE optimization could give for instance the solution for 'good deconvolution procedure' the result where everything is even much blurred than before, while compared to the 'correct deconvolution procedure' it has a better degree of pixel values on the image result.

The following proposed metrics for the Nelder-Mead optimization tries to describe the 'sharpness' of the deconvolution results.

1. Take the image with the result after the deconvolution.
2. For each pixel of the image calculate the square root sum of the 8-neighbour differences between the value of the pixels themselves and their 8 neighbours. This number describes the 'sharpness' of the pixels neighbourhood - the smaller the value is, the smaller the image gradient at this neighbourhood.
3. Divide this sharpness parameter by the actual pixel value (which may vary a lot with different deconvolution methods regardless the real value on the initial map).
4. Sum all these ratios over the image pixels.

The maximization of such a metrics (or practically by computer, to use the minimization of its negative value or inverted fraction) **could get to the point of the most sharp deconvolution results even without the knowledge of the initial map**, which could be then used just for confirmation of the correctness of the results by the test parameters discussed in section 8.2 ($\frac{N_{OK}}{N_*}$, $\frac{N_{NOT}}{N_*}$, $\frac{N_{OVER}}{N_*}$, σ_{MET}).

The practical test of the optimization method described in this section should first work on the non-noised images. Tests were processed under following different conditions - different number of optimization parameters (PSF shape, a number of iterations, ...), all the metrics mentioned in this section used (not only the most suitable 'sharpness' metrics), various initial Nelder-Mead conditions, different images of globular clusters with even easy parameters (low number of stars, high signal values, high PSF resolution, its analytic Moffat shape). **All the tests show strong sensitivity on initial Nelder-Mead input parameters!** The main problem is the *local* minima searching principle of Nelder-Mead optimization method and not the *global* one or at least any resistance against mathematical trapping inside a tiny local pit of scalar dependence on a huge number of input variables (whole images and their deconvolution results). Even the most simple search of correct PSF Moffat shape depended not on the 'correctness' of α and β parameters (with all other parameters known), but on the trapping in some values α and β close to initial values - the metrics was correct and the known deconvolution would provide the minimal value of the 'sharpness' metrics for instance correctly, although the optimization itself always converged to some local scalar pit!

The Nelder-Mead optimization algorithm [36] is highly sensitive in such complicated system as crowded field deconvolution in term of searching for most fitting deconvolution parameters. It may be used only when initial algorithm input parameters are already well known to refine the results.

11 Summary of partial results

In this chapter, the results from previous sections are outlined. They represent the steps and hints to design the better and reliable mathematical algorithm to analyse the crowded fields in the astronomical image processing with as few human interventions as possible. That algorithm (WHIDE) is designed in the next chapter 13. From the previous chapters, the **following hints and results** were gained.

- The automatic approach in the case of unknown initial PSF may combine the deconvolution with the iterative numerical photometry (see sections 4.5.3 and 4.5.4).
- Deconvolution deals better with the shape of PSF than the iterative numerical profile photometry (see section 4.5.4 and 9.2).
- The best suitable deconvolution method for crowded fields from the ones compared is Richardson-Lucy [57, 54] (R-L) which does not need to be modified itself, does not need usually more than dozens of iterations, but needs complex interpretation in terms of artefacts (rings, fake stars), thresholding and self-correction of proper PSF choice (see sections 5 and 9).
- The complexity of real data having space-variant PSF suggest the possible use of two other methods to enhance the efficiency of the algorithm - analytic modelling of optical aberrations by Zernike polynomials [2] and the image processing method dealing with super-resolution [13].
- Good metrics to describe the efficiency tests is the metrics σ_{MET} from (37) to be used with data simulation (see sections 8.2 and 8.5).
- The σ_{MET} ($\sim$ 'photometric error') does not grow quadratically or exponentially with the number of the stars in the cluster, but just roughly linearly with the quadratic growth of a total number of stars (see section 9.2.3).
- **All observed parameters of the deconvolution efficiency** (σ_{MET}, N_{OK}, ...) **grow much slower than with square root dependence on SNR ratio** (see section 9). This is particularly important in the proposal of the new idea of stellar weighing step of WHIDE algorithm in the following subsection 13.1.
- For any level of the noise, the astrometric efficiency decreases with larger FWHM and higher sharpness of PSF (see section 9.3).
- The larger FWHM and higher sharpness of PSF make deconvolution less vulnerable to produce strange residua which could be potentially called as fake discoveries (see section 9.3).

- The higher the noise level is, the higher the photometric errors between various shapes of PSF (see section 9.3).
- Nelder-Mead optimization can be used to iterate the deconvolution process only in the case that the PSF is very precisely known and only slightly varying (see section 10), but due to its trapping in local (not global) minima, it cannot be used as the main iterative process.

12 Design of ”Flux histogram noise thresholding” algorithm

In this section the use of initial knowledge of observed objects in the images is used to develop general criteria which could be used in **automatic processing** of crowded fields. Such a criteria could make the iterative numerical procedure (as described in the sections 4.5.3 and 4.5.4) automatic. Until recently thresholding is commonly used usually corresponding with the visual check of all individual results by the astrophysicists reducting the data manually in the case of complicated fields or GCls [17]. In this section the use of flux histogram shape with the estimation of the noise is suggested to be used as the automatic criteria founder, which would allow reliable automatic algorithm for image processing of crowded fields. Such an algorithm would combine namely - iterative numerical approach [17] (see sec. 4.5.4), Richardson-Lucy deconvolution [54, 57] (see sec. 9) and the proposed method which could be called **”flux histogram noise thresholding”** as suggested and explained in this chapter.

The important thing in the automatic object recognition (such as car plates numbers, robotic vision, road signs recognition, ...) is the assumption of what is expected to be seen in the image [58]. In the case of globular clusters in the astronomy this can be used for the estimation of the **noise** and luminosity function of the appropriate stars.

The common way how to estimate the noise is to get the mean values and Gaussian standard deviations (due to the central limit theorem Poisson distribution converges to Gaussian at higher/infinite parameters [1]) inside some annulus around analysed star. Such an approach is extremely inconvenient in the case of crowded fields where no lone stars can be found. Usually the manual thresholding during the data reduction is set (commonly as the multiplication factor of the standard deviation [17]) to secure that no noise peaks are taken as potential stellar candidate. Deconvolution is dealing well with such a noise and determining whether the shape of such a small peak inside the noise range has or has not a shape of preferred PSF. The results after deconvolution decrease the noise pixels down to zero, yet never completely and many times new residual artefacts occur. So the mathematical problem of choosing the threshold is not solved, but rather postponed to the other higher step of the algorithm (from aperture photometry to deconvolution).

Yet in this chapter the solution is suggested based on the assumptions about the observed objects. The following assumptions (not always 100 % accomplished in the real data, hence influencing the efficiency) should be accomplished :

- Stellar objects with generally monotonous luminosity function up to observational upper limits are in the image. This is valid for crowded fields - globular clusters (GCl) and random stars - but not for objects like planets or galaxies (in case they are not hidden in the additive cosmical background).
- Proper darkframe procedure has been accomplished - many non-thermal types of noise given

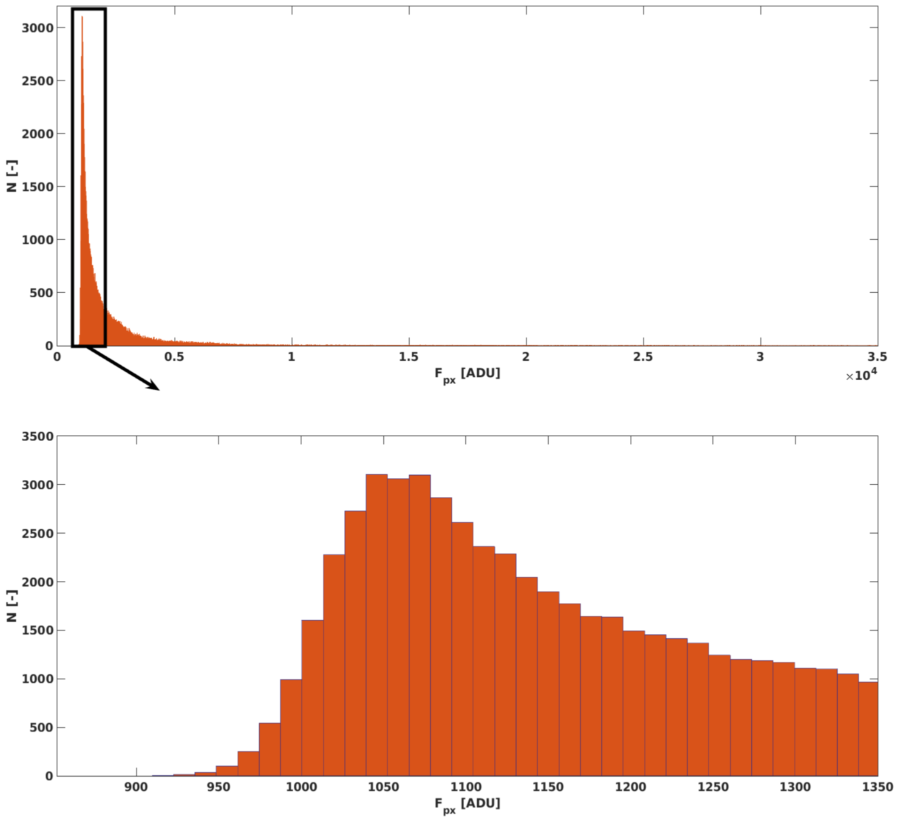

Figure 51: Histogram (and its detail) of the simulated GCl with 1024 estimated stars, max. flux 65536 ADU, $\alpha = 6$, $\beta = 2$, additive noise with est. mean of 1024 ADU (see fig. 52).

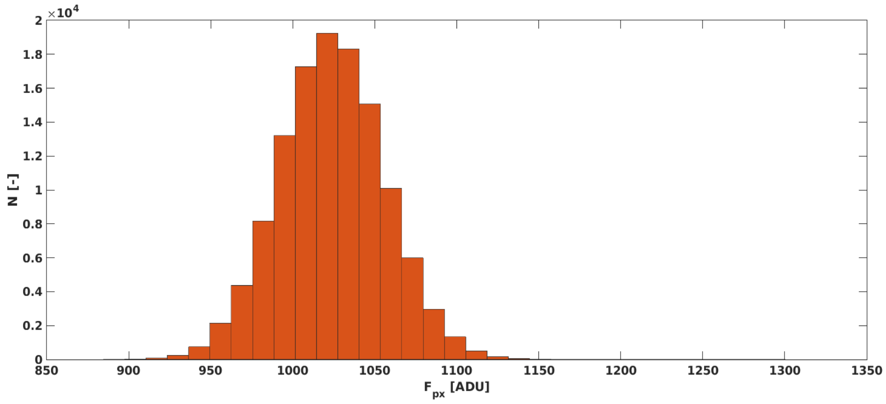

Figure 52: Additive Poisson noise used for simulation of the GCl at figures 51 and 53

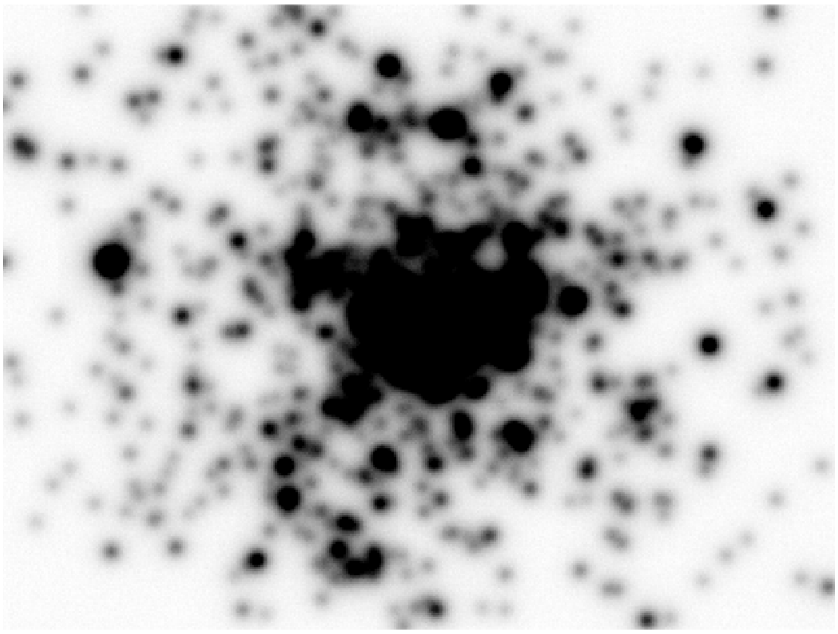

Figure 53: Simulation of the crowded field used for the demonstration of the algorithm of ”flux histogram noise thresholding”.

by the electronics do not follow additive Poisson Probability Density Function (PDF) and may influence the noise histogram significantly [42].

- Noise follows the Poisson distribution - valid for additive background noise and signal dependent noise modification (see sec. 7.3).

12.1 Algorithm of the turnpoint and threshold estimation

Figure 51 shows the flux histogram of the simulation given in figure 53. The values represent number N of the pixels having the values around F_{px} (with given histogram bin width). Its bottom graph shows the detail in the most interesting part of the histogram, which is mainly the additive noise. Although not exactly - figure 52 shows the noise used as $N(x, y)$ from (3) for the simulation in figure 53 by the GlencoeSim simulator [12] (see sec. 7). It is evident that during the simulation by adding the faint stars the shape of the histogram changed significantly. The explanation of the algorithm of ”flux histogram noise thresholding” will be done in this example (figures 51-54). As we know from the simulation the estimated (set) attributes should be $\bar{F} = \lambda = 1024$ ADU. Poisson distribution (Probability Density Function - PDF)

$$PDF = e^{-\lambda}\frac{\lambda^x}{x!} \tag{41}$$

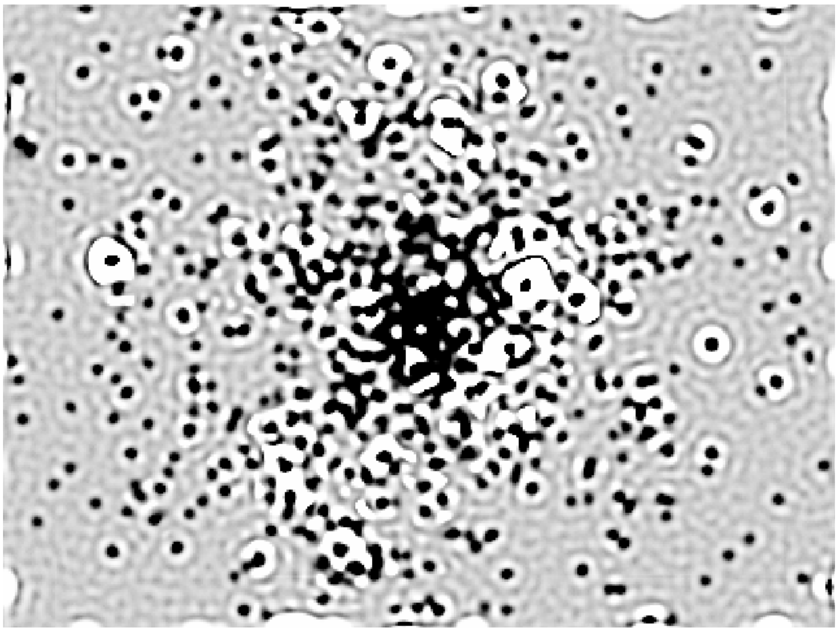

Figure 54: Richardson-Lucy deconvolution of the image 53.

has the second central moment (estimation of standard deviation) equal to the square root of the estimated mean value λ :

$$\sigma_{PDF} = \sqrt{\lambda}. \tag{42}$$

For this case the simulated additive noise (used for the GCl in figure 53) has indeed

$$\bar{F}_{add} = 1024.02 \pm 31.94.$$

Following procedure shows the idea how to get the estimation of this value from the realistic histogram of the illustration crowded field in the image 53 with its histogram in figure 51. The idea is based on the assumption that the shape of the Poisson PDF of the noise is (logically) best fitting in the left wing of the histogram from its peak.

1. Fit Poisson PDF on whole histogram and estimate λ parameter.
2. Throw away all pixels having values **above** $\lambda + \sqrt{\lambda}$.
3. Iterate again from step 1 until no pixels are thrown away.
4. Save the iterated λ parameter for future use.
5. Create smooth analytic PDF (with the same discrete binning as the histogram data) with Poisson shape and λ parameter according to 41.

6. Normalize this analytic Poisson PDF that it fits best to the histogram data with all the higher pixel values thrown away (as given by the steps 1-3).
7. Deduct the normalized analytic PDF from the histogram data.
8. **Get the position F_{TURN} with maximal value in such a differentiated histogram - this position can be regarded as a *turnpoint* of the original histogram. It can be interpreted as a point where there is a maximal growth of stellar pixels compared to the maximal decrease of the noise pixels.**

Steps 1-3 of this procedure converge usually pretty quickly on real data (several/dozens of iterations only), and it is not never ending loop (it is not throwing potentially all pixels away). The graphical illustration of the algorithm designed above is in figure 55. The upper graph shows the histogram of the Globular cluster simulated with the additive noise having $\bar{F}_{add} = 1024.02 ADU$ (brown boxes). Steps 1-4 provide (without the implicit knowledge of the noise distribution) the estimation of λ parameter as

$$\lambda = 1026.01 \pm 32.03 \text{ ADU},$$

which is extremely close to the value by which the image was simulated (1024 ADU)! Especially compared to the maximal value of histogram in the position

$$F_{px,max} = 1046.0 \pm 3.3 \text{ ADU},$$

which could be suggested by standard photometric methods as the estimated noise value. The most important part of figure 55 is the bottom graph, which represents the deduction of normalized analytic PDF from the original histogram. The **turnpoint** F_{TURN} is marked there at the position of

$$F_{TURN} = 1096.0 \pm 3.3 \text{ ADU}.$$

12.2 Interpretation of the turnpoint and deconvolution threshold

The physical interpretation of such a turnpoint can be :

- flux level below which one the number of background noise pixels is growing faster than the number of detectable stars,
- estimated upper limit of the noise (given by completely different process than in standard astrometric or photometric algorithms [17], see sec. 4.4)
- or **the differential threshold when compared to the estimated λ value of the analytic PDF**.

The disadvantage of the deconvolution is that while depending on the noise and PSF shapes it creates residual artifacts (rings, stars, circles, fake stars). While the beauty of the computational results after discrete deconvolution is its tendency to ”enhance” the ”well shaped” objects up into higher values and to decrease the unprobable noise pixels down to zero levels. As this ”zero level” is equal to the λ value in the original image then the threshold inside discrete deconvolution results T_D is equal to the ”turnpoint” level in the original image :

$$T_D = F_{TURN} - \lambda. \tag{43}$$

Also, it is important to keep in mind, that such a threshold is valid in the case the deconvolution sends ideally most of the noise pixels to zero levels (which often happens). If the integer median

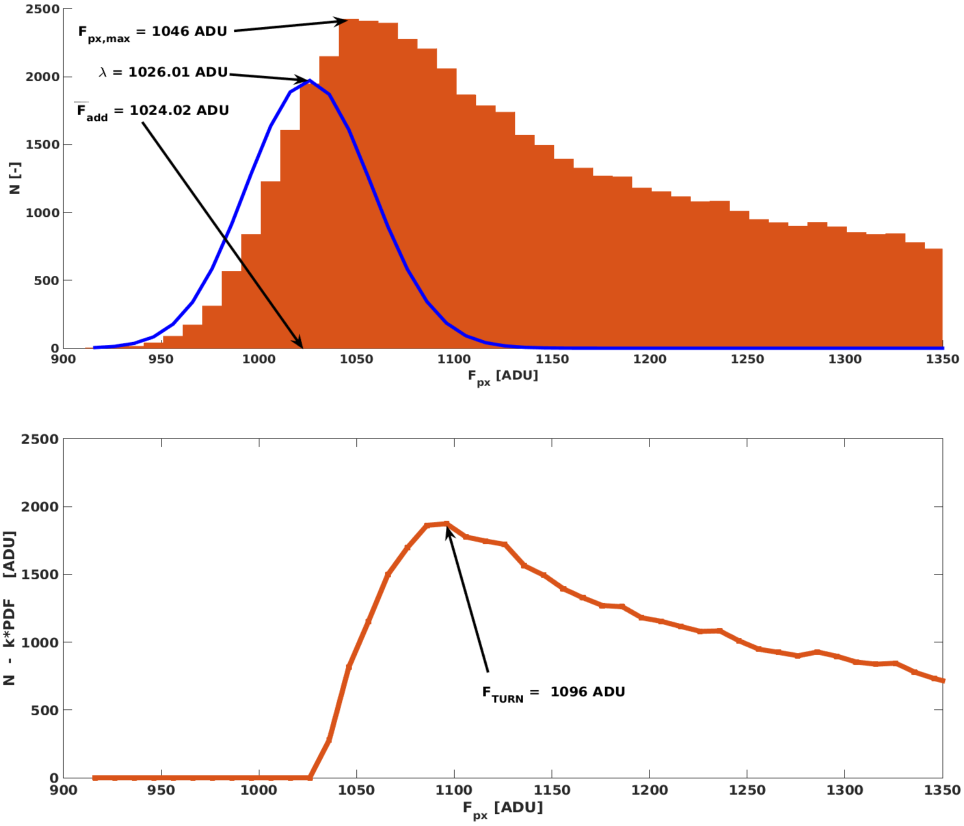

Figure 55: Illustration of the method to get the turnpoint F_{TURN} from the original image histogram and the analytic PDF estimation of the additive noise. The analytic fitted normalized PDF has λ value much closer to the implicitly unknown distribution of the additive noise. The turnpoint then can be found from the deduction of the histogram by the analytic normalized PDF as the maximal point above the λ level.

$\mathrm{med}(D)$ of the deconvolution resulted image $D(x, y)$ is non-zero then it is important not to forget to add this median value to the calculated threshold T_D :

$$T_D = F_{TURN} - \lambda + \mathrm{med}(D). \tag{44}$$

The equation (44) works for any level of the additive noise in the simulations, of course regarding the un/success of the deconvolution (wrong PSF, few iterations, low SNR) it can provide under harsh circumstances no probable stellar deconvolution results. But its advantage is to provide general algorithm how to get criteria for **automatic deconvolution thresholding** regardless the data condition and the experience of the person analysing the data. The usage of such o threshold is evident from the figure 54 where the R-L deconvolution results are shown for the illustration image 53.

Although for the best error-efficiency it is crucial to choose 'proper binning' of the histogram creation. The author tried many options used in the community [44] while the best suitable binning for the analysis designed in the previous subsection seems to follow these rules:

- Sturges formula [60] of the number of bins k in dependence on number of analysed pixels n

$$k = \log_2 n + 1 \tag{45}$$

- and the number of analysed pixels n to get the binning width may not be the total number of the pixels on the image, but just the pixels included in the determination of the analytic Poisson PDF (steps 1-3 in the algorithm description, see previous sec. 12.1).

13 Design of WHIDE - Weighed and HIstogram thresholded DEconvolution algorithm

In the chapter 11 the results were summarized and in this chapter they are used to design the new complete algorithm to deal with the image processing of the crowded fields in astronomy. Such an algorithm combines several already known methods (namely the R-L deconvolution), but (based on the results in previous sections) it generally adds two new ideas.

1. To get the process automatic, it uses the method designed in the previous chapter 12 - **"Flux histogram noise thresholding"** algorithm.
2. The second idea suggests switching two steps in their order compared to as they are commonly processed by the astronomical image processing for the case of many images of the same observational object - **to perform the main deconvolution and any other image processing without (before) mathematical averaging (or summing) of these many images of the same object!** The details and the reasons for it are explained in the subsection 13.1.

The proposed WHIDE algorithm needs several assumptions to be made. It has its limits given by the following conditions.

- The stellar FITS image has been rid of unthermal noise by darkframe (which is dealing both with thermal and the unthermal types of noises [42]). Then the background noise can be described by Poisson additive noise and the modification of signal just by non-uniform Poisson noise.
- There are no other 'flat' objects on the image, and it consists of stellar point sources at least up to the observational limit of the instrument. Then these flat objects (namely deep-sky objects) are 'hidden' inside additive Poisson noise.
- At least 'few' sources can be found isolated and have 'significantly high' SNR (for the first estimation of PSF).
- The luminosity function of the stars is generally monotonous up to the noise levels.

13.1 Stellar weighing step of WHIDE algorithm

In this subsection, the new (heretic) idea for the case of several different image observations of the same object (crowded field) is proposed. Usually, the most simple way to get rid of the background noise in the astronomical images as much as possible is to combine these N images by averaging or summing (or other mathematical process [17]). In such a way the variance (square standard deviation σ) of the background noise gets down [59] from one-image-deviation σ_1 to processed-deviation σ_N as

$$\sigma_N = \frac{1}{\sqrt{N}} \sigma_1, \tag{46}$$

while the average value of the background does not (theoretically) change. Such a background noise (or even non-uniform signal noise) of the processed image, of course, does not follow Poisson distribution anymore, even though the modified distribution (by $\sqrt{N}$) might be still potentially used. **Yet in this thesis, it is suggested in the case when performing the deconvolution process to NOT average these images together before the deconvolution itself!** The idea comes from one result in the previous sections - the R-L deconvolution **IN**efficiency (measured by any metrics - σ_{MET}, N_{OK}, N_{OVER} from the section 8.2) grow much slower than with square root dependence on SNR ratio (see section 9.2.3). If this is to be compared with the general law in (46), then it seems that **the complex R-L deconvolution from complex data with crowded fields tends to produce its artefacts and residua** (see figure 54 for illustration) **'regardless' on the SNR level**. The word 'regardless' is here chosen to express the comparison towards the influence of the denoising by (46). It is if course obvious that the artefacts and the photometric inaccuracy generally grow with the noise level (and many other complex conditions). But due to the analysed influence of the noise on the deconvolution results it is suggested **that more precise results would be obtained when the deconvolution is first applied to all the images separately and just after that the astrometric and photometric results are to be averaged and checked.**

The simplistic potential explanation for this unexpected behaviour of the R-L deconvolution might be seen in the tendency to send all probable noise to zero ADU levels with the artefact levels being obviously dependent more on the central peak deconvolved signal estimation of the star to which the artefact partly belong. Even though such a deconvolved signal is secondary of course dependent on the original image noise (producing self-inconsistency given by the naturalistic behaviour of the noise).

The question is then how to use the information given by the set of many images of the same object (which naturally gives the advantage in search of the reality hidden in the noise) after the deconvolution is performed on each of the images. The outcome of the deconvolution is not the image to be potentially averaged with the other results, but already the list of stars with three characteristics - two position coordinates (with errors) and relative (differential) flux estimation. In this thesis, the other flag parameter is suggested to keep with these astrometric and photometric results. This flag would contain the information about the statistical probability if such a stellar candidate in the crowded field is the residual artefact or not. Let this flag ratio w be defined as

$$w = \frac{F_D}{T_D} \tag{47}$$

where F_D is the signal value of each candidate after deconvolution (which is generally NOT directly comparable with the similar numbers from the other images in the set) and where T_D is the turnpoint threshold value given by (44) in section 12.

The ratio w from (47) is already comparable between the different images in the set, observing the same object. If it happens that some candidate is not found in any of these N images within the position errors then let the flag w value be zero. For each stellar candidate then these flags are *weighed* (hence the name of the designed WHIDE algorithm - Weighed and Histogram Thresholded Deconvolution)

$$w_N = \frac{1}{N} \sum_{k}^{M} w_k. \tag{48}$$

This operation gives the similar information as standard denoising by averaging of the images before processing the astrometry or photometry. Just in the case of WHIDE algorithm this averaging operation is performed AFTER processing the astrometry and photometry of the deconvolution results on each image in the dataset.

The interpretation of the *weight* ratio flag w is simple - the real stellar candidates keep their weight w over the value 1.

13.2 Procedure of the WHIDE algorithm

As discussed above, the WHIDE algorithm uses namely two new approaches based on Flux Histogram Noise Thresholding (to get the process automatic) and the weighing step with w flag (47) which allows combining the information from a larger dataset of the images - with not combining these images before, but after the deconvolution process inside WHIDE algorithm. The name is based on these two approaches - **W**eighed and **HI**stogram thresholded automatic **DE**convolution algorithm. Following is the outline of this WHIDE algorithm to perform the automatic photometry and astrometry of the crowded fields in given FITS images. Steps are described in the worst case of the unknown PSF (if PSF is well known then the steps 1-5 may be skipped).

1. Get the brightest of the symmetric ($\sim$ lonely) stars closest to the image center - this would create the initial PSF estimation.

2. Perform the Richardson-Lucy deconvolution with this zeroth PSF estimation with few ($\sim$ 20) iterations.

3. Calculate the 'sharpness metrics' as proposed in section 10.

4. Take the second (or other) brightest candidate star and calculate the same 'sharpness metrics.'

5. Continue down the list of candidates with the steps 1-4 until the 'sharpness metrics' is maximized.

6. Use this PSF and perform more precise R-L deconvolution ($>$ 80 iterations).
7. Get the estimation of λ parameter from 'cleaned' group of pixels (as described in section 12.1) where all pixels are under the iteratively fitted Poisson PDF with upper limit of $\lambda + \sqrt{\lambda}$. Save the histogram binning width for the later use.
8. Produce the Poisson PDF with given λ parameter normalized to given histogram cut of the pixels above $\lambda + \sqrt{\lambda}$.
9. Deduct this normalized Poisson PDF from the whole histogram (with a larger number of bins, yet their width unchanged) of all image pixels.
10. Get the turnpoint from the resulting histogram maximum above the λ noise level.
11. Calculate the threshold for deconvolution results by (44).
12. Create the lists of all local maxima on the deconvolution result and get rid of all maxima under the calculated threshold.
13. Take the resulting list as the astrometric input for the next profile photometry.
14. Calculate the flux by simple profile photometry with given PSF.
15. Give each analysed star beside the astrometric position and the profile photometry flux another important attribute (flag) representing the statistical probability of the star having correct information - 'weight' w from (47)
16. Perform all the steps 1-15 on the different image of the same stellar field. Adjust the astrometric position at 1-pixel precision, average the flux results and calculate the mean of the weight w from (48) - not found stars having the weight $w_k = 0$.
17. After analysing all the images of the appropriate globular cluster take into the account just the stars with the weight w being over the ratio 1 - this number can be interpreted so that the average SNR is at the histogram turnpoint edge.

14 Practical test of WHIDE algorithm and the results

The algorithm has to be practically tested, yet it is difficult to compare the results with some other methods for the case of the extremely dense crowded fields (GCl), when there are practically ”no reliable data to be compared” (which is actually the reason for this thesis topic to be researched) or extremely difficult to get and to analyse. Standard tool in astronomy is so called aperture photometry [17, 42] (see section 4.4 and (2)). For such a tool the data with the *semi-crowded* stellar field (open cluster with both many individual separable and several overlapping stars) was chosen to be analysed with both standard aperture photometry and the WHIDE algorithm. The combined (averaged) image of five raw preprocessed (darkframe, flatfield) stellar FITS images used for the test can be seen in figure 56 (open cluster called M67 or NGC2682). For the aperture photometry the standard astronomical package IRAF [63] was used. Threshold was set to default value 4-σ and the photometry was applied on the averaged image made from five FITS files.

The results can be seen in figure 57 where there are two charts of discovered and registered stars - left (purple) for the aperture photometry and right (red) for the WHIDE algorithm. Figure 57 shows just detail from the bottom right part of the image 56 while for the analysis whole images were used. The raw images contained dozens of bright overexposed stars producing blooming [42]. Such a defect is a big issue for the correct deconvolution which makes around overexposed stars (to the distance of tens of pixels) significant artefacts which are not eliminated by WHIDE algorithm. **It is important to use the images without such defects (overexposure) or to apply the cover mask** (which was done in our case). On the other hand, when looking more in the detail of figure 57, it is obvious that the automatic procedure WHIDE found correct stars even though it uses way different approach than the aperture photometry. For the given manual threshold of the aperture photometry - four background deviations - it even found weaker correct stars. The efficiency of both methods logically depends on the overall exposure (5 images per 10 seconds each with FOV of 20 arc minutes in our test), but as can be seen in the detail several stars with close faint neighbours were successfully detected by WHIDE algorithm (due to its deconvolution principle) while the aperture photometry failed to distinguish these few objects.

Figure 57 shows the astrometric success of the WHIDE algorithm, while the figure 58 shows the photometric flux differences in the measurement. For both analysis - WHIDE and aperture photometry by IRAF - the instrumental magnitudes are used [42]. For the WHIDE algorithm the peak deconvolved signal is used to produce the logarithmic magnitude (1) with one of the brightest star chosen as the reference star. Such a star has the magnitude $m_{REF} = (10.651 \pm 0.001)^{\mathrm{mag}}$ in the case of the second method - IRAF aperture photometry (DAOPHOT package [59]). The magnitude-magnitude diagram 58 then shows the flux measurement differences between the aperture photometry and the WHIDE

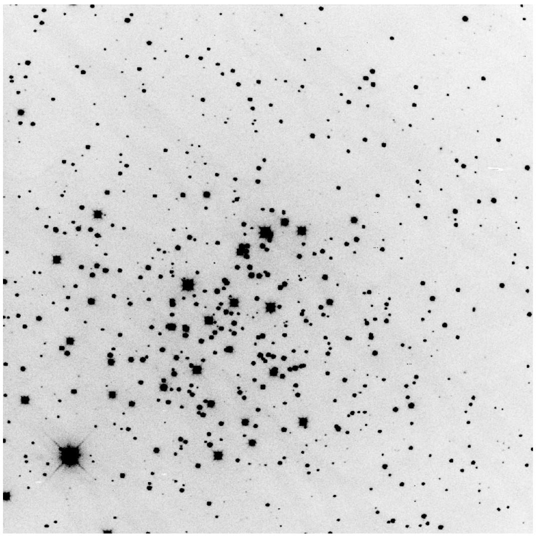

Figure 56: Real image of the open cluster M67 taken by the CCD camera FLI IMG-4710 used for the test of designed WHIDE algorithm in comparison with standard aperture photometry algorithm.

algorithm. On the x-axis, there is the WHIDE magnitude m_{WHIDE} adjusted to zero by the chosen reference star. The y-axis then shows the difference between the WHIDE calculated magnitude and the magnitude m_{IRAF} measured with IRAF package by the aperture photometry. The reference value m_{REF} only adjusts the numbers that the reference star has the relative coordinates (0,0).

From the diagram 58, it is evident that the flux differences (error) between the aperture photometry and WHIDE go from 0.3^{mag} for bright stars up to 0.6^{mag} error for the stars six magnitudes fainter. Such an error might be reasonable for the case of five 10-seconds observations, yet for many precise measurements this is insufficient. **It is clear that the strength of the WHIDE algorithm is namely in the astrometric object detections.** For the better precision of the photometric measurements, it seems more and longer observations are necessary (which is given by the statistical nature of WHIDE algorithm).

Successful test of the WHIDE algorithm on semi-crowded field shows its advantage both in the potential research of dense crowded fields, where the standard methods are useless and in the analysis of standard stellar fields where the automatic approach is regarded.

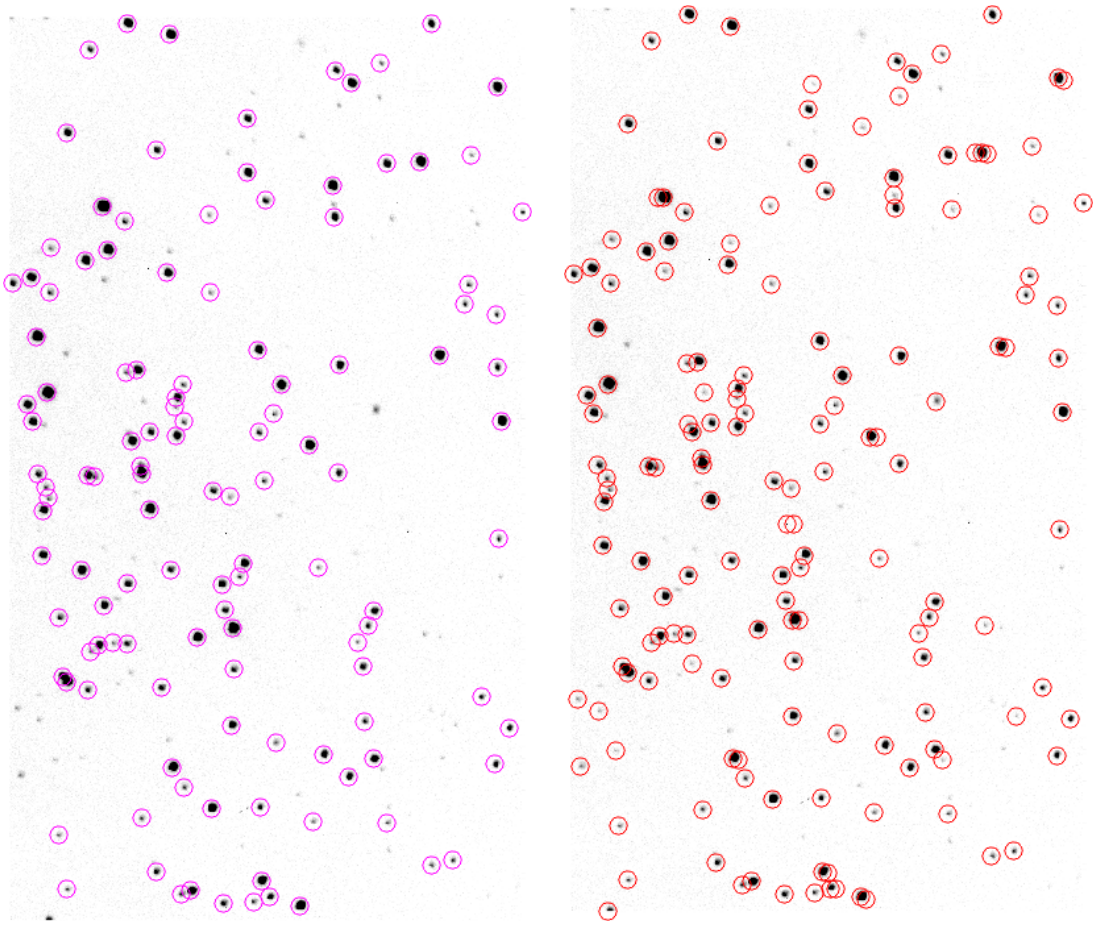

Figure 57: Test of the WHIDE algorithm (right, red) on the real astronomical data (open cluster M67 - figure 56) compared to the standard aperture photometry with the IRAF package (left, purple). Aperture photometry needs manual thresholding while it has difficulties by distinguishing several close neighbours. WHIDE method finds automatically even fainter objects and separates close neighbours, but it has to deal with the existence of the artefacts made by the estimation of the PSF. This points to the statistical behaviour of WHIDE algorithm which gets rid of the artefacts by longer observations from different instruments with different PSF.

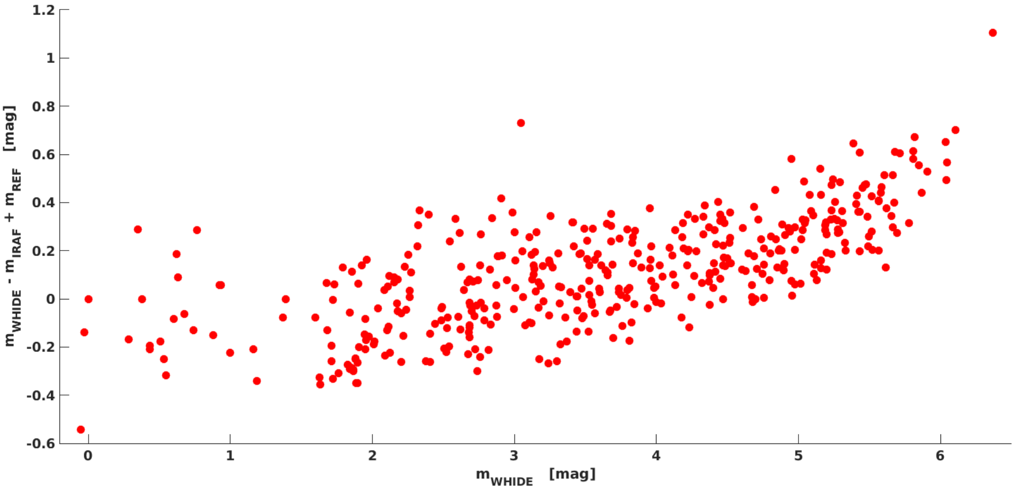

Figure 58: Error magnitude diagram of the M67 measurements (see figures 56 and 57). X-axis represents the magnitudes m_{WHIDE} of stars measured by WHIDE algorithm with the zero point adjusted to the reference star. The y-axis then shows the magnitude difference between the aperture photometry measurements m_{IRAF} and the already mentioned WHIDE measurements (modified by m_{REF} constant value of the reference star in IRAF results to adjust that star to (0,0) relative coordinates).

15 Conclusion

Image processing in astronomy deals namely with significant noise and optical aberrations. This thesis is trying to give new opportunity to analyse the images where the high stellar density prevents such an automatic data reduction. Large international astronomical catalogues still lack the radiometric information about dense crowded fields (such as Globular clusters or concentrated Open stellar clusters). In this thesis the research of various methods (including mathematical deconvolution, Nelder-Mead optimization, aperture and profile photometry, stellar registration, ...) is presented in search of a reliable automatic algorithm which would allow getting the information about the positions and fluxes of individual stars in dense crowded fields. As an outcome, it offers namely four new approaches and methods.

1. In chapter 7 the published simulator of astronomical crowded stellar fields - the GlencoeSim simulator - is presented.
2. ”Flux Histogram Noise Thresholding” method, which is used as a step in the designed WHIDE algorithm, and its description can be found in chapter 12. This method uses the knowledge of the observed data (monotonous luminosity function of point stars) and most importantly the noise distribution. The resulting advantage is to get the criteria for following Richardson-Lucy deconvolution analysis where such an analysis can now be done automatically.
3. The new idea to statistically weigh the deconvolution results before/without usual denoising operations (averaging of the images to get rid of noise). This approach, its description and its motivation is described in section 13.1. Generally, it is trying to get rid of the deconvolution artefacts by the statistical approach.
4. Finally, the proposed algorithm WHIDE is presented in whole chapter 13. Its design is based on the results received during the various analysis described at this thesis, standard methods described in the beginning of the thesis such as Richardson-Lucy deconvolution or profile photometry and finally two new approaches suggested in this thesis - statistical weighing and the thresholding by noise histogram. The name WHIDE is derived from these two approaches - Weighed and Histogram Thresholded Deconvolution.

The structure of the thesis was divided into three groups - research, simulations and algorithms design. Chapters 2 - 6 describe the current situation, definition of the studied topic and the tasks, overview of the systems where the proposed algorithms are potentially useful and the list of image processing deconvolution algorithms with their detailed description (and comparative analysis in section 5.3). Chapter 7 presents the algorithm and description of the newly designed simulator GlencoeSim and chapters 8 - 9 show the results from the performed simulations. Chapter 10 analyses the advantages and the limits of Nelder-Mead optimization method to be used with the thesis topic and chapter just summarizes all the information we got from the chapters 7-10. They are immediately used in following chapters concerning the newly designed algorithms themselves.

The new proposed algorithms can be found in chapters 12 - 14. Chapter 12 describes the mentioned Flux histogram noise thresholding method and chapter 13 then the general WHIDE (Weighed and Histogram Thresholded Deconvolution) algorithm together with the explanation of the idea of statistical weighing in section 13.1. The algorithm efficiency can be analytically tested only in the simulations due to the known initial conditions, but the most important asset is of course in practical use - chapter 14 shows the use of WHIDE algorithm on the example of real data compared to the standard aperture photometry made by IRAF software.

As the WHIDE algorithm helps to get the information about dense stellar crowded fields we can say that

”The strength of the WHIDE algorithm is in getting us deeper into the deep Universe.”

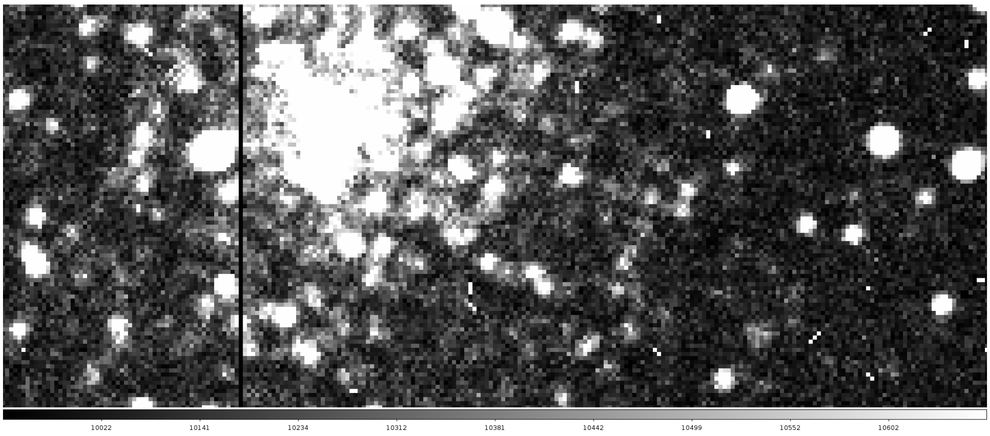

List of Figures

List of Tables

References

[1] A. ANGOT, *Užitá matematika pro elektrotechniké inženýry*, SNTL, 1971.

[2] E. ANISIMOVA, J. BEDNAR, M. BLAZEK, P. JANOUT, F. KAREL, P. PATA, J. SVIHLIK, AND S. VITEK, *Estimation and measurement of space-variant features of imaging systems and influence of this knowledge on accuracy of astronomical measurement*, in Applications of Digital Image Processing XXXVII, vol. 9217, SPIE, SPIE, Sept. 2014, pp. 92171E–1–92171E–13.

[3] E. ANISIMOVA, K. FLIEGEL, M. BLAZEK, P. JANOUT, J. BEDNAR, P. PATA, S. VITEK, AND J. SVIHLIK, *Analysis of images obtained from space-variant astronomical imaging systems*, SPIE, 2013, pp. 885607–1–885607–11.

[4] E. ANISIMOVA, P. PÁTA, M. BLAŽEK, K. FLIEGEL, K. KOTEN, AND S. VÍTEK, *Wavelet Transform for Processing of Video from MAIA System*, in Photonics, Devices, and Systems V, vol. 8306, SPIE, 2011, pp. 1–6.

[5] E. ANISIMOVA, P. PATA, AND M. BLAZEK, *Stellar object detection using the wavelet transform*, Acta Polytechnica, 51 (2011), p. 9.

[6] D. ARTHUR AND S. VASSILVITSKII, *k-means plus plus : The Advantages of Careful Seeding*, in PROCEEDINGS OF THE EIGHTEENTH ANNUAL ACM-SIAM SYMPOSIUM ON DISCRETE ALGORITHMS, 3600 UNIV CITY SCIENCE CENTER, PHILADELPHIA, PA 19104-2688 USA, 2007, ACM SIGACT; SIAM, SIAM, pp. 1027–1035. 18th ACM-SIAM Symposium on Discrete Algorithms, New Orleans, LA, JAN 07-09, 2007.

[7] R. BERRY AND J. BURNELL, *The Handbook of Astronomical Image Processing*, Willmann-Bell, Inc., 2nd ed., 2005.

[8] M. BLAŽEK, E. ANISIMOVA, AND P. PÁTA, *Application of Wavelet Transform for Image Denoising of Spatially and Time Variable Astronomical Imaging Systems*, Acta Polytechnica, 51 (2011), pp. 11–15.

[9] M. BLAŽEK AND R. HUDEC, *Faint objects on INTEGRAL/IBIS mosaics in 15 - 80 keV energy range*, in Proceedings of ”The Extreme sky: Sampling the Universe above 10 keV”, Trieste, 2009, SISSA/ISAS.

[10] M. BLAZEK AND R. HUDEC, *V1062 Tau - comparison of the X-Ray (INTEGRAL) and optical (D50) data*, in Proceedings of 8th INTEGRAL Workshop ”The Restless Gamma-ray Universe”, Trieste, 2011, SISSA/ISAS, pp. –.

[11] M. Blazek and P. Pata, *Colour transformations and K-means segmentation for automatic cloud detection*, Meteorologische Zeitschrift, 24 (2015), pp. 503–509.

[12] M. Blazek and P. Pata, *Image processing of globular clusters - Simulation for deconvolution tests (GlencoeSim)*, New Astronomy, 48 (2016), pp. 24–29.

[13] M. Born and E. Wolf, *Principles of Optics*, Cambridge University Press, Oct. 1999.

[14] C. Cabanac, *PIF method and Fourier Analysis with INTEGRAL main instruments.*, in The Extreme Sky: Sampling the Universe above 10 keV, 2009.

[15] P. Campisi and K. Egiazarian, eds., *Blind Image Deconvolution - Theory and Applications*, CRC Press, 2007.

[16] A. J. Castro-Tirado, J. Soldán, M. Bernas, P. Páta, T. Rezek, R. Hudec, T. J. Mateo Sanguino, B. de La Morena, J. A. Berná, J. Rodríguez, A. Peña, J. Gorosabel, J. M. Más-Hesse, and A. Giménez, *The Burst Observer and Optical Transient Exploring System (BOOTES)*, Astronomy and Astrophysics Supplement, 138 (1999), pp. 583–585.

[17] L. E. Davis and P. Massey, *A User's Guide to Stellar CCD Photometry with IRAF*, April 1992. p. 34 - 61.

[18] C. de Santis, A. Grazian, A. Fontana, and P. Santini, *ConvPhot: A profile-matching algorithm for precision photometry*, New Astronomy, 12 (2007), pp. 271–288.

[19] J. W. Eaton, D. Bateman, S. ren Hauberg, and R. Wehbring, *GNU Octave version 3.8.1 manual: a high-level interactive language for numerical computations*, CreateSpace Independent Publishing Platform, 2014. ISBN 1441413006.

[20] K. Fliegel, P. Páta, M. Klíma, M. Blažek, and J. Havlín, *Open source database of images DEIMOS: high dynamic range images*, in Applications of Digital Image Processing XXXIII, Bellingham (stát Washington), 2010, SPIE, pp. 77981G–1–77981G–7.

[21] P. E. Freeman, V. Kashyap, R. Rosner, and D. Q. Lamb, *A Wavelet-Based Algorithm for the Spatial Analysis of Poisson Data*, The Astrophysical Journal Supplement Series, 138 (2002), pp. 185–218.

[22] A. I. Gómez de Castro, P. Sestito, N. Sánchez, F. López-Martínez, J. Seijas, M. Gómez, P. Rodríguez, J. Quintana, M. Ubierna, and J. Muñoz, *World Space Observatory-Ultraviolet: ISSIS, the imaging instrument*, Advances in Space Research, 53 (2014), pp. 996–1002.

[23] R. GONZALEZ, R. WOODS, AND S. EDDINS, *Digital Image Processing Using MATLAB*, Gatesmark Publishing, 2009.

[24] E. W. GREISEN AND M. R. CALABRETTA, *Representations of world coordinates in FITS*, Astronomy and Astrophysics, 395 (2002), pp. 1061–1075.

[25] E. J. GROTH, *A pattern-matching algorithm for two-dimensional coordinate lists*, Astronomical Journal, 91 (1986), pp. 1244–1248.

[26] A. M. HOPKINS, C. J. MILLER, A. J. CONNOLLY, C. GENOVESE, R. C. NICHOL, AND L. WASSERMAN, *A New Source Detection Algorithm Using the False-Discovery Rate*, The Astronomical Journal, 123 (2002), pp. 1086–1094.

[27] S. B. HOWELL, *Handbook of CCD Astronomy*, Cambridge University Press, Mar. 2006.

[28] R. HUDEC, M. BLAŽEK, AND V. HUDCOVÁ, *Czech Participation in the INTEGRAL Satellite: A Review*, Acta Polytechnica, 51 (2011), pp. 38–45.

[29] P. JANOUT, P. PATA, J. BEDNAR, E. ANISIMOVA, M. BLAZEK, AND P. SKALA, *Stellar objects identification using wide-field camera*, in PHOTONICS, DEVICES, AND SYSTEMS VI, Tomanek, P and Senderakova, D and Pata, P, ed., vol. 9450 of Proceedings of SPIE, 1000 20TH ST, PO BOX 10, BELLINGHAM, WA 98227-0010 USA, 2015, Czech & Slovak Soc Photon; Act M Agcy, SPIE-INT SOC OPTICAL ENGINEERING.

[30] P. A. JANSSON, R. H. HUNT, AND E. K. PLYLER, *Resolution Enhancement of Spectra*, Journal of the Optical Society of America (1917-1983), 60 (1970), pp. 596–+.

[31] M. JELÍNEK, P. KUBÁNEK, R. HUDEC, M. NEKOLA, M. TOPINKA, AND J. ŠTROBL, *BART - Burst Alert Robotic Telescope*, in The Astrophysics of Cataclysmic Variables and Related Objects, J.-M. Hameury and J.-P. Lasota, eds., vol. 330 of Astronomical Society of the Pacific Conference Series, Aug. 2005, p. 481.

[32] H. L. JOHNSON AND W. W. MORGAN, *Fundamental stellar photometry for standards of spectral type on the revised system of the Yerkes spectral atlas*, The Astrophysical Journal, 117 (1953), pp. 313–352.

[33] I. KING, *The structure of star clusters. I. an empirical density law*, Astronomical Journal, 67 (1962), p. 471.

[34] J. KLECZEK, *Velká encyklopedie vesmíru*, Academia, 2002.

[35] P. KUBÁNEK, *RTS2 - The Remote Telescope System*, Advances in Astronomy, 2010 (2010), p. 902484.

[36] J. LAGARIAS, J. REEDS, M. WRIGHT, AND P. WRIGHT, *Convergence properties of the Nelder-Mead simplex method in low dimensions*, SIAM JOURNAL ON OPTIMIZATION, 9 (1998), pp. 112–147.

[37] L. LANDWEBER, *An Iteration Formula for Fredholm Integral Equations of the First Kind*, American Journal of Mathematics, 73 (1951), pp. 615–624.

[38] B. M. LASKER, M. G. LATTANZI, B. J. MCLEAN, B. BUCCIARELLI, R. DRIMMEL, J. GARCIA, G. GREENE, F. GUGLIELMETTI, C. HANLEY, G. HAWKINS, V. G. LAIDLER, C. LOOMIS, M. MEAKES, R. MIGNANI, R. MORBIDELLI, J. MORRISON, R. PANNUNZIO, A. ROSENBERG, M. SARASSO, R. L. SMART, A. SPAGNA, C. R. STURCH, A. VOLPICELLI, R. L. WHITE, D. WOLFE, AND A. ZACCHEI, *The Second-Generation Guide Star Catalog: Description and Properties*, The Astronomical Journal, 136 (2008), pp. 735–766.

[39] C. LIEBE, *Pattern recognition of star constellations for spacecraft applications* , IEEE Aerospace and Electronic Systems Magazine, 7 (1992), pp. 34–41.

[40] P. LINDE, *Crowded Field Photometry with HST - a Simulation*, in European Southern Observatory Conference and Workshop Proceedings, P. J. Grosbøl and R. H. Warmels, eds., vol. 38 of European Southern Observatory Conference and Workshop Proceedings, 1991, p. 225.

[41] P. LINDE AND A. JOHANNESSON, *Image Sharpening - Context-Controlled Enhancement and Deconvolution*, in European Southern Observatory Conference and Workshop Proceedings, P. J. Grosbøl and R. H. Warmels, eds., vol. 38 of European Southern Observatory Conference and Workshop Proceedings, 1991, p. 173.

[42] P. MARTINEZ AND A. KLOTZ, *A Practical Guide to CCD Astronomy*, Practical astronomy handbook, Cambridge University Press, 1998.

[43] R. D. MCCLURE, J. E. HESSER, P. B. STETSON, D. A. VANDENBERG, AND R. A. BELL, *CCD photometry of the globular cluster M68*, Astronomical Journal, 93 (1987), pp. 1144–1165.

[44] M. MELOUN AND J. MILITKY, *Kompendium statistického zpracování dat*, Academia, 2002.

[45] K. MILOŠ, F. KAREL, P. PET, V. STANISLAV, B. MARTIN, D. PETR, K. LUKÁŠ, K. T., S. M., ŘÍČNÝ V., P. L., K. O., AND B. L., *DEIMOS - an Open Source Image Database*, Radioengineering, 20 (2011), pp. 1016–1023.

[46] A. F. J. MOFFAT, *A Theoretical Investigation of Focal Stellar Images in the Photographic Emulsion and Application to Photographic Photometry*, Astronomy and Astrophysics, 3 (1969), p. 455.

[47] D. G. MONET, S. E. LEVINE, B. CANZIAN, H. D. ABLES, A. R. BIRD, C. C. DAHN, H. H. GUETTER, H. C. HARRIS, A. A. HENDEN, S. K. LEGGETT, H. F. LEVISON, C. B. LUGINBUHL, J. MARTINI, A. K. B. MONET, J. A. MUNN, J. R. PIER, A. R. RHODES, B. RIEPE, S. SELL, R. C. STONE, F. J. VRBA, R. L. WALKER, G. WESTERHOUT, R. J. BRUCATO, I. N. REID, W. SCHOENING, M. HARTLEY, M. A. READ, AND S. B. TRITTON, *The USNO-B Catalog*, The Astrophysical Journal, 125 (2003), pp. 984–993.

[48] M. NEKOLA, R. HUDEC, M. JELÍNEK, M. KOCKA, P. KUBÁNEK, F. MÜNZ, C. POLÁŠEK, V. ŠIMON, AND J. ŠTROBL, *Robotic telescopes for high energy astrophysics in Ondřejov*, Experimental Astronomy, 28 (2010), pp. 79–85.

[49] NOAO, *PHELP manual pages of IRAF system.* Documentation on http://iraf.noao.edu/, May 2000.

[50] P. PÁTA, K. FLIEGEL, M. KLÍMA, M. BLAŽEK, AND M. ŘEŘÁBEK, *Utilization of consumer level digital cameras in astronomy*, in Applications of Digital Image Processing XXXIII, Bellingham (stát Washington), 2010, SPIE, pp. 77982H–1–77982H–12.

[51] C. A. PRIMMERMAN, D. V. MURPHY, D. A. PAGE, B. G. ZOLLARS, AND H. T. BARCLAY, *Compensation of atmospheric optical distortion using a synthetic beacon*, Nature, 353 (1991), pp. 141–143.

[52] P. PŘÍHODA, *Průvodce astronomií*, Hvězdárna a planetárium hlavního města Prahy, 2000.

[53] C. RÉGULO, J. M. ALMENARA, R. ALONSO, H. DEEG, AND T. ROCA CORTÉS, *TRUFAS, a wavelet-based algorithm for the rapid detection of planetary transits*, Astronomy and Astrophysics, 467 (2007), pp. 1345–1352.

[54] W. H. RICHARDSON, *Bayesian-Based Iterative Method of Image Restoration*, Journal of the Optical Society of America (1917-1983), 62 (1972), pp. 55–+.

[55] V. N. SHALYAPIN AND L. J. GOICOECHEA, *Crowded-field image simulator for WSO-UV/ISSIS: first functional version developed by the Glendama team*, Astrophysics and Space Science, 354 (2014), pp. 187–190.

[56] V. ŠIMON, C. POLÁŠEK, R. HUDEC, AND M. BLAŽEK, *Cycles and their instability in the cataclysmic variable V795 Her*, AIP Conference Proceedings, 1248 (2010), pp. 207–208.

[57] J.-L. Starck and F. Murtagh, *Astronomical Image and Data Analysis*, Springer, 2 ed., 2006.

[58] J. L. Starck, F. Murtagh, and A. Bijaoui, *Image Processing and Data Analysis*, Cambridge University Press, 1998.

[59] P. B. Stetson, *DAOPHOT - A computer program for crowded-field stellar photometry*, Astronomical Society of the Pacific, 99 (1987), pp. 191–222.

[60] H. A. Sturges, *The Choice of a Class Interval*, Journal of the American Statistical Association, 21 (1926), pp. 65–66.

[61] D. Tody, *The IRAF Data Reduction and Analysis System*, in Instrumentation in astronomy VI, D. L. Crawford, ed., vol. 627 of Society of Photo-Optical Instrumentation Engineers (SPIE) Conference Series, Jan. 1986, p. 733.

[62] M. Řeřábek and P. Páta, *The space variant PSF for deconvolution of wide-field astronomical images*, in Society of Photo-Optical Instrumentation Engineers (SPIE) Conference Series, vol. 7015 of Society of Photo-Optical Instrumentation Engineers (SPIE) Conference Series, July 2008.

[63] F. G. Valdes, *The IRAF Mosaic Data Reduction Package*, in Astronomical Data Analysis Software and Systems VII, R. Albrecht, R. N. Hook, and H. A. Bushouse, eds., vol. 145 of Astronomical Society of the Pacific Conference Series, 1998, p. 53.

[64] P. H. van Cittert, *Zum Einfluß der Spaltbreite auf die Intensitätsverteilung in Spektrallinien. II*, Zeitschrift fűr Physik, 69 (1931), pp. 298–308.

[65] V. Vit, *Televizní technika*, BEN, 1997, ch. 2, pp. 45–52.

[66] S. Vitek and M. Blazek, *Notes on DSLR photometry*, in Notes on DSLR photometry, no. 7, Astronomical Society of India, 2012, pp. 231–238.

[67] S. Vítek, P. Koten, P. Páta, and K. Fliegel, *Double-Station Automatic Video Observation of the Meteors*, Advances in Astronomy, 2010 (2010), pp. Article ID 943145, 4 pages.

[68] M. Řeřábek, P. Páta, and P. Koten, *Processing of the Astronomical Image Data obtained from UWFC Optical Systems.*, in Image Reconstruction from Incomplete Data V, vol. 7076 of Proc. SPIE, 2008, p. 70760L.

[69] D. C. Wells, E. W. Greisen, and R. H. Harten, *FITS - a Flexible Image Transport System*, Astronomy & Astrophysics Supp. Ser., 44 (1981), p. 363W.

[70] C. Winkler, T. J.-L. Courvoisier, G. Di Cocco, N. Gehrels, A. Giménez, S. Grebenev, W. Hermsen, J. M. Mas-Hesse, F. Lebrun, N. Lund, G. G. C. Palumbo, J. Paul, J.-P. Roques, H. Schnopper, V. Schönfelder, R. Sunyaev, B. Teegarden, P. Ubertini, G. Vedrenne, and A. J. Dean, *The INTEGRAL mission*, Astronomy and Astrophysics, 411 (2003), pp. L1–L6.

Author's bibliography related to thesis

BLAZEK, M., AND PATA, P. Image processing of globular clusters - Simulation for deconvolution tests (GlencoeSim). *New Astronomy 48* (Oct. 2016), 24–29.

BLAZEK, M., AND PATA, P. Colour transformations and K-means segmentation for automatic cloud detection. *Meteorologische Zeitshrift 24*, 5 (2015), 503–509.

JANOUT, P., PATA, P., BEDNAR, J., ANISIMOVA, E., BLAZEK, M., AND SKALA, P. Stellar objects identification using wide-field camera. In *PHOTONICS, DEVICES, AND SYSTEMS VI* (1000 20TH ST, PO BOX 10, BELLINGHAM, WA 98227-0010 USA, 2015), Tomanek, P and Senderakova, D and Pata, P, Ed., vol. 9450 of *Proceedings of SPIE*, Czech & Slovak Soc Photon; Act M Agcy, SPIE-INT SOC OPTICAL ENGINEERING.

ANISIMOVA, E., BEDNAR, J., BLAZEK, M., JANOUT, P., KAREL, F., PATA, P., SVIHLIK, J., AND VITEK, S. Estimation and measurement of space-variant features of imaging systems and influence of this knowledge on accuracy of astronomical measurement. In *Applications of Digital Image Processing XXXVII* (Sept. 2014), vol. 9217, SPIE, SPIE, pp. 92171E–1–92171E–13.

ANISIMOVA, E., FLIEGEL, K., BLAZEK, M., JANOUT, P., BEDNAR, J., PATA, P., VITEK, S., AND SVIHLIK, J. Analysis of images obtained from space-variant astronomical imaging systems. SPIE (2013), pp. 885607–1–885607–11.

VITEK, S., AND BLAZEK, M. Notes on DSLR photometry. No. 7, Astronomical Society of India (2012), pp. 231–238.

BLAŽEK, M., AND HUDEC, R. V1062 Tau - comparison of the X-Ray (INTEGRAL) and optical (D50) data. In *Proceedings of 8th INTEGRAL Workshop "The Restless Gamma-ray Universe"* (Trieste, 2011), SISSA/ISAS, pp. –.

ANISIMOVA, E., PÁTA, P., BLAŽEK, M., FLIEGEL, K., KOTEN, K., AND VÍTEK, S. Wavelet Transform for Processing of Video from MAIA System. In *Photonics, Devices, and Systems V* (2011), vol. 8306, SPIE, pp. 1–6.

Klíma, M., Fliegel, K., Páta, P., Vítek, S., Blažek, M., Dostál, P., Krasula, L., et al. DEIMOS - an Open Source Image Database. *Radioengineering 20*, 4 (Dec. 2011), 1016–1023.

Blažek, M., Anisimova, E., and Páta, P. Application of Wavelet Transform for Image Denoising of Spatially and Time Variable Astronomical Imaging Systems. *Acta Polytechnica 51*, 2 (April 2011), 11–15.

Anisimova, E., Páta, P., and Blažek, M. Stellar Object Detection Using the Wavelet Transform. *Acta Polytechnica 51*, 6 (Dec. 2011), 9–12.

Páta, P., Fliegel, K., Klíma, M., Blažek, M., and Řeřábek, M. Utilization of consumer level digital cameras in astronomy. In *Applications of Digital Image Processing XXXIII* (Bellingham (stát Washington), 2010), SPIE, pp. 77982H–1–77982H–12.

Šimon, V., Polášek, C., Hudec, R., and Blažek, M. Cycles and their instability in the cataclysmic variable V795 Her. *AIP Conference Proceedings 1248* (July 2010), 207–208.

Fliegel, K., Páta, P., Klíma, M., Blažek, M., and Havlín, J. Open source database of images DEIMOS: high dynamic range images. In *Applications of Digital Image Processing XXXIII* (Bellingham (stát Washington), 2010), SPIE, pp. 77981G–1–77981G–7.